Distribution Agreement

In presenting this thesis or dissertation as a partial fulfillment of the requirements for an advanced degree from Emory University, I hereby grant to Emory University and its agents the non-exclusive license to archive, make accessible, and display my thesis or dissertation in whole or in part in all forms of media, now or hereafter known, including display on the world wide web. I understand that I may select some access restrictions as part of the online submission of this thesis or dissertation. I retain all ownership rights to the copyright of the thesis or dissertation. I also retain the right to use in future works (such as articles or books) all or part of this thesis or dissertation.

Signature:

_____ _____

Dana C. Harvey Date

High-speed & Long-time Electrostatic Measurements of Fluid & Particle Interfaces

By

Dana C. Harvey
Doctor of Philosophy

Phyics

Justin C. Burton, Ph.D.
Advisor

Saad Bhamla, Ph.D.
Committee Member

Luiz Santos, Ph.D.
Committee Member

Kurt Warncke, Ph.D.
Committee Member

Eric Weeks, Ph.D.
Committee Member

Accepted:

Kimberly Jacob Arriola, Ph. D.
Dean of the James T. Laney School of Graduate Studies

Date

High-speed & Long-time Electrostatic Measurements of Fluid & Particle Interfaces

By

Dana C. Harvey
B.S., Davidson College, NC, 2017

Advisor: Justin C. Burton, Ph.D.

An abstract of
A dissertation submitted to the Faculty of the
James T. Laney School of Graduate Studies of Emory University
in partial fulfillment of the requirements for the degree of
Doctor of Philosophy
in Phyics
2022

Abstract

High-speed & Long-time Electrostatic Measurements of Fluid & Particle Interfaces
By Dana C. Harvey

Studying the inter-facial dynamics of complex systems requires non-invasive measurement techniques. During my time at Emory, I used electrostatic concepts to probe two separate systems: the dynamics of Leidenfrost vapor layers near collapse and charge decay on acoustically levitated particles. A Leidenfrost vapor layer forms between a sufficiently hot solid and an evaporating fluid. The gas-fluid and gas-solid interfaces are treated as capacitors to capture micro-second dynamics. Using this technique, a minimum Leidenfrost temperature, $T_{-} \approx 140°\text{C}$, was found and determined to be caused by hydrodynamics alone. To expand upon experimental results, COMSOL Multiphysics simulations were conducted. Simulations uncovered a lower bound for T_{-}, which matched the experimental results. It was determined that inertia, often assumed negligible in simulations, is paramount in determining the failure of Leidenfrost vapor layers. In the second experimental system, an acoustic levitator is coupled with an inductive Faraday cup to monitor charge decay in a non-contact manner. It was found that charge remained on particles in dry environments for weeks, contradicting the current theories. Furthermore, charge decay was found to be independent of particle composition, and instead determined by environmental factors. Finally, using a 1D sedimentation model it was determined that charge must be considered when determining how far particles can travel in Earth's atmosphere.

High-speed & Long-time Electrostatic Measurements of Fluid & Particle Interfaces

By

Dana C. Harvey
B.S., Davidson College, NC, 2017

Advisor: Justin C. Burton, Ph.D.

A dissertation submitted to the Faculty of the
James T. Laney School of Graduate Studies of Emory University
in partial fulfillment of the requirements for the degree of
Doctor of Philosophy
in Phyics
2022

Acknowledgments

I would like to acknowledge the help and support of family, friends, lab mates, and mentor. Without whom I could not have made it through the last 5 and a half years.

Family: Lidia, Dawn, Dave, & Drew Harvey

Friends: Cody Herron, Alexander Palinski, Michael Moore, Joseph Gallagher, and Nick Pappayliou

Lab Mates: Xiaolei, Guga, Kavinda, Wentao, Josh ...

Mentor: Justin C. Burton

Contents

1 Introduction **1**

1.1 History of the Leidenfrost effect 1

1.2 Acoustic levitation as a tool for isolating atmospheric particles 5

2 Minimum Leidenfrost Temperature on Smooth Metallic Surfaces **12**

2.1 The failure temperature of Leidenfrost drops 13

2.2 Inverse Leidenfrost geometry as a reproducible experimental system . 15

2.3 Chapter conclusions 30

2.4 Leidenfrost thickness measurement technique 32

2.4.1 Sampling Protocol 32

2.4.2 Capacitor model of the vapor layer 32

3 Inertial Leidenfrost Collapse **35**

3.1 Leidenfrost simulations couple many physics concepts 35

3.2 COMSOL simulation Details 38

3.3 Lubrication model details 42

3.4 Chapter conclusions 52

4 The lifetime of charged dust in the atmosphere **62**

4.1 Non-contact charge measurement technique 63

4.2 Schlieren imaging 68

4.3 Behavior determines the discharge behavior 70
4.4 1-D sedimentation model 78

5 Conclusions **85**

Bibliography **89**

List of Figures

1.1 Burton Drop Geometry 2
1.2 Star Shaped Oscillations 3
1.3 Acoustic field Cartoon 6
1.4 Saharan Dust Transport 9

2.1 Drop Failure Temp as a Function of Size 14
2.2 Inverse Leidenfrost Experimental Setup 16
2.3 Capacitor Equivalent Circuit 17
2.4 Total Circuit Design 18
2.5 Leidenfrost Collapse Cartoon 20
2.6 Comsol Interface Profiles 21
2.7 Capacitor Fit 22
2.8 Hysteresis in Inverse Leidenfrost Experiment 23
2.9 Complex impedance 24
2.10 High-Speed Capacitance 25
2.11 Failure Points 27
2.12 Time Series 28
2.13 Effect of Immersion depth 29
2.14 Effect of NaCl Concentration 31

3.1 Leidenfrost Wavefront 36

3.2 Experiment Basis for Simulation 36
3.3 Simulation Size 39
3.4 Copper Simulation Time Series 43
3.5 Aluminum Simulation Time Series 44
3.6 Titanium Simulation Time Series 45
3.7 Lubrication Velocity Profile 46
3.8 Lubricating Flow 48
3.9 COMSOL & Lubrication Interface Comparison 51
3.10 Surface area of the vapor layer 53
3.11 T_- vs A_eff of Simulations and Experiments 55
3.12 COMSOL Velocity Field 56
3.13 Radial Velocity Profile 57
3.14 Simulation Wave Mechanism 59
3.15 Increasing γ or Mw increases T_- 60
3.16 Effect of Mw and surface tension on T_- 60

4.1 TinyLev Acoustic Levitator 63
4.2 Charge Distributions 64
4.3 Ionizer Requirements 65
4.4 Voltage Measurement Schleiren Image 66
4.5 Types of Particles 67
4.6 Schlieren Imaging Technique 69
4.7 Normalized Charge Decay 71
4.8 Half Life vs Humidity 75
4.9 Effect of UV on Charge Decay 76
4.10 Vaccum Chamber shows longer decays 78
4.11 Air Density for 1D sedimentation Model 81
4.12 1D Settling time model 82

Chapter 1

Introduction

The work presented in this dissertation consists of two distinct systems: The Leidenfrost vapor layer and charge decay of acoustically levitated particles. Here brief overviews are given for both systems as well as descriptions for some of the techniques used to put this work in context of the general literature.

1.1 History of the Leidenfrost effect

In his seminal 1756 treatise, J. G. Leidenfrost noted that a water droplet placed on a heated, polished metal spoon does not wet the surface [68]. Instead, the water droplet levitates above the hot surface, cushioned by a vapor film generated by evaporation. For water it is generally understood that a vapor layer exists above 250-300°C with a thickness of order 100 μm. The Leidenfrost effect has been well studied due to its importance in industrial, geophysical, and laboratory contexts [90]. In industry, precise knowledge of the temperature of formation helps inform the limits of water cooling in factories and nuclear reactors. Water cooling relies on liquid-solid contact to dissipate heat from the interface. If the hot object rises above the Leidenfrost temperature, the vapor barrier that forms will have a significantly lower thermal conductivity diminishing the fluids ability to cool. In the lab, experiments often

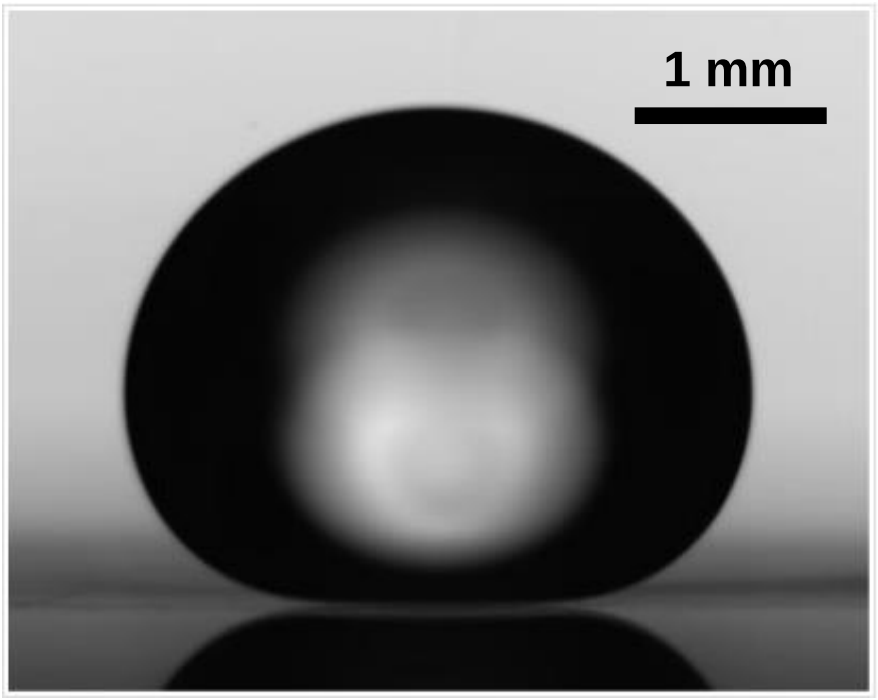

Figure 1.1: A stable water droplet on a hot surface, as published by Burton *et al.* [16], will have a vapor layer thickness of order 100 μm when the temperature is well above 250°C.

focus on the physics of Leidenfrost droplets, where an evaporating fluid is placed on a hot solid. Examples include studying vapor layer geometry beneath droplets [17, 6, 10, 98, 30, 70] (see **Fig. 1.1**), spontaneous motion and oscillations of drops [13, 26, 65, 69, 36, 73, 74] (see **Fig. 1.2**), drop impact on heated surfaces [105, 20, 92, 118], and "nano-painting" through particle deposition [7, 33].

In nature, the Leidenfrost effect–or more precisely, the collapse of a Leidenfrost vapor layer between ascending magma and an aquifer–underpins one of the most energetic and common forms of volcanism: phreatomagmatic eruptions [72, 28]. The Leidenfrost effect need not involve water or even a liquid; blocks of sublimating CO_2 ice may "surf" down Martian dunes on lubricating layers of CO_2 gas, carving channels and pits on the red planet's surface [79]. This very manifestation of the Leidenfrost effect may help power the first Martian colonies [113].

In all of these examples, precise knowledge of the transition temperature at which

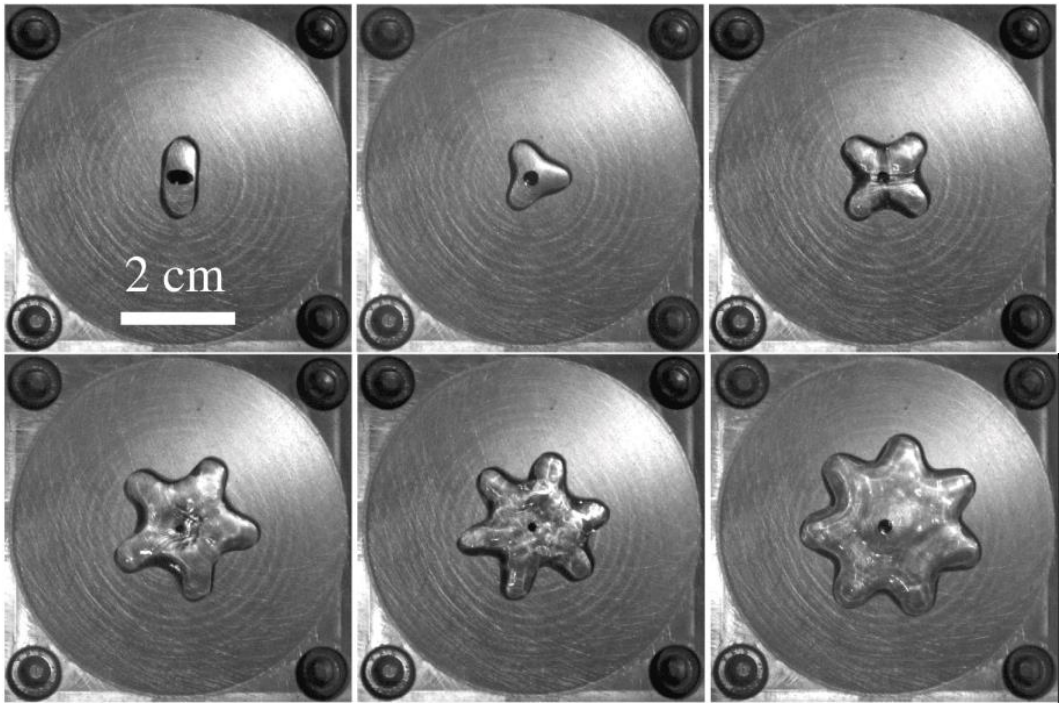

Figure 1.2: Spontaneous star shaped oscillations of water drops on a curved surface of various volumes taken from Fig. 8 of Ma *et al.* [73].

the vapor layer forms (or fails) is crucial. However, reported values of this temperature vary widely in the literature, and are known to depend on surface roughness [58, 59, 63, 57, 50], hydrophobicity [71, 108, 109, 57], thermal properties of the solid [35, 108, 109, 116, 44, 96], bulk liquid temperature [51, 35, 96, 116, 117, 57], solid geometry [14, 45, 51, 35, 108, 109, 96, 116], and liquid impurities [45, 1, 44, 57]. For smooth, homogeneous surfaces, a comprehensive theoretical study by Zhao *et al.* showed that the temperature at which the vapor layer forms spontaneously from liquid-solid contact depends only on the hydrophobicity of the surface [123]. For water drops on metallic surfaces, this corresponds to temperatures exceeding 200°C. Yet, once formed, Leidenfrost drops can exist on metal surfaces with temperatures below boiling (100°C) [8].

In the second chapter, we show how this large metastable region between formation and failure arises from the hydrodynamic stability of the gas flow in the vapor

layer. Our experiments employ a new electrical technique that can directly measure the average thickness of the vapor layer around a heated solid with microsecond resolution. For smooth metallic surfaces, we find a formation Leidenfrost temperature, T_+, consistent with recent predictions of a nanoscale wetting theory [123]. Once a stable vapor layer is formed over a given solid surface, its thickness is solely a function of the surface temperature, T_s. Remarkably, we find a minimum Leidenfrost temperature, T_-, which is nearly independent of liquid impurities and solid properties. At this temperature, the vapor layer spontaneously fails through liquid-solid contact and rapid boiling. Our results show that hydrodynamics alone cause the vapor layer to fail, however the experiments cannot give us further information. To investigate the root cause of the instability, I developed COMSOL Mulitphysics simulations of Leidenfrost vapor layers [25].

Previous simulations investigating the geometry of stable Leidenfrost drops have matched experiments very well [6, 23, 10, 17]. However, approximations made for stable geometries become invalid as the vapor layer thins near failure. In particular, separating the fluid dynamics of a droplet into a lubrication approximation on the bottom, encompassing the vapor layer (10-100 μm thick) and the boundary fluid, and a Navier-Stokes fluid on the top with a boundary matching point [6, 23]. This approximation requires a smooth velocity gradient in the vapor layer, which cannot be true during the wave instabilities we see in experiments. Another common approximation is to have a uniform temperature in the fluid, which ignores convection and more importantly eliminates the computational costs of evaporation (energy consumption), heat transfer, phase mixtures, and phase boundary conditions [23]. If we want to investigate the instability that causes vapor layer failure we do not want to neglect any fluid flows that may lead to surface waves, so we cannot assume a uniform temperature or a smooth gradient in the velocity field.

In the third chapter, I confirmed the results of our experiments with simulations

that combine two-phase flow, heat transfer, and evaporation. I found the same T_{-} as in experiments, which was independent of thermal properties of the solid. Furthermore, by changing certain parameters in the simulation, we are able to determine that inertia, often neglected in simulations, plays a key role for vapor layer failure.

1.2 Acoustic levitation as a tool for isolating atmospheric particles

In the second system, we used an acoustic levitator to electrically isolate particles to track their charge in time. We chose a non-resonant levitator, which uses arrays of transducers that allow for manipulation of particles along the primary axis [77]. Recently, investigators have successfully used acoustic levitation to levitate small animals [114, 3], iridium (the second most dense naturally occurring metal) [115], and fluids [3]. The robustness of the technique brings new perspective to isolated systems in laboratory settings. For example, manipulation of fluids in acoustic fields could help us understand ice nucleation of isolated droplets [81, 3], or be utilized for precise drug delivery inside the human body [76]. By isolating particles with compositions similar to those found in Earth's atmosphere we observed, *in situ*, how particles lose charge only through their surrounding environment.

An acoustic field is generated by sound waves, emitted by a transducer or many transducers, interacting constructively and destructively to produce a pressure field, see **Fig. 1.3**. A particle placed in the acoustic field will alter the interactions between waves and in fact, gives rise to the second order acoustic radiation force, F_{rad}, responsible for levitation. In 1962, L.P. Gor'kov first defined the acoustic potential field, U_{rad}, created by placing a small particle (size $\ll \lambda$) in an acoustic field and considering 2^{nd} order perturbations. Typical wavelengths of sound in air are $8.6 < \lambda < 12.3$ mm, corresponding to frequencies between 40 and 28 kHz respectively. U_{rad} has since

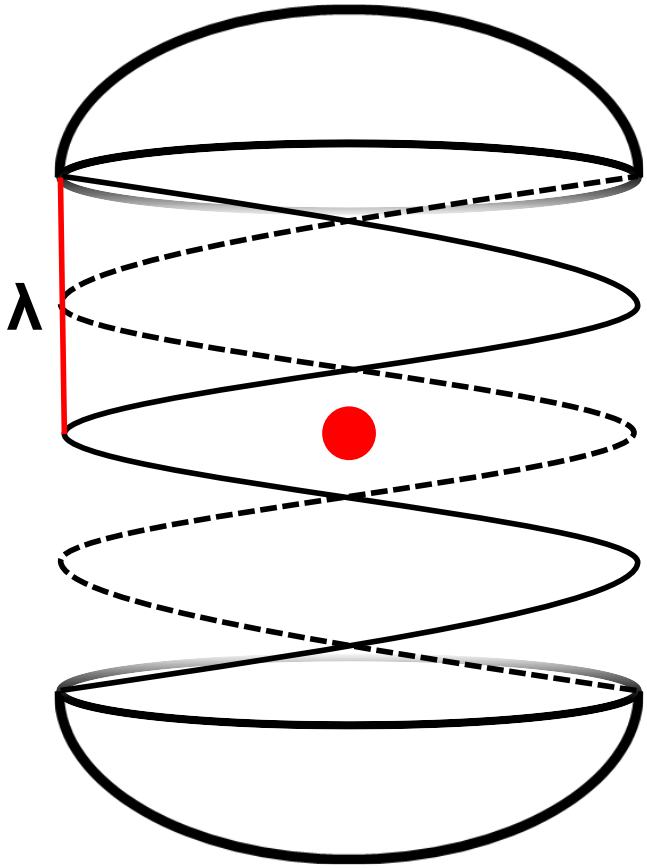

Figure 1.3: A cartoon diagram of how transducers emit sound waves. Areas of constructive interference correlate to high pressure swings. A particle of the right size and density will levitate according to F_{rad} at the peaks of the pressure swing.

been known as the Gor'kov potential used to determine F_{rad}, and defined as follows [37, 15]:

$$U_{rad} = \pi a^3 \kappa_0 p_1^2 \left[\frac{f_1}{3} \cos^3(kz) - \frac{f_2}{2} \sin^2(kz) \right], \tag{1.1}$$

$$F_{rad} = \nabla U_{rad}, \tag{1.2}$$

where a is the radius of the particle, p_1 is the first order harmonic perturbation pressure, $f_1 = 1 - \kappa_p/\kappa_0$ and $f_2 = 2(\rho_p - \rho_0)/(2\rho_p + \rho_0)$ are the first and second order perturbation frequencies, κ_p and κ_0 are the compressibilities of the particle and fluid respectively, $k = 2\pi/\lambda$ is the wave vector, λ is the acoustic wavelength, and ρ_p and ρ_0 are the densities of the particle and fluid respectively. In our system the fluid is air and $f = 40$kHz, therefore we can assume $\kappa_0 \gg \kappa_p$, so that $f_1 \approx 1$, and $\rho_p \gg \rho_0$, so that $f_2 \approx 1$. Solving for F_{rad} we get:

$$F_{rad} = \frac{5}{6} \pi k a^3 \frac{p_1^2}{\rho_0 c_0^2} \sin(2kz) \hat{z}. \tag{1.3}$$

Here the speed of sound is defined as $c_0 = \sqrt{1/\rho_0 \kappa_0}$. It is important to note that F_{rad} is in the z direction (along a levitator axis) and that it is strongest at $\frac{1}{2}\lambda$ intervals corresponding to the peaks shown in **Fig. 1.3**. The parameters of F_{rad} can be optimized for the given fluid, particle type, and λ of a system, making acoustic levitation a robust technique. We were particularly interested in using this tool to isolate small insulating materials that cannot be levitated using techniques like magnetic levitation.

Using acoustic levitation to suspend particles, we can begin to understand charge accumulation and dissipation of insulating materials. Previous work has used acoustic levitation to determine how charge transfers between 2 levitated particles that are periodically collided, separated, and then measured [67]. By altering the composition

of the particles Lee *et al.* presented work to further our understanding of charge transfer even between particles of the same material [67]. However, there are even more fundamental questions left to answer for charged particles. For instance: How does charge decay off of an isolated particle? and How is charge accumulated by isolated particles in the atmosphere? Using acoustic levitation to isolate particles on long timescales we answer the first of these questions to help determine how particles like dust in Earth's atmosphere retain charge.

Atmospheric dust is an important component of local and global climate systems. Mineral dust is the most abundant aerosol type by mass and is emitted into the atmosphere at a rate of up to 5000 Tg/yr [60, 62]. While the flux of material into the atmosphere is large, the steady state value of material is about 17 Tg. Thus, most of the material injected into the atmosphere settles out. Small, localized events, like volcanic eruptions or wild fires also contribute to Earth's dust budget (volcanoes, for instance, inject ≈ 13 Tg of ash into the atmosphere every year [53]). At regional scales dust emission from wildfires, volcanoes, and dust storms may rapidly and dramatically alter local atmospheric dust budgets. These acute increases in solid mass loading represent hazards to populations, natural environments, and infrastructure [119, 54]. On a planetary-wide scale, atmospheric dust interacts with short- and long-wave radiation, tuning the Earth's energy balance [102]. In turn, this modulation has profound impacts on sea and land surface temperatures, atmospheric circulation, and weather [46, 22]. Solid particles may also serve as cloud condensation and ice nuclei, influencing the formation of clouds and impacting precipitation rates [94]. Airborne particles have the ability to carry nutrients, toxins, and bacteria across long distances. Indeed, Saharan desert dust has been recognized as an important source of phosphorous for the Amazon rain forest [120], see **Fig. 1.4**. Similarly, lofted dust can modify atmospheric chemistry by providing reactive substrates for various chemical species [107]. Beyond Earth, atmospheric dust likely influences surface processes on

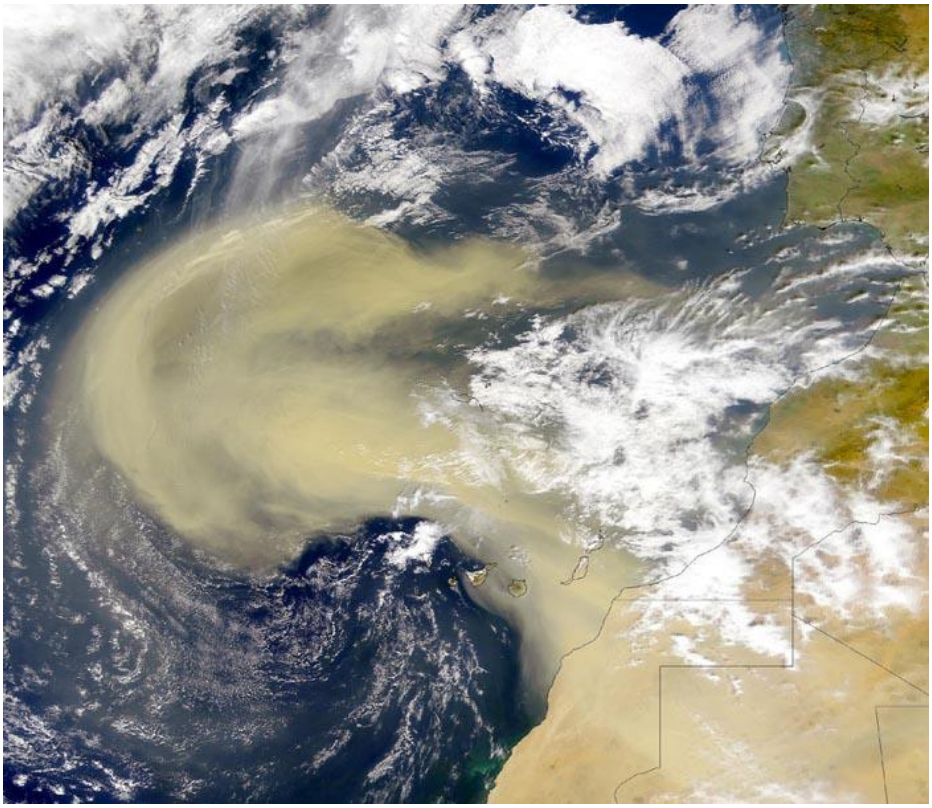

Figure 1.4: Saharan dust transports nutrients to Earth's oceans. Electrostatic forces may help explain the longer than expected distances this type of dust can travel. Photo courtesy of NOAA https://www.nesdis.noaa.gov/content/dirt-atmospheric-dust

Venus, Mars, Io, Titan, and Gliese J1214b [103, 82, 93, 80].

Since the 1970s, evidence indicates that climate models fail to accurately represent the quantity of coarse-mode particles (with diameters $D > 5$ μm) in the atmosphere [112, 2] by a factor of 4 [2]. Although dust transport models predict that coarse dust settles rapidly, observations consistently find large particles at distances well beyond the maximum ranges estimated numerically. For instance, Denjean *et al.* showed that the effective diameter of coarse-mode Saharan dust over the Mediterranean remained unchanged for up to a week after being lofted into suspension [29]. Likewise, modelling shows that particles in the range of 20–30 μm should settle out of the Saharan Air Layer in approximately 1.5-3 days. Yet, grains with these diameters have been detected over the Caribbean after 4,000 km and 5 days of transport [112].

Maring *et al.* [75] found that the distribution of dust over the Canary islands requires that particles experience upward velocity of ∼0.33 cm/s imparted by some unknown process.

Recently, electrostatic forces have been invoked to account for extended residence times of dust in the atmosphere [104]. Particles may charge as they are injected into the atmosphere through aeolian action, splashing, chemical processes, and comminution [61]. Charging mechanisms include fracto- and triboelectric charging [48, 83, 111], radioactive decay [4], and gas ionization [86]. Surprisingly, a number of investigations have demonstrated that airborne particles may remain charged even at great distances from where they emanate. For example, high space charge densities were found in an ash cloud 1,200 km from its source at the Eyjafjallajökull volcano [40], and Saharan dust over Scotland can carry an edge charge density several times larger than that of typical stratiform clouds [41].

Accurately assessing the degree to which electrostatic forces influence the transport of large particles requires better constraints on 1) the magnitude of the electric fields within atmospheric dust layers, 2) the mechanisms by which particles charge before and after being lofted, and 3) the ability of electrified grains to retain charge once airborne. Improvements to our understanding of the meso- to macroscale electrostatic characteristics within dusty environments may come from a combination of airborne and ground-based measurements, complemented by numerical modeling [40, 84, 2, 122]. However, elucidating charge evolution on particles fundamentally requires long-term measurements at the grain scale. Such measurements are difficult to do *in-situ* and, until recently, laboratory experiments have been unable to isolate charged grains from other surfaces to mimic airborne transport.

In the fourth chapter, we investigated the longevity of charge on isolated particles of various compositions suspended in air. We implemented a non-contact charge measurement technique that could monitor charge decay of a single acoustically-

levitated particle for days to weeks. Unlike previous investigations which allowed charge to leak away across contact points, the presented experiments characterize charge loss occurring only at the particle-gas interface. Our results suggest that lofted particles can retain charge for weeks, with the decay rate depending only on environmental factors like relative humidity, charge polarity, and irradiation. Relative humidity (RH) decreases the half-life ($t_{1/2}$) of charge decay by roughly a factor of 10 at saturation, while particle composition, size (in the range of 0.5 to 2 mm), and polarity seem to have little effect. Asymmetries in the effect of UV radiation requires further study, but can provide insight into the relative influence of radiation on particles in Earth's atmosphere. We present a simple ion recruitment model that can accurately predict decay times and curves below 60-70% RH. Together, our experiments and models show that electrostatic forces significantly influence the residence times of particles with diameters between 1 and 100 μm.

Chapter 2

Minimum Leidenfrost Temperature on Smooth Metallic Surfaces

In this chapter, I will explain the experiments performed to investigate the failure of Leidenfrost vapor layers. The text here has been adapted from the published paper of the same title [42]. We tracked the thickness of the vapor layer in time using a novel technique which treats the vapor layer as the dielectric of a capacitor between a hot solid and the evaporating liquid. This simple method allowed us to investigate three major questions: At what temperature does the vapor layer fail upon cooling? At what temperature does the vapor layer form upon heating? What properties can affect these temperatures?

We started with the more studied case of Leidenfrost water drops on a hot solid. In the drop experiments, the aluminum substrate was heated and drops were placed onto the substrate until a vapor layer formed. The heater was then turned off and the drop was left to evaporate until liquid solid contact. We then used a more controllable "inverse Leidenfrost" system to systematically explore the effect of solid thermal properties and NaCl concentration on the Leidenfrost temperature. In these experiments the hot object was immersed in water and a vapor layer formed around

the solid. The fixed geometry of the hot object with an evaporating bath allowed for more repeatable results than drop systems. We found a hydrodynamically determined minimum Leidenfrost temperature, $T_- \approx 140°C$, that is over 100°C less that the temperature required to form a vapor layer, T_+.

2.1 The failure temperature of Leidenfrost drops

The most studied Leidenfrost system is that of Leidenfrost drops where water placed on a sufficiently heated surface will levitate on its own vapor. In this system, we considered the importance of two temperatures, the temperature required to form a vapor layer, T_+, and the temperature at which an established vapor layer will fail, T_-. The hot object is an aluminum substrate with a polished concave surface. The substrate was heated using an embedded ceramic heater while a k-type thermocouple measured the temperature. Water was periodically dropped on the surface using a pipette until a vapor layer formed instantaneously at $T_+ = 190 \pm 20°C$. The heater was then turned off and the aluminum cooled. As the surface cools, the drop evaporates, but remains levitated until eventually, liquid-solid contact occurs at T_-. **Figure 2.1a** illustrates how a small water droplet can levitate over a heated concave aluminum surface with temperature $T_s < T_+$.

The failure temperature, T_- varies with drop size (**Fig. 2.1b**). Surprisingly, droplets smaller than ≈ 100 μm can even levitate below the boiling point by way of a diffusive Stefan flow [121]. Conversely, droplets with radii larger than the capillary length of water, $l_c \sim 2.5$ mm, fail at higher temperatures that are roughly independent of drop size. Large variations in T_- exist in this regime, possibly due to vapor layer oscillations sustained by evaporation [73, 21]. However, failure always occur near or below $T_+ = 190 \pm 20°C$.

What determines T_-? Drops on flat surfaces with radii larger than ≈ 10 mm are

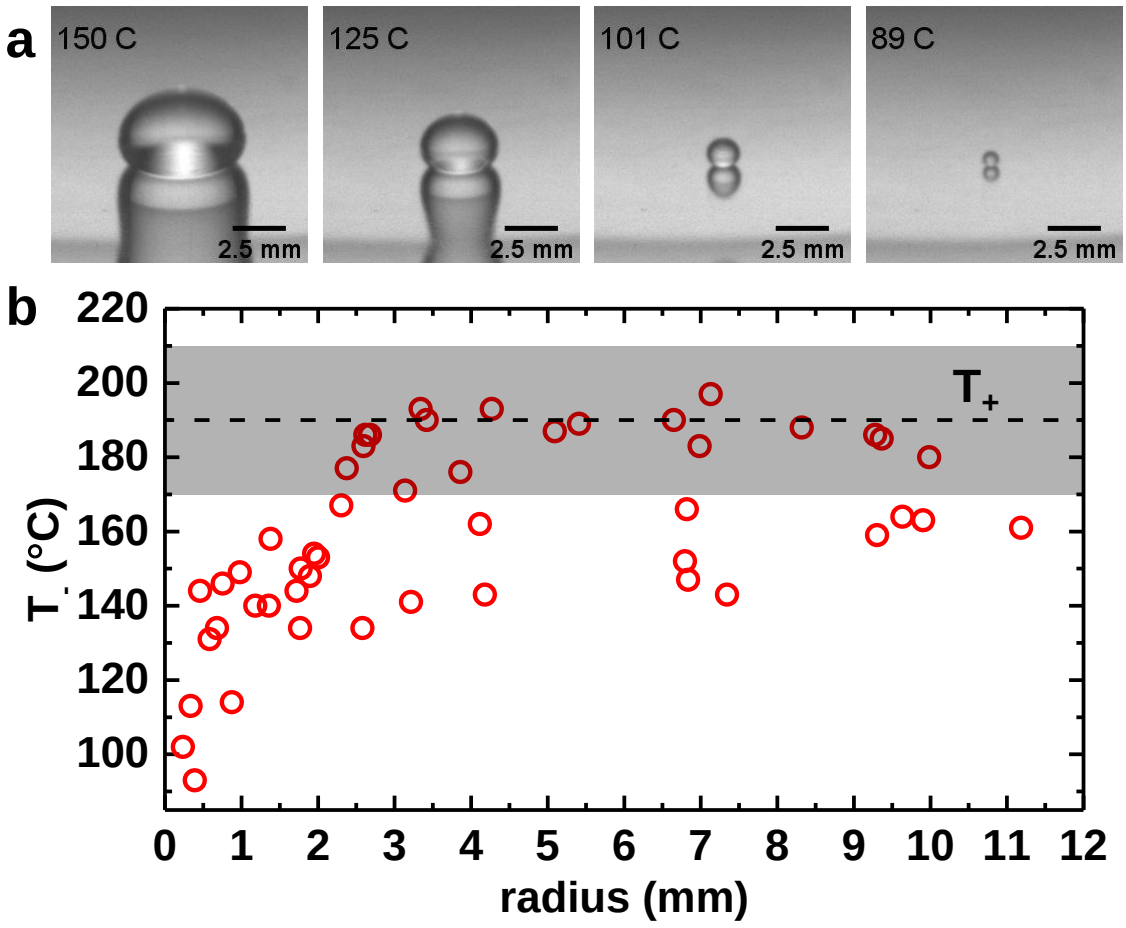

Figure 2.1: (a) Sequence of images showing a single pure water Leidenfrost drop that remains levitated over a heated aluminum surface below the boiling point. (b) Failure temperature, T_-, as a function of drop radius. Each data point represents a different water drop. The upper Leidenfrost temperature, $T_+ = 190 \pm 20°\text{C}$, is indicated by the dashed line and shaded region.

known to succumb to the Rayleigh-Taylor instability [10, 98], yet **Fig. 2.1b** shows that all drops fail below a minimum temperature, regardless of size. To better investigate the thickness and dynamics of vapor layers near collapse we wanted to control as many parameters as possible. While drops are a well studied system, they include many uncontrollable degrees of freedom. Drops spontaneously oscillate [74, 73, 90], have a tendency to move around surfaces [12], and constantly shrink as water evaporates. To control the surface area of the vapor layer and eliminate movement we chose to use an "inverse Leidenfrost" geometry. We used a heated metallic cylinder (diameter = 7.9 mm) with a rounded tip immersed into a liquid bath heated to a temperature T_l (**Fig. 2.2**) so that a vapor layer forms around it. A ceramic heater and thermocouple were embedded in the cylinder, and the bath was heated externally. With this geometry, both T_s and the water liquid level, H **(Fig. 2.3b)**, could be controlled independently.

2.2 Inverse Leidenfrost geometry as a reproducible experimental system

Our inverse Leidenfrost system was designed for high-speed measurements of the dynamics of the vapor layer, shown in **Fig. 2.2**. The upper metal electrodes were constructed from titanium alloy, brass, and copper, where the brass and copper parts were electroplated with nickel to resist corrosion. The electrode consisted of cylinders of length 8.90 cm and radii 7.94 mm, where one end is a hemispherical tip of radius 7.94 mm, and the other has a lip of radius 1.11 cm. The lip rested on ceramic, insulating washers attached to a vertical, linear motion system which allowed us to raise and lower the heated electrode. The lower electrode, same geometry, but 6.35 cm long, was fully immersed in the bath and machined from titanium alloy to be resistant to salt water. The upper electrodes were heated using a cylindrical ceramic heater cemented in the center of the rod. A K-type thermocouple at the end of the

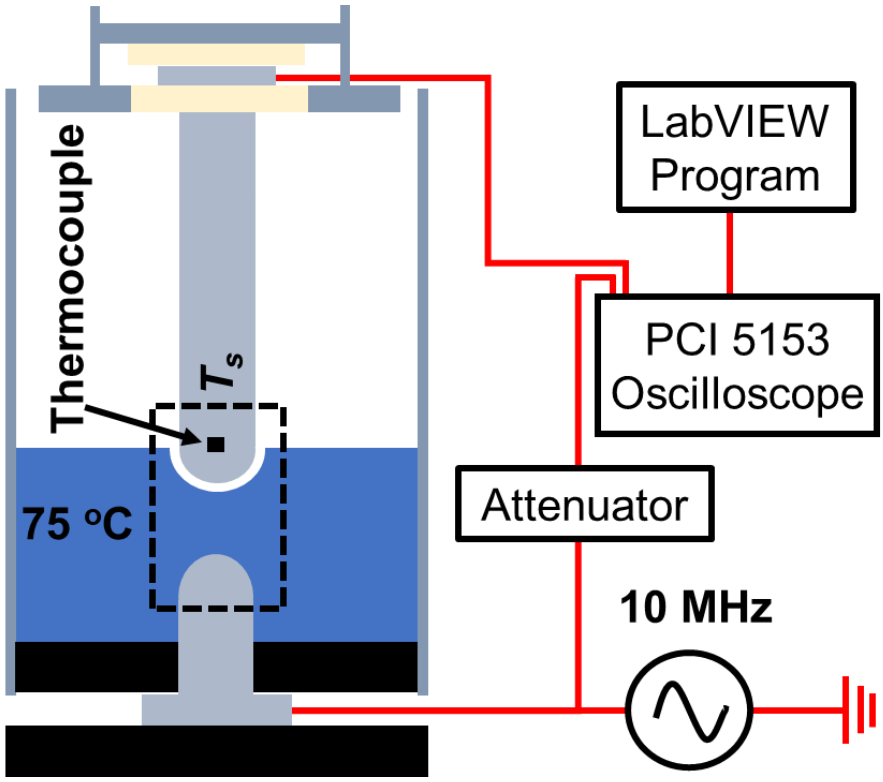

Figure 2.2: Experimental setup for high-speed measurements of the vapor layer dynamics. The dashed box indicates the complex impedance which varies in time.

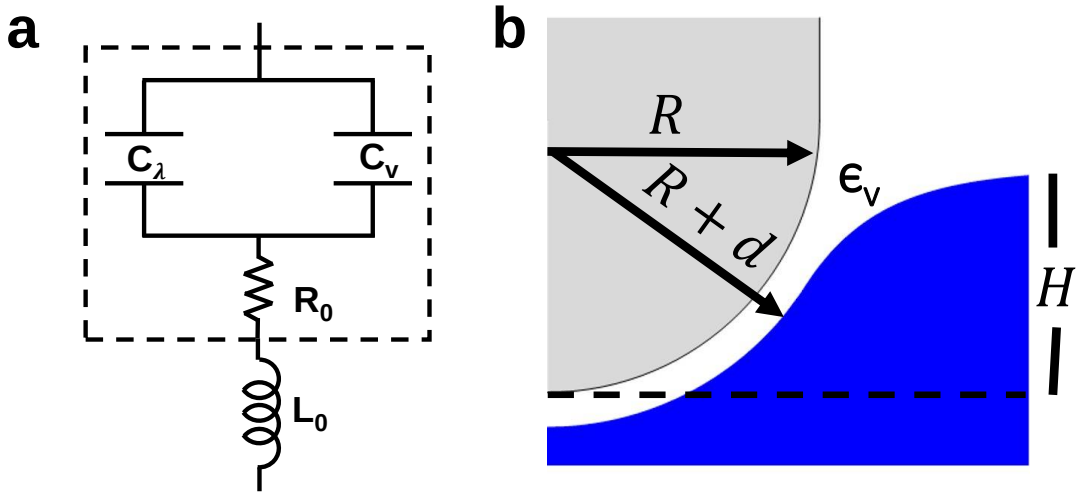

Figure 2.3: (a) Equivalent circuit for the complex impedance of the vapor layer, as described in the text. Both C_v and C_λ are time dependent. (b) Simplified geometry for modeling the capacitance of the vapor layer.

ceramic heater measured T_s near the tip **Fig. 2.2**.

The liquid temperature, T_l, was maintained using an exterior water bath, heated by a hot plate and silicon heaters glued to the experimental chamber. $T_l \approx 75°C$ was measured with k-type thermocouple placed at the bottom of the experimental chamber. The external bath was connected by a small tube to the experimental chamber so that water could be siphoned to keep H constant. The upper electrode started at room temperature (hysteresis experiments) or was heated above 600°C before being lowered to a set position in the water bath.

To study the dynamics of the vapor layer at short time scales, we monitored the electrical impedance between the heated solid and a geometrically-similar lower electrode in the bath. The lower electrode was immersed completely in the liquid, whereas the heated electrode was immersed only to a depth of H (see **Fig. 2.3b**). A 10 MHz signal supplied by an Agilent 33220A function generator was split into two cables of identical length **Fig. 2.4**. One split was driven into the lower electrode and then measured at the heated electrode with a PCI-5153 computer-based oscilloscope. This path included Z_{unknown}, which represents the complex impedance of the Leidenfrost

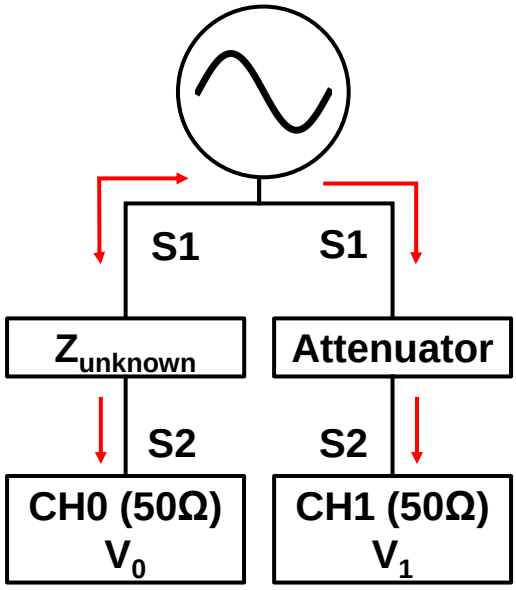

Figure 2.4: Measurement system used to determine Z_{unknown} of the Leidenfrost system. The carrier wave (10 MHz) traveled along RG58C/U cables of lengths $S1$ and $S2$. The telegraphers equations are solved along each length of cable. Arrows indicate allowed directions of current along each cable. By simultaneously measuring V_0 and V_1, we could determine Z_{unknown}.

system (**Fig. 2.3a**), including any parasitic capacitance or inductance. The other split passed through a 6 dB pi-pad attenuator, which minimized noise in the final measurement by forcing the voltage range of each channel to be the same [89]. The amplitude and phase of the signals were extracted by custom software-based lock-in detection (**Fig. 2.4**). For more information on the signal sampling see section 2.4.1. This circuit is similar to recent experiments investigating drop coalescence by Paulsen *et al.* [89]. We added a variable concentration of NaCl salt to the bath in order to increase the conductivity of the liquid. $Z_{unknown}$ was extracted using the telegrapher's equations as described in more detail in section 2.4.2.

The region between the two electrodes, shown in the dashed box in **Fig. 2.2a**, can be modeled as an RLC circuit (**Fig. 2.3a**). The inductance, L_0, represents parasitic inductance in the experimental apparatus, and R_0 is the combined resistance of the liquid and metal-liquid boundaries. We treat the vapor layer as a capacitor, where

one plate is the heated metal electrode and the other is the liquid surface (see **Fig. 2.3b**). The interface between the upper, heated electrode and the liquid is modeled as a parallel combination of two capacitors. C_v is the capacitance of the vapor layer, and C_λ is the capacitance of the double layer that forms upon liquid-solid contact (**Fig. 2.5**). The transition from a vapor layer capacitor to a Debye layer capacitor can be thought of as liquid bridges contacting the hot surface, **Fig. 2.5a**. We assume that the transition is so fast that d remains constant as the wetting front grows. When the vapor layer is present, $C_\lambda = 0$ and the average vapor layer thickness, d, can be computed using a simple geometric model. First, the vapor layer is modeled as a hemispherical capacitor with inner and outer radii equal to R and $R+d$, respectively:

$$C_1 = 2\pi\epsilon_v \frac{R(R+d)}{d} \times c\frac{H}{R}. \tag{2.1}$$

The first term corresponds to a hemispherical capacitor. However, as shown in **Fig. 2.3b**, the vapor layer does not encompass the entire volume between the two hemispheres for a given value of the immersion depth H. To lowest order, we modified the volume of the vapor layer by a factor of cH/R, where c is a numerical constant that takes into account the curved water surface away from the electrode.

In our experiments, $R = 7.9$ mm and $\epsilon_v = 1.0057\epsilon_0$ is the dielectric constant of water vapor at 100°C. Since $d/R < 1.5\%$, we only consider the leading order term so that

$$C_1 = 2\pi cH\epsilon_v \frac{R}{d}. \tag{2.2}$$

As the water level is lowered ($H \to 0$), the capacitance approaches that of a sphere above a flat plane. To leading order, this is given by

$$C_2 = 2\pi\epsilon_v R \ln\left(\frac{R}{d}\right) + C_0. \tag{2.3}$$

C_0 is a constant that contains the residual capacitance of the rest of the cylindrical

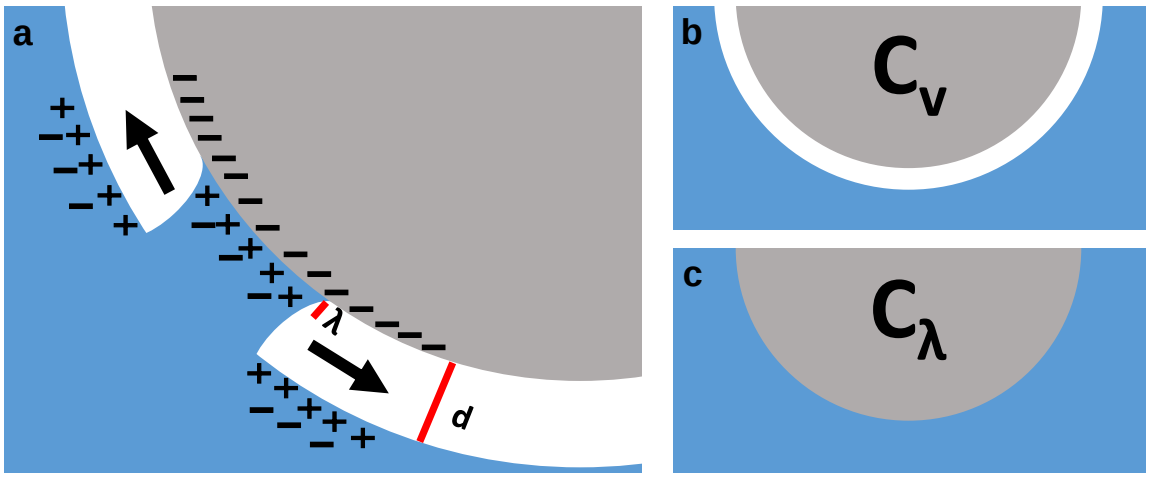

Figure 2.5: (a) During the collapse of a vapor layer with thickness d, the capacitance rapidly changes due to the formation of a double layer of thickness $\lambda \ll d$. (b) Prior to collapse, the capacitance is solely determined by the capacitance of the vapor layer, C_v. (c) After collapse, it is the double layer capacitance, C_λ, which dominates the parallel combination.

electrode. Combing these terms gives us a relationship between $C_v = C_1 + C_2$ and d:

$$\frac{C_v - C_0}{2\pi R \epsilon_v} = \frac{cH}{d} + \ln\left(\frac{R}{d}\right). \tag{2.4}$$

To verify Eq. 2.4, we generated the equivalent electrostatic geometry in COMSOL and measured the resulting capacitance. The water surface profile was computed by a surface of revolution composed of two curves: 1) an arc of a circle with radius $R+d$ and 2) a hydrostatic solution of the water's surface profile taking surface tension and gravity into account [16]. The two curves were matched at a point with continuous first derivatives, providing a unique solution given the boundary conditions (**Fig. 2.6**). An arc of radius $R+d$ centered on the tip is matched to a surface profile, $f(r)$, given by balancing surface tension and gravitational forces [16]:

$$f'' + \frac{f'}{r} = \frac{g\rho_l}{\gamma} f - P_0. \tag{2.5}$$

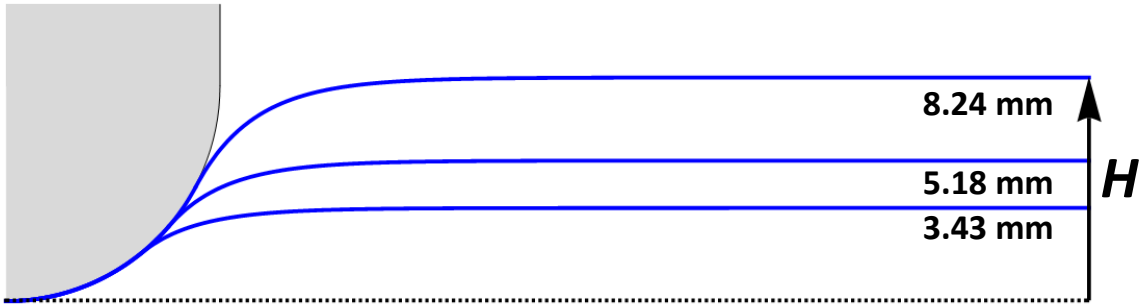

Figure 2.6: Piecewise water surface profiles for a 30 μm vapor layer at various values of H. When computing capacitance in the COMSOL model, these profiles are rotated about the z axis.

Here, ρ_l is the liquid density, g the acceleration due to gravity, γ is the surface tension, and P_0 is a constant pressure. The prime denotes differentiation with respect to r. We have also assumed that the interface profile is shallow, i.e. $f'(r) << 0$, to simplify the full expression for the curvature and produce a linear equation.

The outer boundary conditions were $f(R_{max}) = H$ and $f'(R_{max}) = 0$. The curved outer surface given by Eq. 2.5 was patched at a point r_0 to the inner circular arc with the requirements of continuity in f and f', which then determined the appropriate values of r_0 and P_0. The equations are solved analytically using Mathematica, resulting in a complex expression for f containing Bessel functions. By simulating many curves with 1.3 mm $< H <$ 8.3 mm and 10 μm $< d <$ 100 μm, we found excellent agreement with Eq. 2.4, as shown in **Fig. 2.7**. The data collapses well for $c = 0.58$ and $C_0 = 1.85$ pF. To find d from measurements of C_v, Eq. 2.4 was analytically solved in terms of product logarithms.

Upon heating and then cooling the immersed upper electrode, we observed a large, metastable region characterized by hysteresis in d versus T_s, in agreement with **Fig. 2.1b**. Figure **2.8** shows the average vapor layer thickness between pure water at $T_l =$ 75-95°C and a nickel-coated copper electrode. For this particular experiment, NaCl was not added to avoid salt deposition on the electrode surface. Bubble nucleation and detachment resulted in large variations in our measurements of d during heating.

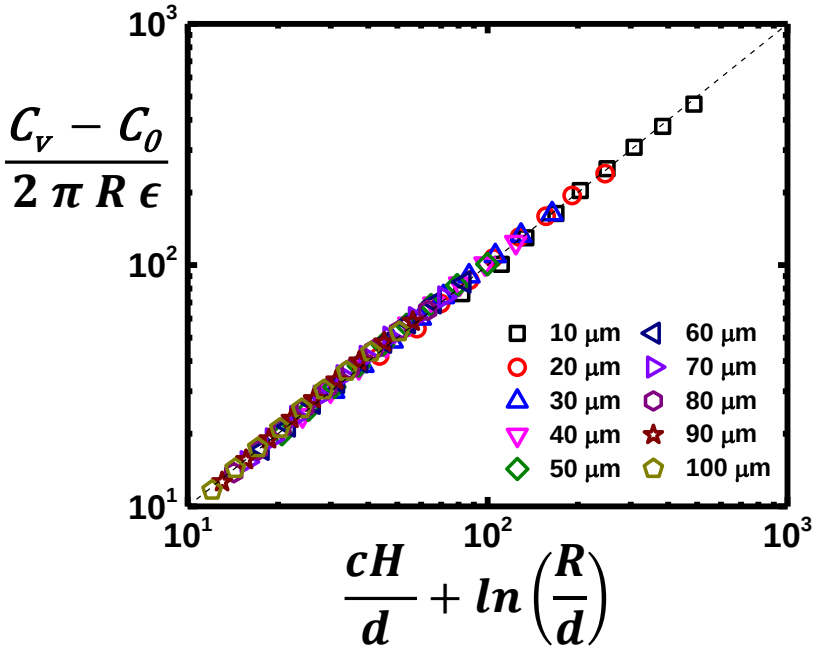

Figure 2.7: Capacitance data from the COMSOL model [25] using a range of values for H and d. Symbols correspond to different values of d. The dashed line is Eq. 2.4, with $c = 0.58$ and $C_0 = 1.85$ pF.

On average, a stable vapor layer formed at $T_+ = 240 \pm 30°$C, which is consistent with recent theoretical predictions for metallic surfaces [123]. Nevertheless, once formed, the vapor layer remained stable at temperatures well below T_+. As shown in **Fig. 2.8**, the collapse of the vapor layer occurred repeatedly at $T_- = 140 \pm 10°$C.

The collapse of the vapor layer at T_- is explosive and audible. We used synchronized high-speed video (Phantom V7.11, Vision Research) to visualize this process. **Figure 2.9a&b** show the real and imaginary parts of the impedance (dashed box in **Fig. 2.3a**) before and after a single collapse event. The bubbles generated during the explosion lead to a large increase in resistance before eventually returning to quiescence at long times. The slightly smaller resistance after collapse was due to the increased water temperature from the heated electrode. For some values of H, we observed capillary waves that traveled upwards along the vapor layer. These manifested as oscillations in the reactive impedance (**Fig. 2.9b**). The capillary waves are

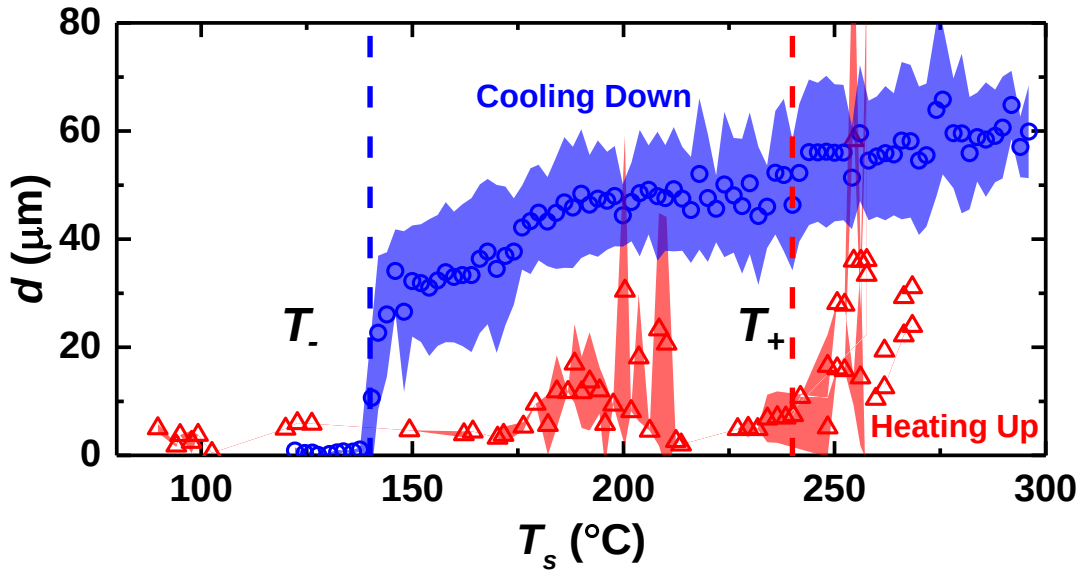

Figure 2.8: d versus T_s for a nickel-coated copper electrode in pure water. The electrode was first heated (red triangles) and then subsequently cooled (blue circles). $T_+ = 240 \pm 30$°C (red dashed line) was the average temperature when the vapor layer formed, and $T_- = 140 \pm 10$°C (blue dashed line) was the average temperature when the vapor layer collapsed. The shaded regions show the standard deviation from multiple experiments.

visible with a typical wavelength of λ = 2-3 mm. We can estimate the corresponding frequency using the dispersion relation for pure capillary waves, $f = (\gamma k^3/\rho_l)^{1/2}/2\pi \approx$ 120-220 Hz, where $\rho_l = 959$ kg/m^3 is the density of pure water at the boiling point, and $k = 2\pi/\lambda$ is the wave vector. This agrees well with **Fig. 2.9b**, where $f \approx 200$ Hz.

During collapse, the combined capacitance, $C_v + C_\lambda$, increases by more than 3 orders of magnitude (**Fig. 2.10**), and is facilitated by an explosive wetting front spreading from the initial contact point. The speed of this front is consistent with the capillary velocity, $\gamma/\eta_w \approx 210$ m/s, where $\gamma = 59$ mN/m is the liquid-vapor surface tension and $\eta_w = 0.28$ mPa·s is the viscosity of water at the boiling point. The large increase in capacitance is due to the formation of an ionic double layer as soon as the liquid contacts the surface, made possible by the addition of salt in the water (**Fig. 2.5**). The effective thickness of the ionic screening layer (1-10 nm [56])

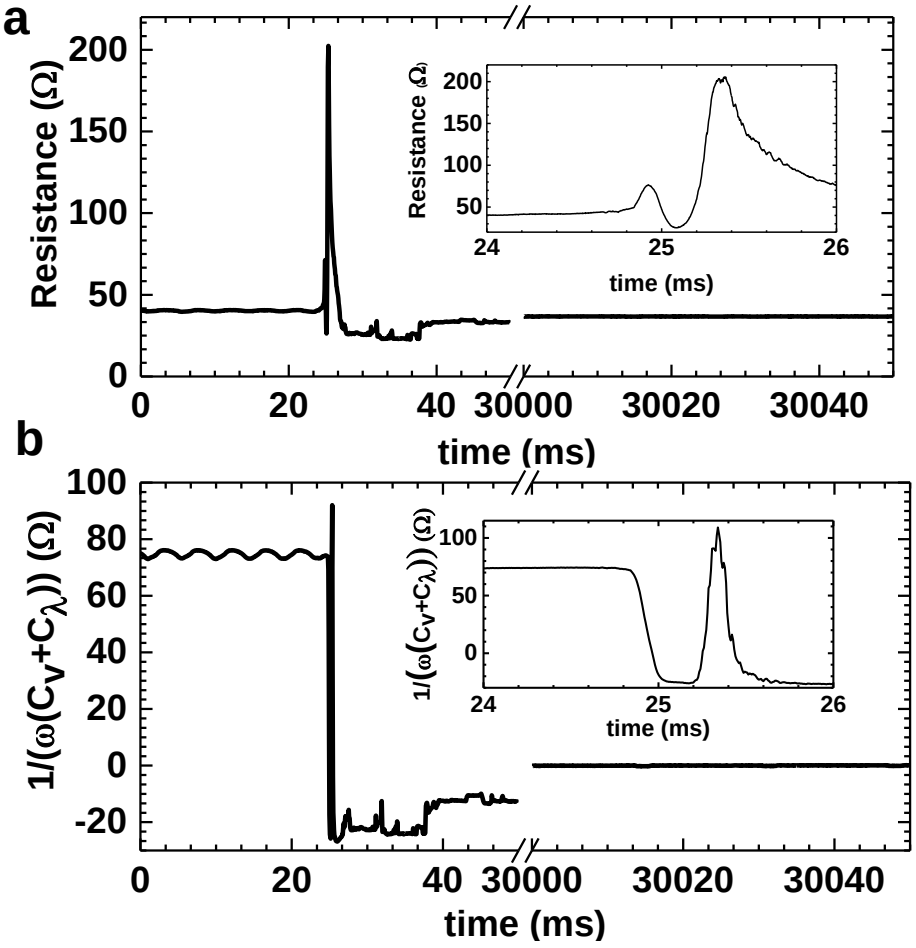

Figure 2.9: Resistance (a) and capacitive reactance (b) of the Leidenfrost cell during collapse with 0.02 M NaCl. The insets show 2 ms of the data right before and after collapse. 30 s after collapse, the system is quiescent. Capillary waves are visible as oscillations in the reactance prior to collapse.

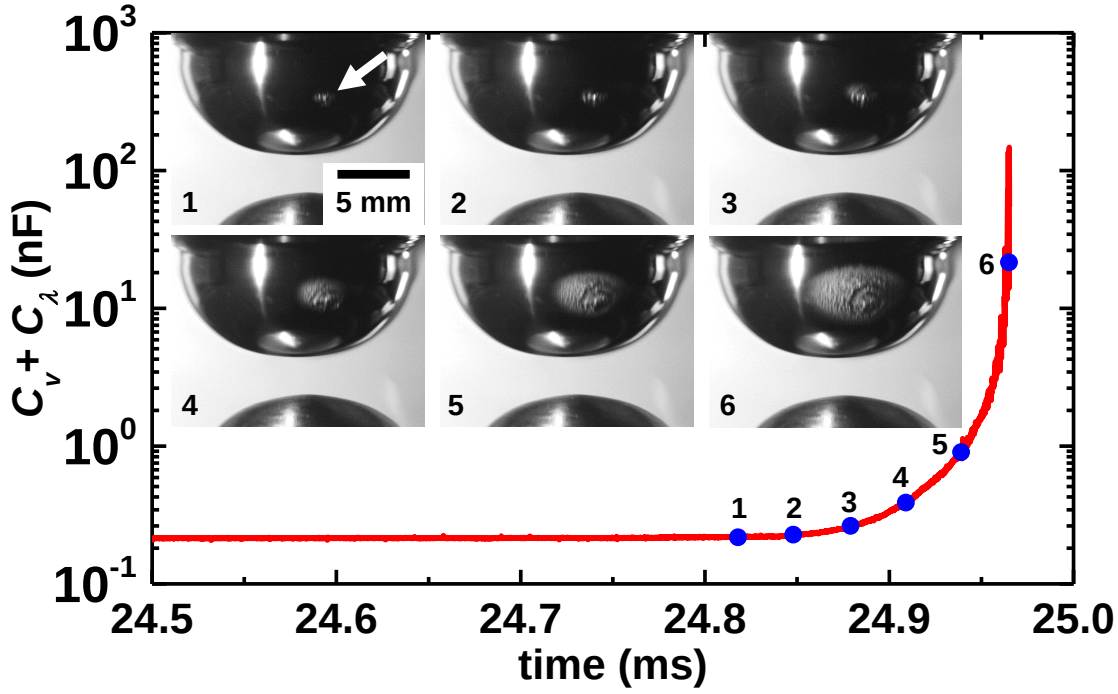

Figure 2.10: Total capacitance of the liquid-vapor-solid interface just before collapse. The enormous increase is due to the formation of an ionic double layer at the liquid-solid contact. The images show a time sequence of the initial collapse point, as indicated by the arrow, where bubbles are generated as the wetting front spreads rapidly. The blue points in the data correspond to the indicated images.

is 3 orders of magnitude smaller than the thickness of the vapor layer, resulting in a much larger capacitance. Thus, even a small fraction of liquid touching the electrode surface will drastically increase the capacitance. The slower decay in the impedance is due to the dissipation of a large cloud of vapor bubbles.

Surprisingly, and in contrast to the strong dependence of T_+ on material properties [123], we found that T_- was independent of the metal used for the heated electrode. **Figure 2.11a** shows d versus T_s for 3 representative experiments with metals of varying thermal conductivity: titanium (7 W/m·K), brass (115 W/m·K), and copper (390 W/m·K). For each material, the time evolution of T_s looked distinct due to differences in heat capacity (**Fig. 2.12**), yet d only depended on T_s. The discontinuities in the data at lower temperatures mark the failure of the vapor layer and determine both T_- and the spatially-averaged vapor layer thickness at collapse, d_c. These values were independently measured in each experiment. **Figure 2.11b** shows T_- and d_c for different metals, liquid levels H, and aqueous salt concentrations. A larger thermal conductivity resulted in slightly larger values of d_c. We speculate that localized cooling near the liquid interface [110] could result in a smaller vapor layer thickness near the tip of the electrode for metals with lower thermal conductivity. However, the stability of the vapor pocket should be mostly determined by the gas flux through the "neck" region [98], where the vapor layer opens up to ambient pressure.

Furthermore, both T_- and d_c were nearly independent over the range 3.7 mm $< H <$ 7.6 mm (**Fig. 2.13**), which is consistent with the behavior of Leidenfrost drops shown in **Fig. 2.1b**. This range of H corresponded to vapor layer surface areas of 89-210 mm^2, as computed from the geometric model (**Fig. 2.6**). Although we did not investigate metal geometries with $R \lesssim l_c$, we would expect a significant drop in T_- in this regime due to a lack of vapor layer fluctuations [17, 21]. In the next chapter we did see this expected decrease in T_- with simulations with smaller geometries.

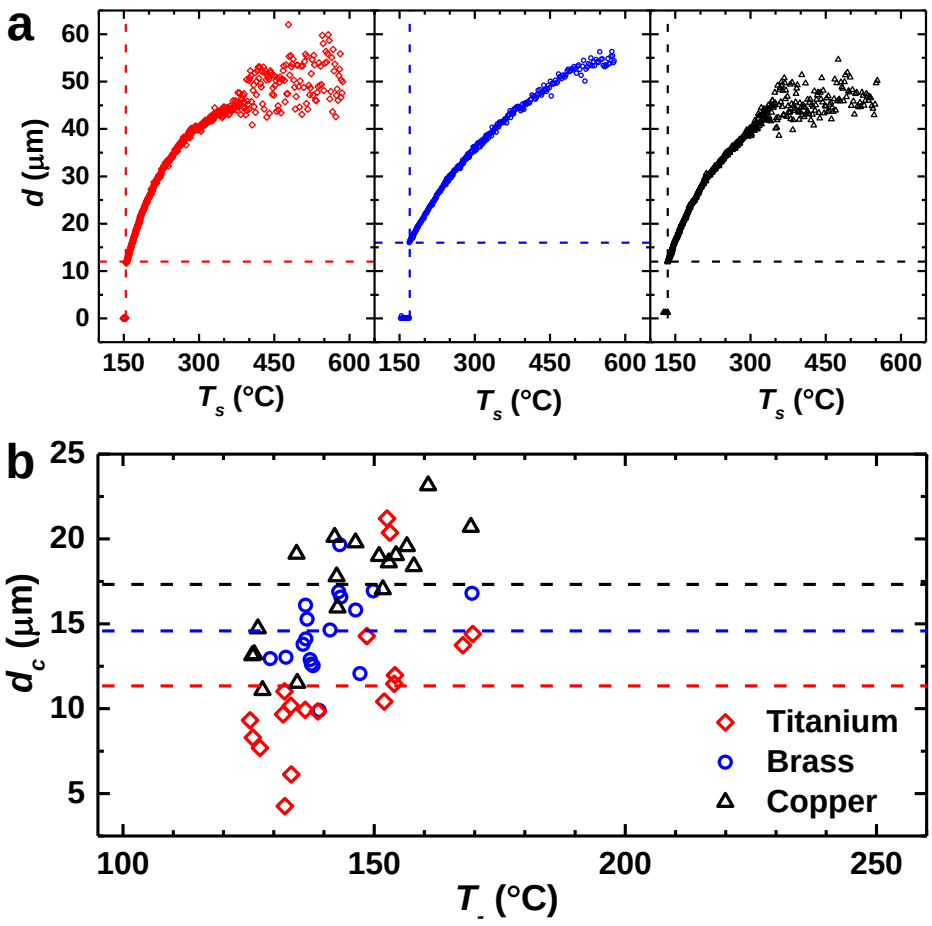

Figure 2.11: (a) Spatially-averaged vapor layer thickness, d, as a function of substrate temperature, T_s, during the cooling of titanium, brass, and copper electrodes. The visible discontinuities in the data, indicated by the dashed lines, correspond to vapor layer failure at temperature T_- and thickness d_c (b) Thickness at failure, d_c, as a function of the temperature at failure, T_-. Each data point represents varying aqueous NaCl concentrations and liquid level H for each metal. The dashed lines show the mean value of d_c for each metal, while the average of T_- was 140 ± 10°C for all experiments.

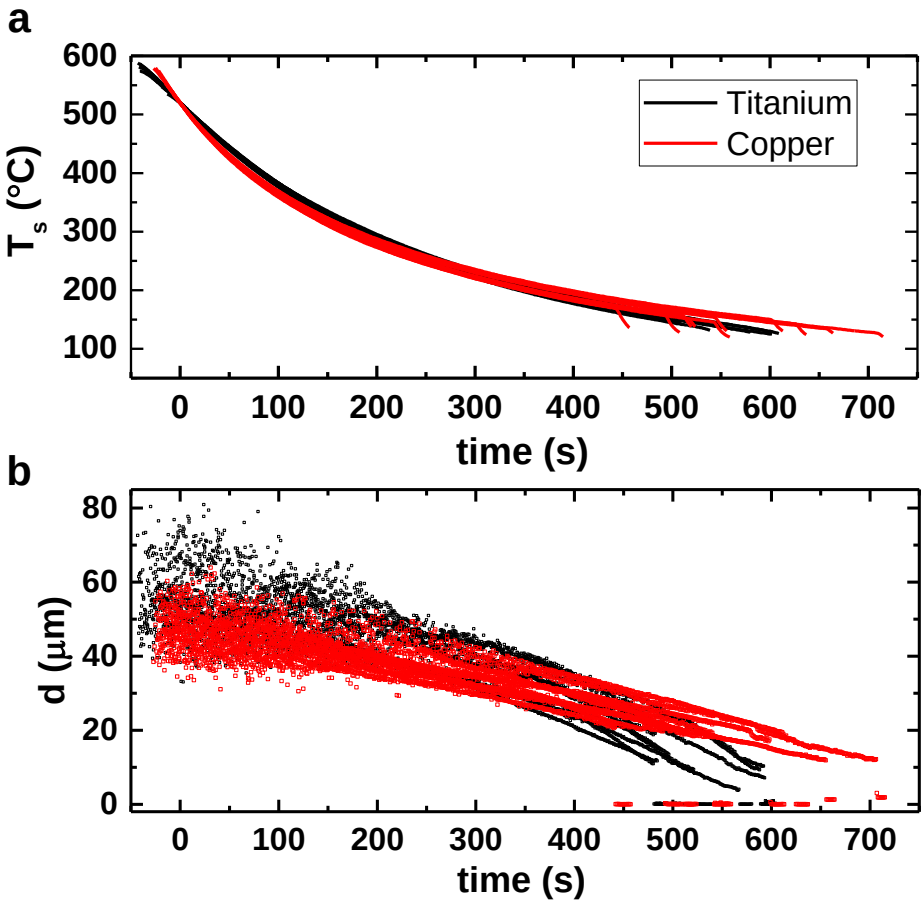

Figure 2.12: Series of individual experiments showing the surface temperature T_s versus time for titanium and copper (a), and the thickness d versus time for titanium and copper (b). All data have been shifted in time so that $T_s = 520°\text{C}$ at the origin. Black (Red) lines and dots are for titanium (copper) experiments. There are slight differences between the two metals in the time series due to their heat capacity. Failure occurred at nearly the same T_- for both metals.

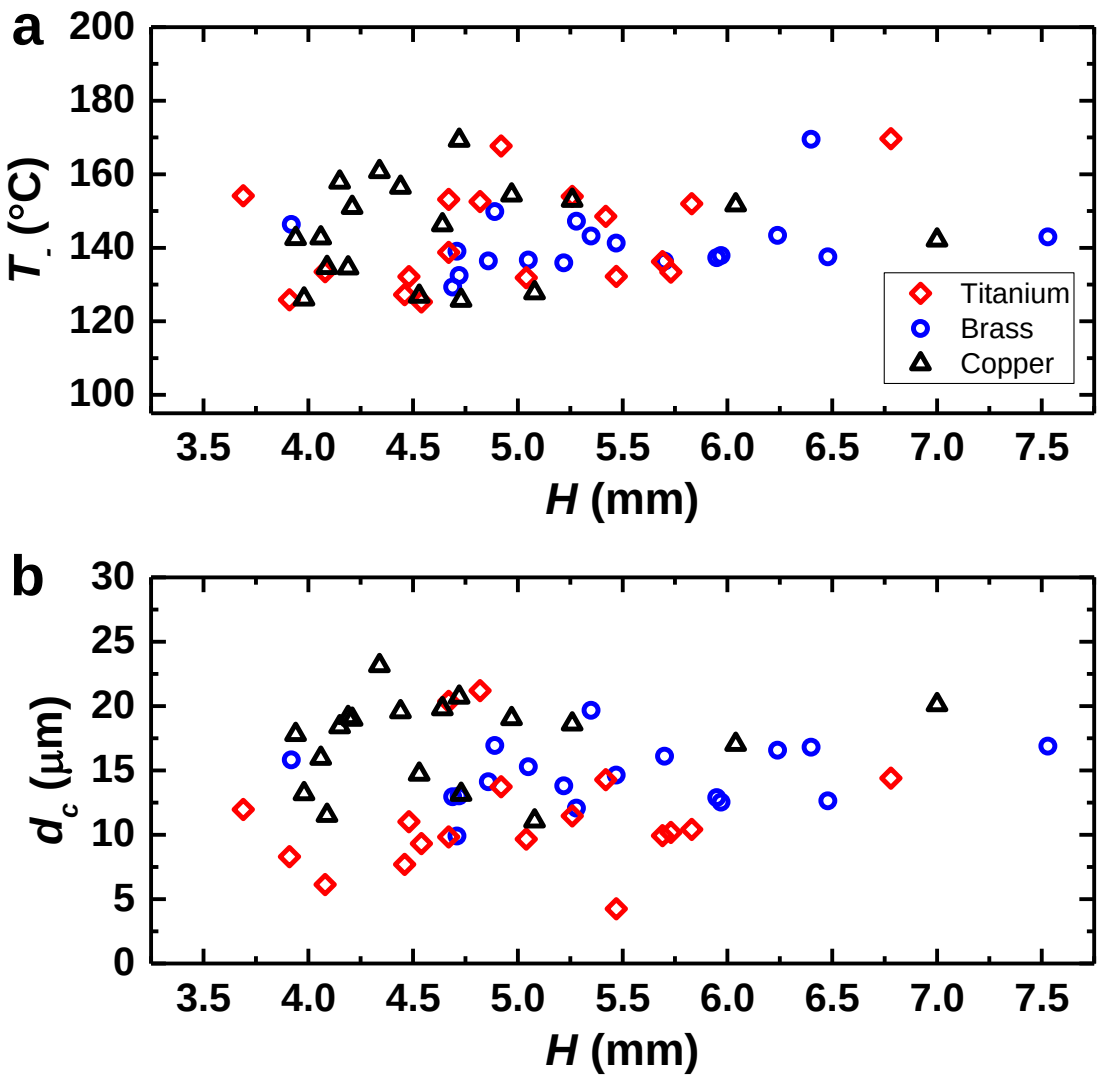

Figure 2.13: The failure temperature, T_- (a), and the thickness at failure, d_c (b), as functions of the immersion depth, H. Data are shown for 3 materials, as indicated in the legend.

Additionally, T_- and d_c showed no dependence on NaCl salt concentration (**Fig. 2.14**). The addition of salt is widely known to suppress Leidenfrost phenomena [45, 1, 44], despite the fact that NaCl concentrations even up to sea water do not strongly affect the vapor pressure [34], evaporation rate, boiling point, viscosity [55], or surface tension of water [49]. Taken together, these measurements suggest that the minimum Leidenfrost temperature is determined by the hydrodynamic stability of the vapor layer. For water, failure reliably occurs at $T_- = 140 \pm 10°\text{C}$ and $d_c \approx$ 10-20 μm.

2.3 Chapter conclusions

Although Leidenfrost vapor layers require a material-dependent elevated temperature (T_+) for formation, here we showed how vapor layers can be stable at a much lower temperature (T_-) that is nearly independent of material and liquid properties. These two temperatures can be separated by more than 100°C, leading to a large hysteresis and an explosive collapse at low temperatures. This study inherently poses outstanding questions surrounding the initiation of vapor layer collapse, either through unsteady hydrodynamic fluctuations or surface roughness. The liquid interface must approach the surface on sub-micron length scales for short-ranged van der Waals forces to initiate contact and wetting [123]. We suspect that in highly-dynamic geometries where the vapor layer is constantly in motion, hysteresis may not be visible due to repeated liquid-solid contacts [50]. Nevertheless, this study explains the surprising robustness of Leidenfrost vapor layers once they are formed, and the physics that determines their violent demise.

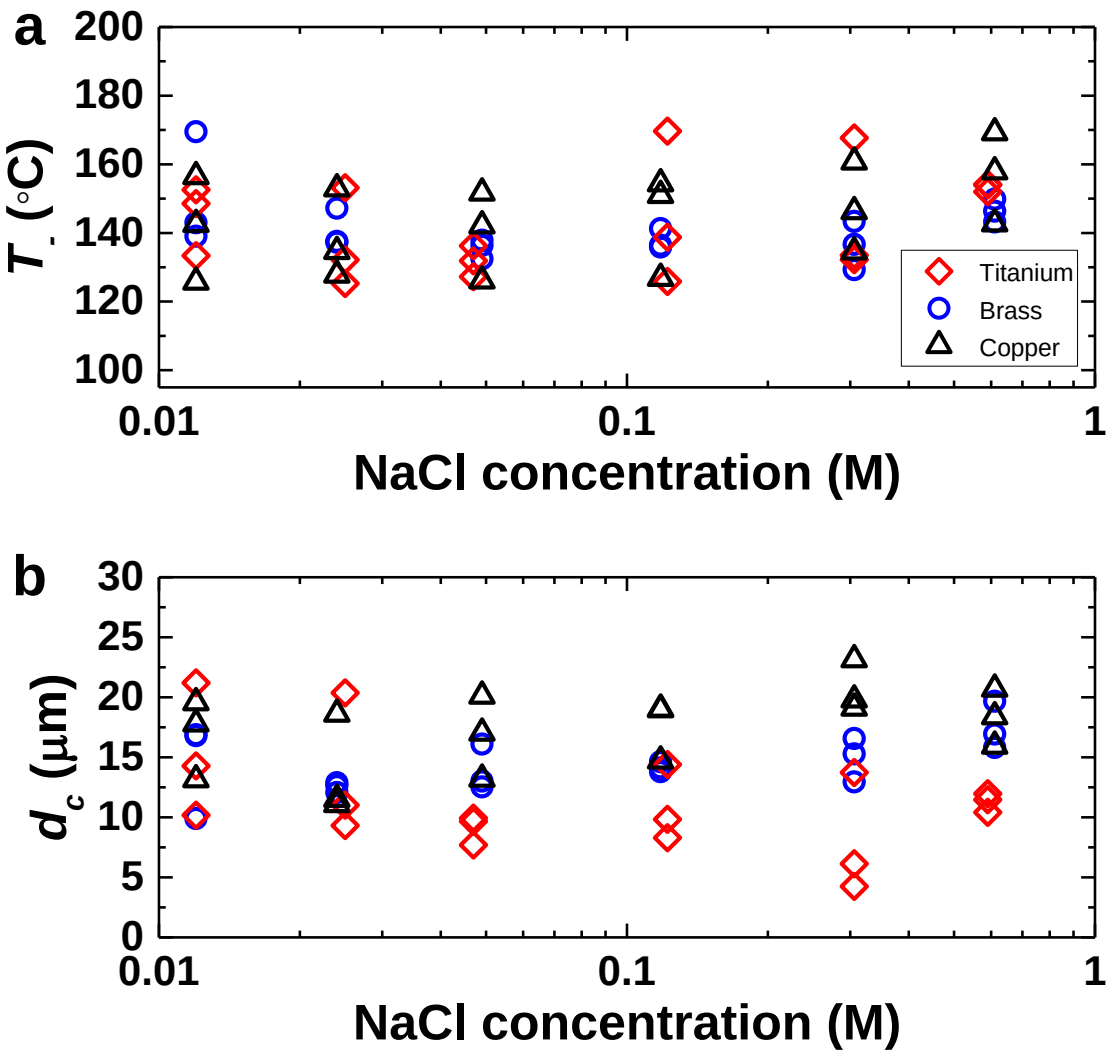

Figure 2.14: The failure temperature, T_- (a), and the thickness at failure, d_c (b), as functions of NaCl concentration. Data are shown for 3 materials, as indicated in the legend.

2.4 Leidenfrost thickness measurement technique

2.4.1 Sampling Protocol

We used the same carrier wave frequency for all experiments, however, we sampled the data differently. For short time scales, we used a sampling rate of 200 MS/s for 50 ms of data, for a total of 10 MS (here "MS" refers to "Megasamples"). This is equivalent to 20 sampled points per cycle for the 10 MHz carrier wave. We wrote a custom LabVIEW program that acts as a lock-in amplifier to extract the 10 MHz amplitude for each cycle, resulting in a total of 500,000 data points for the data shown in **Fig. 2.9 & 2.10**. For some experiments, such as those shown in **Figs. 2.8 & 2.11**, the thickness, d, is measured over many minutes. For these measurements, we averaged 800 samples at 100 MS/s to calculate the thickness of the vapor layer in 1 s intervals. Additionally, T_s and T_l were also measured every second. Measurements could not be made while the heater was turned on. We used a resistive heater attached to a 60 Hz variac tuned to 80 to 120 V. This was enough to interfere with the carrier signal of the electrical thickness measurement. While this does not matter for cooling experiments, it limited our sampling of hysteresis data. Upon heating, the heater had to be turned off to allow a few seconds of thickness measurements before being turned back on. This was repeated until a vapor layer formed, at which point the heater was turned off and constant thickness measurements could be made as the metal cooled until vapor layer failure.

2.4.2 Capacitor model of the vapor layer

To measure Z_{unknown}, and ultimately the thickness of the vapor layer, we solved the telegraphers equations on each cable, and matched the boundary conditions at Z_{unknown} and the attenuator (**Fig. 2.4**). We ignored losses and assumed a capacitance, C_c, and inductance, L_c, per unit length of cable. Along the length x of each

cable, the voltage V and current I are determined by:

$$\frac{dV}{dx} = -L_c \frac{dI}{dt}, \tag{2.6}$$

$$\frac{dI}{dx} = -C_c \frac{dV}{dt}. \tag{2.7}$$

Assuming a plane wave ansatz, $V = V_c e^{i(k_c x - \omega t)}$ and $I = V/\sqrt{L_c/C_c}$, where V_c is the amplitude, k_c is the wave vector, and $\omega = 2\pi f$ is the angular frequency, we solved for the real and imaginary components of Z_{unknown}, Z_R and Z_I, respectively.

Taking the real part of the signals, we found the resulting expressions for Z_R and Z_I in terms of the measured signals (CH0 and CH1, **Fig. 2.4**). For each channel, the voltage can be written as a sum of the sine and cosine parts:

$$V_0 = A_0 \cos\omega t + B_0 \sin\omega t \tag{2.8}$$

$$V_1 = A_1 \cos\omega t + B_1 \sin\omega t. \tag{2.9}$$

A custom LabVIEW program extracts A_0, A_1, B_0, and B_1 for each cycle of oscillation of the 10 MHz carrier wave. Thus, the amplitudes are sampled every 100 ns. Z_R and Z_I are then computed using the following relations:

$$Z_R = \frac{-R_{in}}{A_0^2 + B_0^2}\Bigg(A_0^2 - A_0 A_1 A_F + B_0(B_0 - A_F B_1) + A_F(A_1 B_0 - A_0 B_1)\tan\left(\frac{S\omega}{v}\right)\Bigg), \tag{2.10}$$

$$Z_I = \frac{R_{in}}{A_0^2 + B_0^2}\Bigg(- A_1 A_F B_0 + A_0 A_F B_1 + (A_0^2 - A_0 A_1 A_F + B_0(B_0 - A_F B_1))\tan\left(\frac{S\omega}{v}\right)\Bigg). \tag{2.11}$$

where $R_{\text{in}} = 50\ \Omega$ is the input impedance of the oscilloscope channels, $S = S1 = 1.1$ m, $v = 0.65c$ is the wave speed on the cable (relative to the speed of light c), and

$A_F = 2.02$ is the measured voltage attenuation ratio for the 6 dB attenuator.

Ultimately we wanted to relate Z_R and Z_I to R_0, C_v, and C_λ, as shown in **Fig. 2.3a**. Since C_v and C_λ are summed in parallel, we could only measure the total capacitance $C_v + C_\lambda$. Thus, R_0 and $C_v + C_\lambda$ can be written as:

$$R_0 = Z_R, \tag{2.12}$$

$$C_v + C_\lambda = \frac{1}{\omega(Z_I + L_0\omega)}. \tag{2.13}$$

While $C_v + C_\lambda$ and R_0 are functions of time, we assumed the parasitic inductance L_0 was constant. In order to measure L_0 in experiments, we used the fact that the impedance associated with C_λ is almost negligible when there is a fully-formed double layer. The length scale associated with charge separation is $\lambda \approx 1-10$ nm [56], which is more than 3 orders of magnitude smaller than the typical vapor layer thickness d (**Fig. 2.5**). Prior to collapse, there is no liquid-solid contact so $C_\lambda = 0$. Well after collapse, when there is significant liquid-solid contact, $C_v = 0$ and $C_\lambda < 3$ μF for the centimeter-scale electrodes in our experiment [56]. At $f = \omega/2\pi = 10$ MHz, the corresponding impedance is $1/|\omega C_\lambda| < 0.045$ Ω. Thus, we could ignore the impedance due to C_λ and assume $L_0 = Z_I/\omega$ when there is a double layer. For our experiments, $L_0 \lesssim 1$ μH. We then used this measured value of L_0 for each experiment and applied it to data before, during, and after the collapse.

Chapter 3

Inertial Leidenfrost Collapse

In the last chapter we saw that Leidenfrost vapor layers fail due to a hydrodynamic instability. In this chapter, I will discuss simulations I preformed using COMSOL Multiphysics to investigate the nature of the instability [25]. Work presented in this chapter is in preparation of my third first author paper.

3.1 Leidenfrost simulations couple many physics concepts

A Leidenfrost vapor layer separates a hot solid from an evaporating fluid. While experiments have elucidated a vast array of interesting phenomena involving Leidenfrost vapor layers, direct measurements of the gas-fluid and gas-solid interfaces have been limited. It was determined in the last chapter that surface waves incited vapor layer collapse [42], **Fig. 3.1**. For the geometry used in chapter 2 the instability was independent of the thermal properties of the solid or the salt concentration of the fluid, **Fig. 3.2**. Computational work was required to confirm our experimental results and investigate the nature of the instability.

Investigating Leidenfrost dynamics computationally requires interplay between

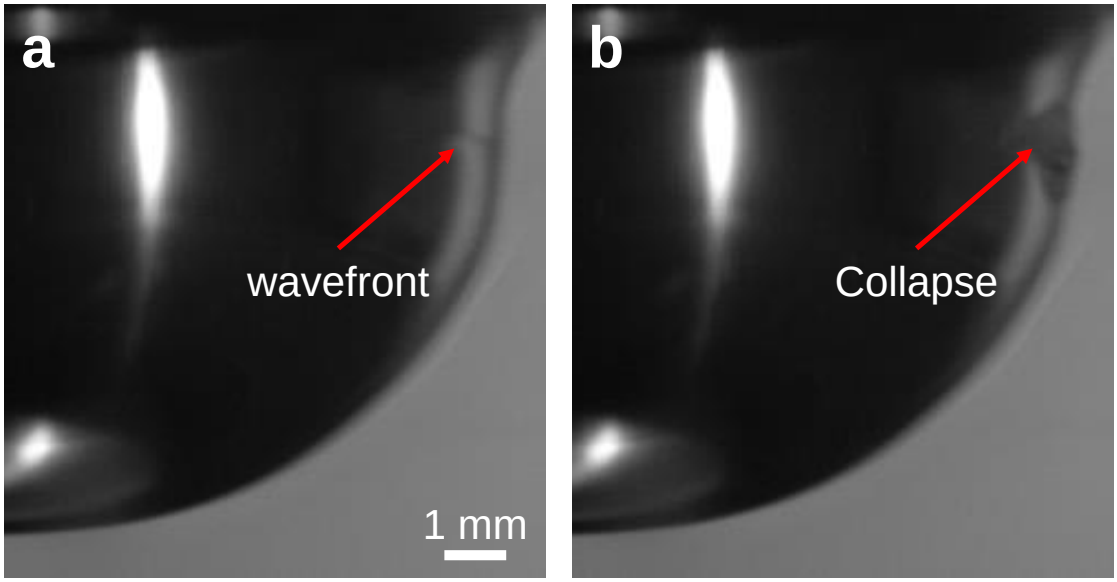

Figure 3.1: (a) Experimental picture of the wavefront instability that leads to the collapse of the vapor layer pictured in (b).

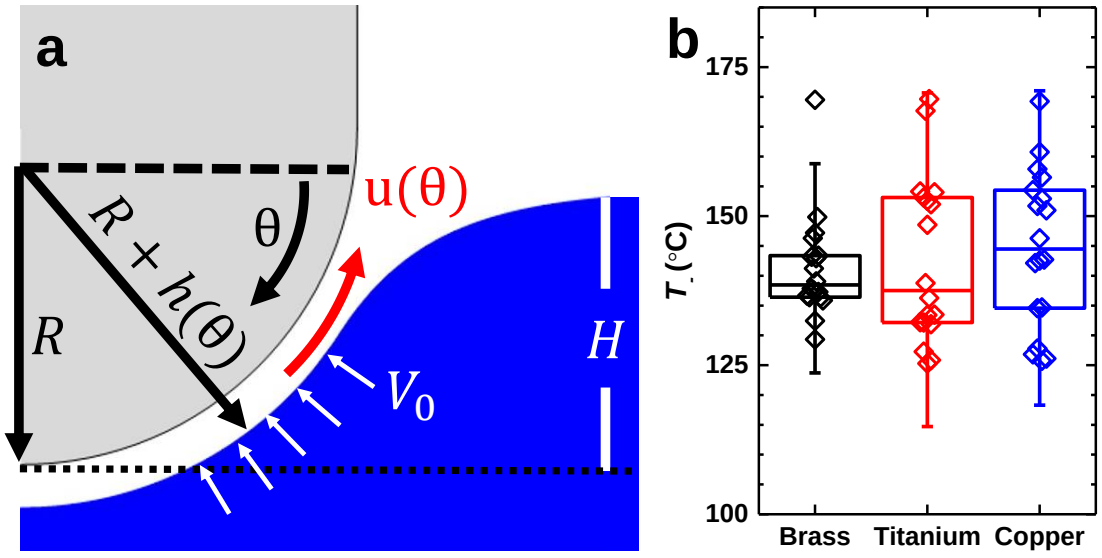

Figure 3.2: (a) Inverse Leidenfrost schematic. R is the radius of the hot object, θ is the angular coordinate measured from 0 to $\frac{1}{2}\pi$ as indicated by the arrow, $h(\theta)$ is the thickness of the vapor layer, H is the height from the tip of the hot object to water level, and v_0 and $u(\theta)$ are the evaporation velocity and flow velocity used in the lubrication model. (b) Hair and Whisker distribution of experimental values of the failure temperature, T_{-}. $T_{-} \approx 140°\text{C}$ for all materials tested.

rapid evaporation, liquid super heating/cooling, local solid cooling, and length-scales from μm to cm. Selective assumptions, made to reduce computational costs, limit previous studies to stable steady-state systems. These simulations match the geometry of stable Leidenfrost drops with experiments very well [6, 23, 10, 17]. However, approximations made for steady-state geometries become invalid as the vapor layer thins near failure. In particular, lubricating flow in the vapor and uniform temperature in the fluid.

Here, we solve the full Navier-Stokes equations to produce the fluid flows:

$$\frac{\partial \vec{v}}{\partial t} + (\vec{v} \cdot \vec{\nabla})\vec{v} = g - \frac{1}{\rho}\vec{\nabla}p + \mu\vec{\nabla}^2\vec{v}. \tag{3.1}$$

In COMSOL, to allow for gradients in μ the equations are defined as follows with the corresponding incompressibility equation:

$$\rho\frac{\partial v}{\partial t} + \rho(v \cdot \nabla)v = \nabla \cdot [-p + \mu(\nabla v + (\nabla v)^{\mathrm{T}})] + \rho g, \tag{3.2}$$

$$\rho\nabla \cdot v = 0, \tag{3.3}$$

where v is the velocity, g is gravity, ρ is the density of the fluid, p is the pressure, and μ is the dynamic viscosity of the fluid. Steady-state solutions separate the fluid dynamics of a droplet into a lubrication approximation on the bottom, encompassing the vapor layer (10-100 μm thick) and the boundary fluid, and a Navier-Stokes fluid on the top with a boundary matching point [6, 23]. A lubrication approximation neglects the inertial terms of the Navier-Stokes equations and instead solves the simpler set of equations:

$$\nabla p = \nu\nabla^2 v, \tag{3.4}$$

where it is further assumed that v is a parabolic function of the vapor layer thickness.

However, surface waves indicate a dynamic velocity profile, **Fig. 3.1**, therefore, we cannot approximate the vapor layer as a steady-state lubricating flow near failure.

Another common approximation for steady-state solutions is to have a uniform temperature in the fluid, which decreases fluid flow (convection) and more importantly eliminates the computational costs of evaporation (energy consumption), heat transfer, phase mixtures, and phase boundary conditions [23]. We did not want to neglect any fluid flows that may lead to surface waves, so could not assume a uniform temperature. Here, we combined two-phase laminar flow, nonisothermal heat transfer, and evaporation in a COMSOL Multiphysics simulation to examine the failure mechanism of Leidenfrost vapor layers upon cooling. Using the full fluid flow we can match stable interface profiles with previously used lubrication models while matching the failure temperature, T_{-}, with experimental results of the same geometry shown in **Chapter 2**. Furthermore, our simulations highlight the importance of inertia, assumed negligible for steady-state solutions, in driving vapor layer failure.

3.2 COMSOL simulation Details

We simulated a 2-D axisymmetric inverse Leidenfrost system. Combining all the necessary physics modules is computationally expensive, but necessary to investigate all possible causes for the instability leading to vapor layer failure. The geometry space is a 40 $\times$ 40 mm box with a solid hot object (rod with a spherical tip) placed at the symmetry boundary, $r = 0$ mm, **Fig. 3.3a**. The bottom tip of the hot solid is fixed at $z = 22$ mm and the initial water height is $z = 21$ mm. The surface area of the vapor layer is controlled by varying the radius of the hot object, $2 \leq R \leq 16$ mm and the water level $0.5 \leq H \leq 17$ mm, **Fig. 3.2a**. To suppress overheating and limit wall boundary effects, the boundary at $r = 40$ mm is held at 70 °C with a slip condition (no restrictions on tangential velocity).

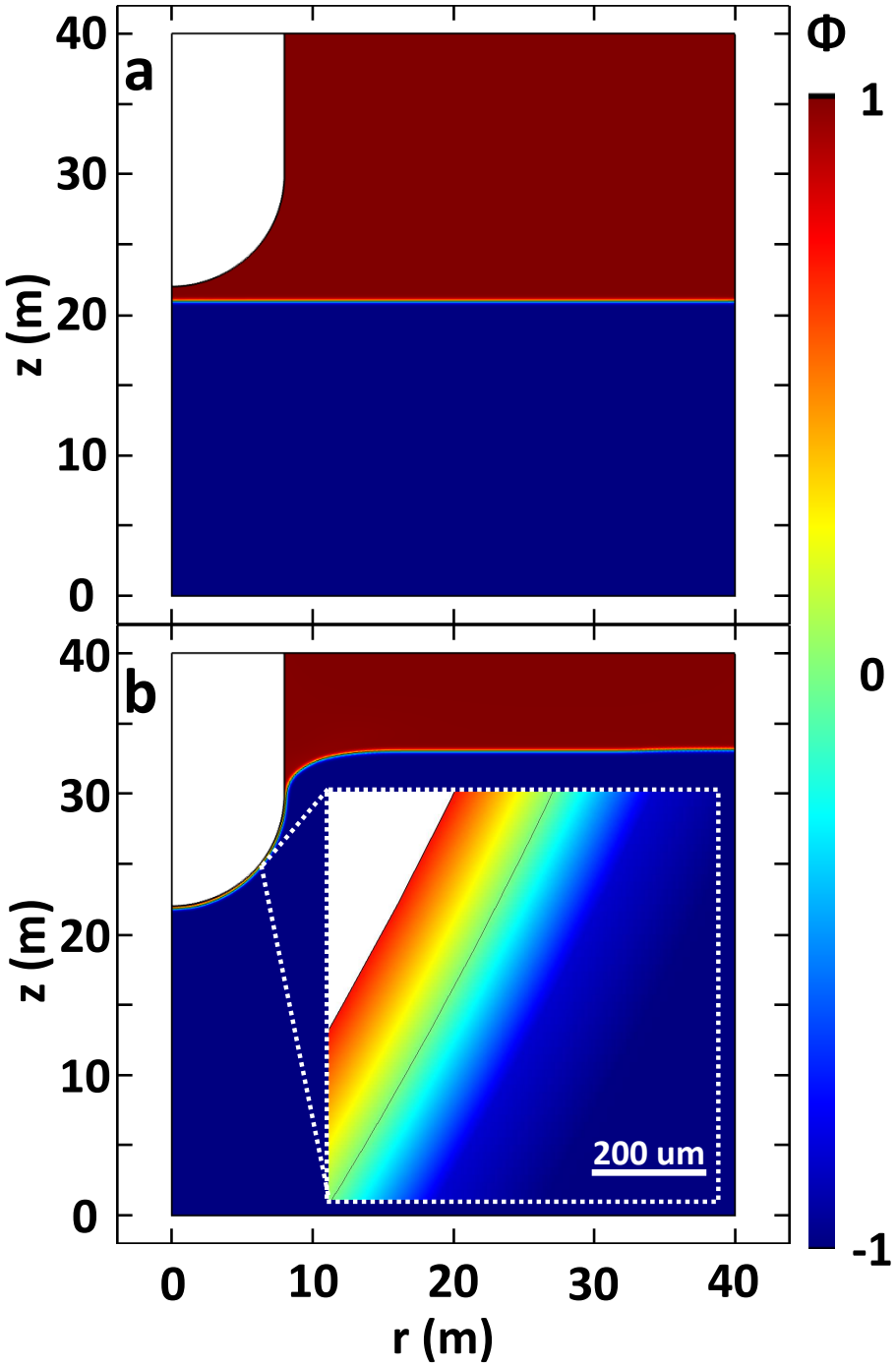

Figure 3.3: Characteristic simulation frame for a copper hot object of $R = 8$ mm and a water height of $H = 14$ mm. The color scale denotes the volume fraction of the gas as 1, red, and fluid as -1, blue. The simulation size is 40×40 mm with a mesh size in the fluid of 2.25 μm - 195 μm and in the solid of 3 μm - 800 μm.

Parameter	Expression	units	Description
Mw	0.018	kg/mol	Molecular weight of water
L	$42000/Mw$	J/kg	Latent heat of vaporization
Cp_l	4200	J/(kg·K)	Specific heat of liquid water
Cp_v	1840	J/(kg·K)	Specific heat of water vapor
T_{sat}	373	K	Saturation temperature
k_l	0.63	W/(m·K)	Thermal conductivity of water
ρ_l	1000	kg/m^3	density of water
ρ_v	(p0·Mw)/(8.314·(T+eps))	kg/m^3	Density of water vapor
R_T	0.001	m/s	tuning parameter
$hmax$	195	μm	maximum grid size
$p0$	101325	Pa	Atmospheric pressure
μ_l	2.82E-2	Pa · s	dynamic viscosity of the fluid
μ_v	1.3E-4	Pa · s	dynamic viscosity of the gas

Table 3.1: Simulation parameters

In the fluid domain we consider in-compressible flow with gravity and the non-conservative phase field equations. The non-conservative form must be used to avoid excessive convergence times while maintaining accurate results for our simulations, which have a fluid domain mesh size of 2.25 μm - 195 μm [100, 24]. In the solid we found a mesh size of 3 μm - 800 μm was sufficient. Evaporation is added to the system as a heat source, Q_s, defined in the literature as [47, 91]:

$$Q_s = -\dot{\mathrm{m}} L \delta, \tag{3.5}$$

where L is latent heat of vaporization of water defined in **Table 3.1**. The rate of vaporization, $\dot{\mathrm{m}}$, and the interface delta function, δ are defined as:

$$\dot{\mathrm{m}} = \begin{cases} R_T \rho_v \dfrac{T - T_{sat}}{T_{sat}}, & \text{if } T < T_{sat}, \\ \\ R_T \rho_l \dfrac{T - T_{sat}}{T_{sat}}, & \text{otherwise}, \end{cases} \tag{3.6}$$

and

$$\delta = 6Vf_l(1 - Vf_l)0.5\sqrt{\phi_r^2 + \phi_z^2 + eps}. \tag{3.7}$$

Here T_{sat}, ρ_v, and ρ_l are real values defined in **Table 3.1**, $R_T = 0.001$ m/s is a tuning parameter, *eps* is a small mathematical number to ensure there are no divisions by 0 when using δ [47], T is the temperature of the fluid, Vf_l is the volume fraction of water, and ϕ_r and ϕ_z are the r and z components of the phase field variable. Similar equations for $\dot{m}$ and δ are used by Jafari *et al.* to successfully simulate a growing vapor bubble in a confined tube [47].

Variable	Expression	units	Description
k_v	8.32E-5 · T-7.46E-3	W/(m·K)	thermal conductivity of vapor
κ	(k_l-k_v)(V_l+k_v)	W/(m·K)	thermal conductivity for two-phase flow
Cp	(Cp_L-Cp_v)V_l+Cp_v	J/(kg·K)	specific heat for two-phase flow

Table 3.2: Variables

A weak expression, W_k in the fluid domains helps further smooth results. W_k = test(ψ) ϕ_s+test(p) u_s, where test() is a localized sampling function, $\phi_s = -\dot{m}\delta(Vf_v/\rho_v + Vf_l/\rho_l)$ is the source term of the phase field equation, p is the pressure, $u_s = \dot{m}\delta(1/\rho_v - 1/\rho_l)$ is the source term in the continuity equation, Vf_v is the volume fraction of the vapor, and $\psi = -\vec{\nabla} \cdot \epsilon_{pf}^2 \vec{\nabla}\vec{\phi} + (\phi^2 - 1)\phi + \frac{\epsilon_{pf}^2}{\lambda}\frac{\partial f}{\partial \phi}$ is the phase field help variable, where ϵ_{pf} is the interfacial thickness variable and $\lambda = \frac{3\epsilon_{pf}\sigma}{\sqrt{8}}$. The help variable helps describe the interfacial free energy between the two phases [88, 47]. All other variables are defined in **Table 3.1**.

To initialize a simulation we defined the hot solid thermal properties, **Table 3.3** and chose the hot solid starting temperature, 650 K except in cases where an increased initial temperature was required (large values of H and low thermal conductivity materials). The water and vapor temperatures were set to 90°C and 110°C respectively. An ambient pressure outlet at $z = 40$ mm allows gas to escape, while the inlet at $z = 0$ mm has a variable pressure, P giving the phase field frame shown in **Fig. 3.3a**. P

is initialized and held for 1s at $P = P_0 = \rho_l g z$, where $z = 21$ mm, $\rho_l = 1000$ kg/m^2, and $g = 9.8$m/s^2. The condition changes to $P = 5 * t + P_0$, which raises the water height until $P = P_0 + \rho_l g(H + 1$ mm), where H is the desired water height above the tip of the hot object, **Fig. 3.3b**. As the water level rises a vapor layer spontaneously forms around the hot object without any fluid or geometric constraints. Furthermore, a pressure boundary helped minimize the effects of using the non-conservative mass equations by allowing as much water as needed into the chamber to maintain H.

Material		$\kappa \frac{W}{m \cdot K}$	$\rho \frac{kg}{m^3}$	$C_p \frac{J}{kg \cdot K}$
Copper	Cu	386	8940	385
Aluminum	Al	247	2710	897
Iron	Fe	60	7800	449
Titanium	Ti	7	4420	540
Glass		0.8	2500	792

Table 3.3: Thermal properties of the simulated hot object.

The simulation continues unhindered until the vapor layer fails as shown in the time sequences for copper, aluminum, and titanium hot objects with $R = 8$ mm and $H = 8$ mm, **Fig. 3.4 - 3.6** respectively. From left to right are the phase, ϕ, velocity, v (m/s), and temperature, T (K), fields at the indicated times. The color map for the three fields are such that, red indicates $\phi = 1$ (gas), $v = 0.2$ (m/s), and T = 650 K, while blue indicates $\phi = -1$ (water), $v = 0$ (m/s), and T = 350 K.

3.3 Lubrication model details

We can compare the stable state solutions of the COMSOL Multiphysics simulations to a lubrication approximation to ensure the validity of the COMSOL model. Nearly identical models have been used for the air flow under a levitated drop in stable conditions [70, 98, 30]. In particular, predictions from Snoeijer et al. [98] show excellent agreement with experiments of Leidenfrost drops [17]. The lubrication approximation balances the leading order pressure gradient terms driving the tangential flow in the

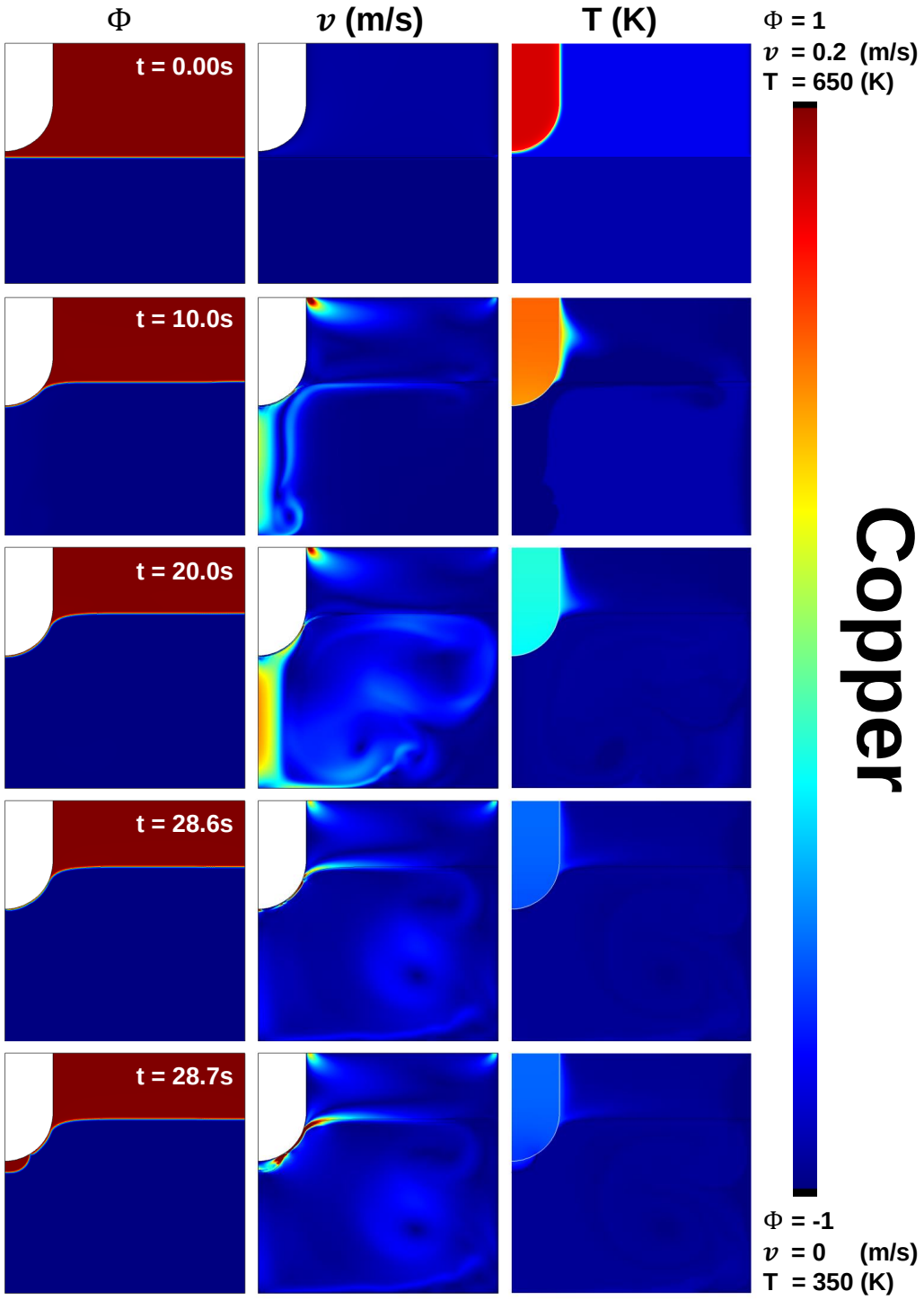

Figure 3.4: A time series of an $R = 8$ mm Copper object from top to bottom. From left to right is a phase field, velocity, and temperature field at the same time. The color map is $-1 \leq \phi \leq 1$, $0 \leq v \leq 0.2$ (m/s), and $350 \leq T \leq 650$ K for columns 1-3 respectively. The vapor layer fails between frames 28.6 and 28.7s.

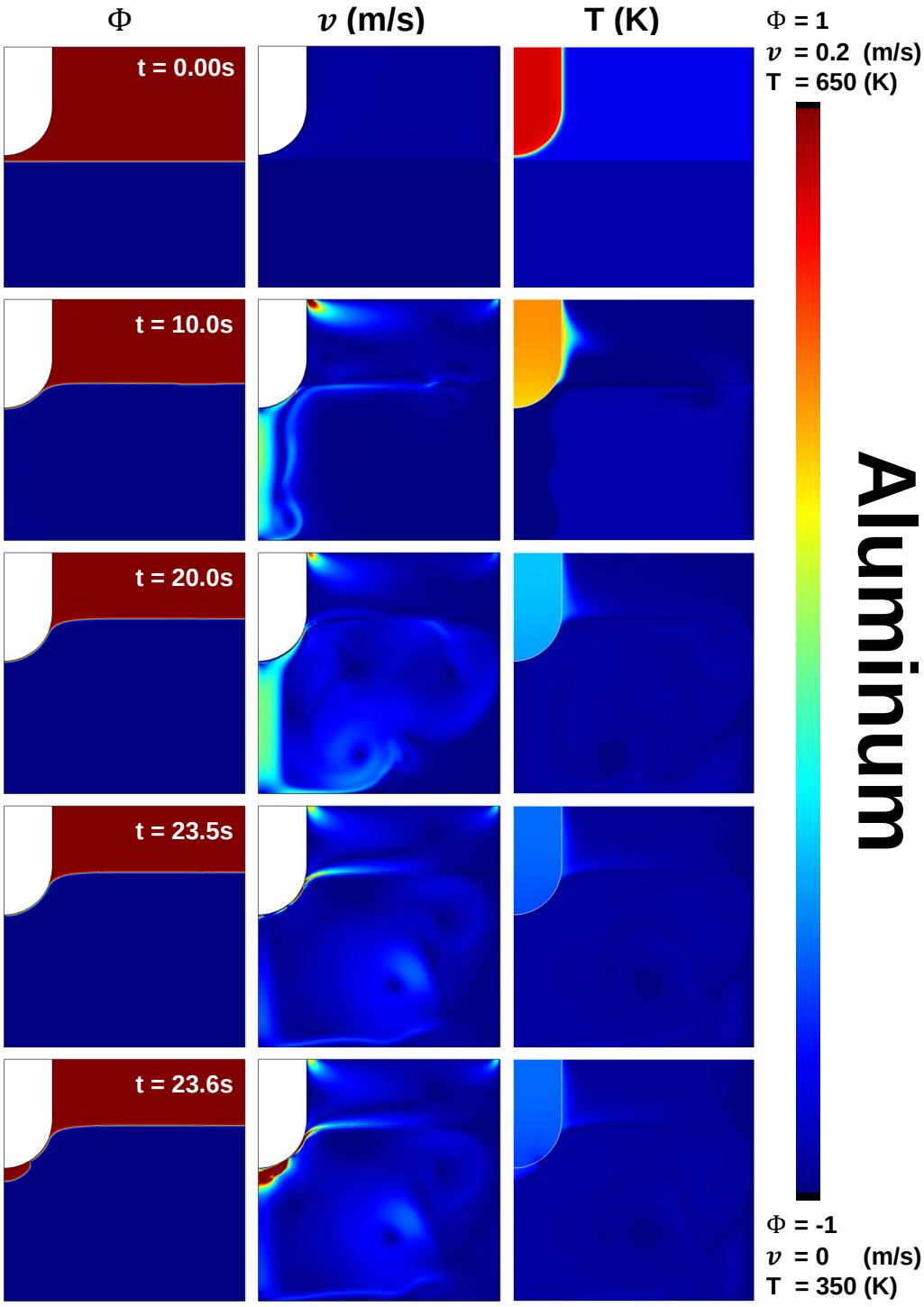

Figure 3.5: A time series of an $R = 8$ mm Aluminum object from top to bottom. From left to right is a phase field, velocity, and temperature field at the same time. The color map is $-1 \leq \phi \leq 1$, $0 \leq v \leq 0.2$ (m/s), and $350 \leq T \leq 650$ K for columns 1-3 respectively. The vapor layer fails between frames 23.5 and 23.6s.

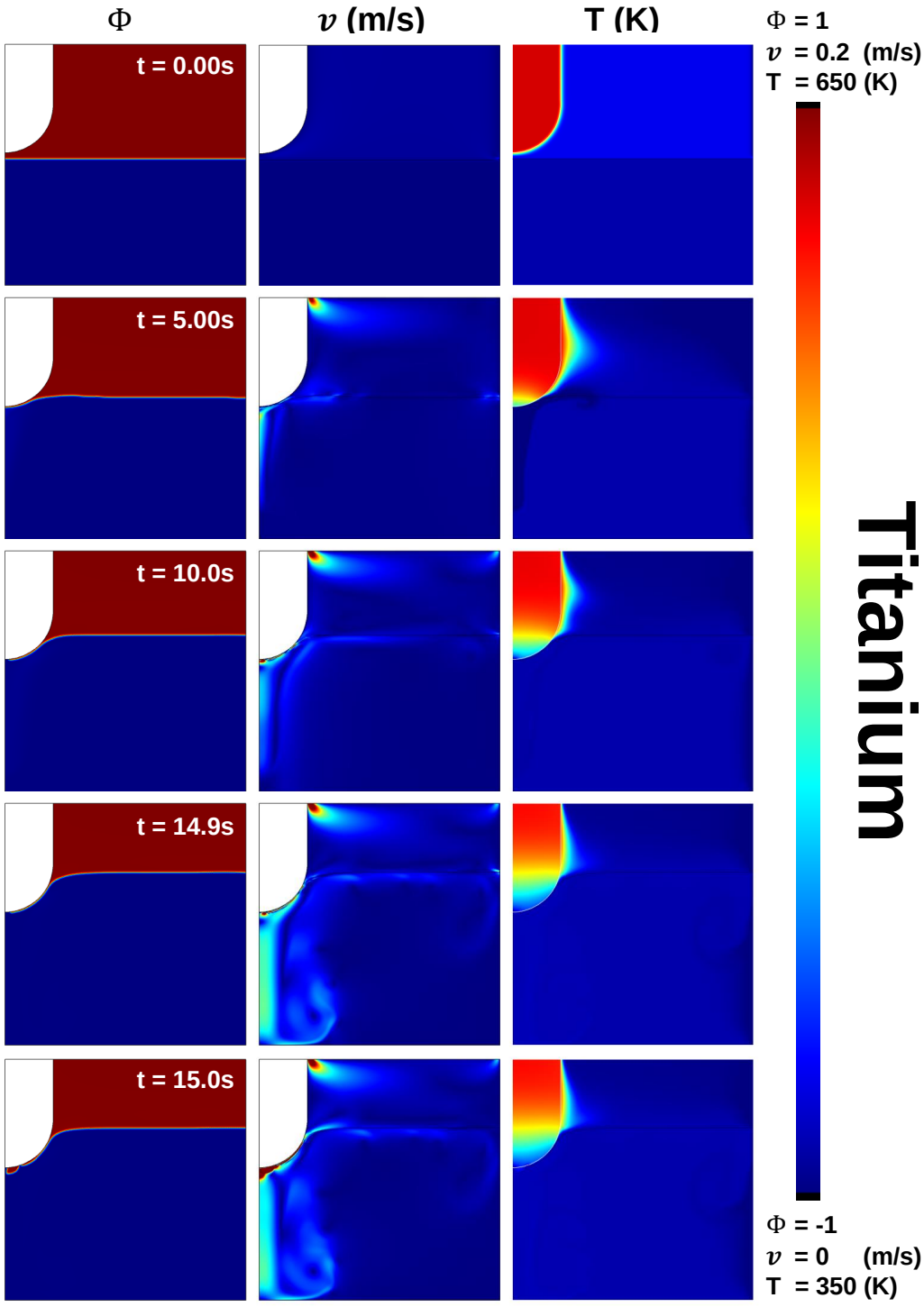

Figure 3.6: A time series of an $R = 8$ mm Titanium object from top to bottom. From left to right is a phase field, velocity, and temperature field at the same time. The color map is $-1 \leq \phi \leq 1$, $0 \leq v \leq 0.2$ (m/s), and $350 \leq T \leq 650$ K for columns 1-3 respectively. The vapor layer fails between frames 14.9 and 15.0s.

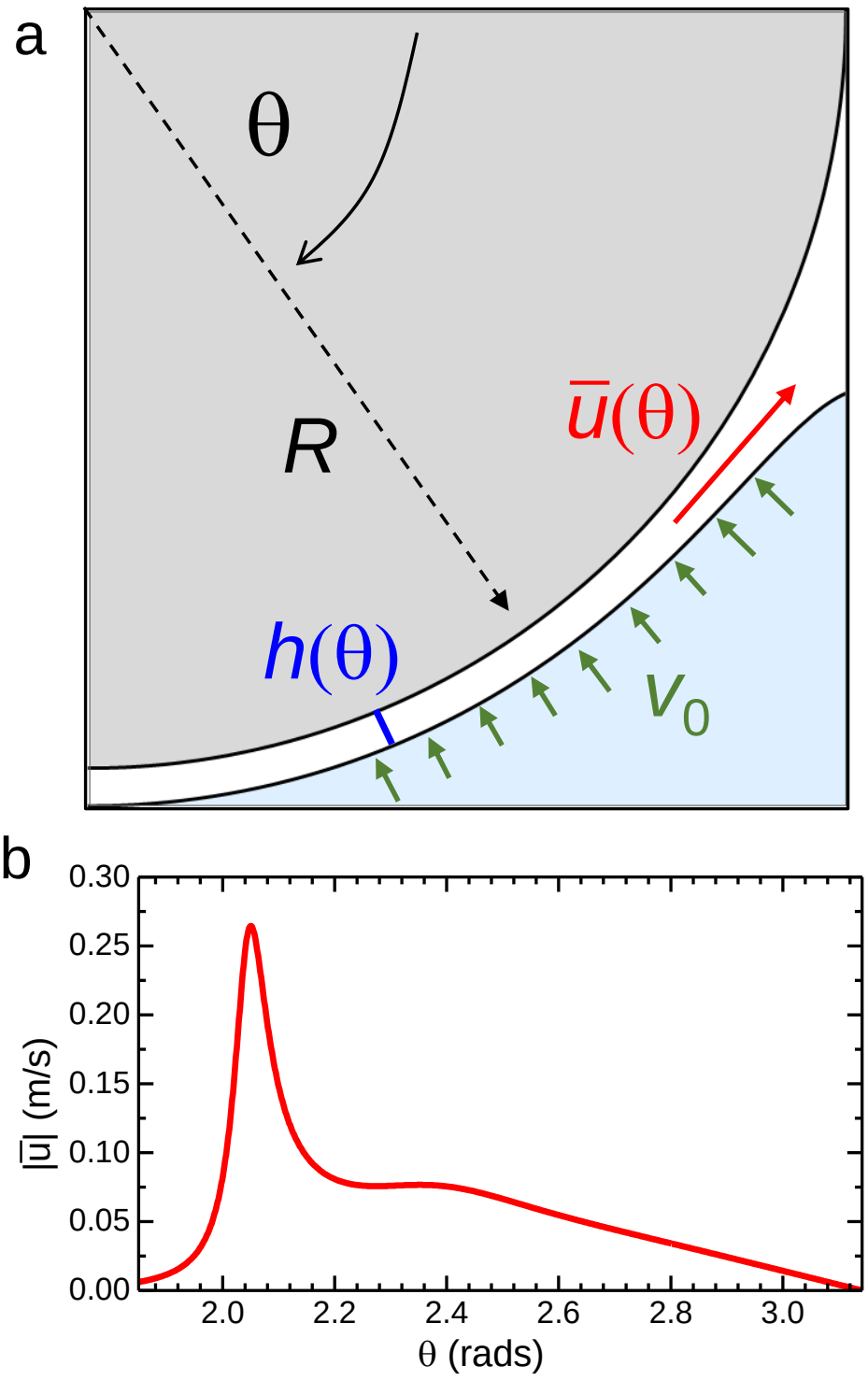

Figure 3.7: (a) Schematic of the geometry used in the lubricating flow. The local thin film thickness is $h(\theta)$, and the depth-averaged velocity is $\bar{u}$. The layer is fed by a uniform gas flow from the liquid-vapor surface with velocity $v_0 \ll \bar{u}$. (b) Solution of Eqs. 3.8 and 3.9 for $\bar{u}$ with $v_0 = 0.001$ m/s assuming a water-vapor interface at the boiling point. The corresponding solution for h is shown in Fig. 4c in the main text. The boundary conditions are $h(\pi) = 40.32$ μm, $h'(\pi) = 0$, and $h''(\pi) = 8.4$ μm.

vapor layer, with a conservation of mass in the flow. For the lubrication model presented here, both the fluid interface and the solid material are considered motionless. This is valid if the velocity in the fluid is considerably less than in the thin, vapor layer. We must compare the steady-state solutions of the COMSOL simulation with the lubrication model as has been done in past models of Leidenfrost vapor layers [23, 99, 6, 70, 98] and determine the breakdown of lubrication assumptions upon wave formation.

In general, a lubrication approximation makes two major assumptions to simplify the governing equations. First, $h/L << 1$, where h is the gap thickness and L is the total fluid path length. In a Leidenfrost system $10 \leq h \leq 100$ μm and $L \lessapprox 2$ cm making the assumption valid. Second, the fluid has a parabolic velocity profile along y such that $\vec{u}(x, y, t) = y*(h-y)$ for a given x position in time, **Fig. 3.8 a**. These two assumptions together mean an average integrated velocity can be computed along y, reducing the dimensions of the problem. Thus, $\vec{u}(x, y, t)$, can be expressed as a function of x and t, $\bar{u}(x, t)$ [66]. A separate assumption that further simplifies previous Leidenfrost simulations is to study steady-state solutions that are time independent, reducing the velocity to $\bar{u}(x)$. Upon failure of a vapor layer these assumptions break down. The wavelength and amplitude of the instability, which causes vapor layer failure, grow in time to be of order h, **Fig. 3.8 b**. The wavelength becomes the important fluid flow lengthscale, L, thus breaking the assumption that $h/L << 1$. Finally, this occurs over some finite time making the system time dependent. However, our simulations at steady-state times, where no wave instabilities occur, should obey the lubrication approximation.

The Reynolds number, Re, in the vapor layer is assumed small enough that inertia can be safely ignored when viewing a stable state. Estimates for the flow beneath centimeter-scale droplets suggest that Re $\lesssim 0.3$ [74], so this assumption is reasonable for our simple lubrication model. Since we are not explicitly considering evaporation,

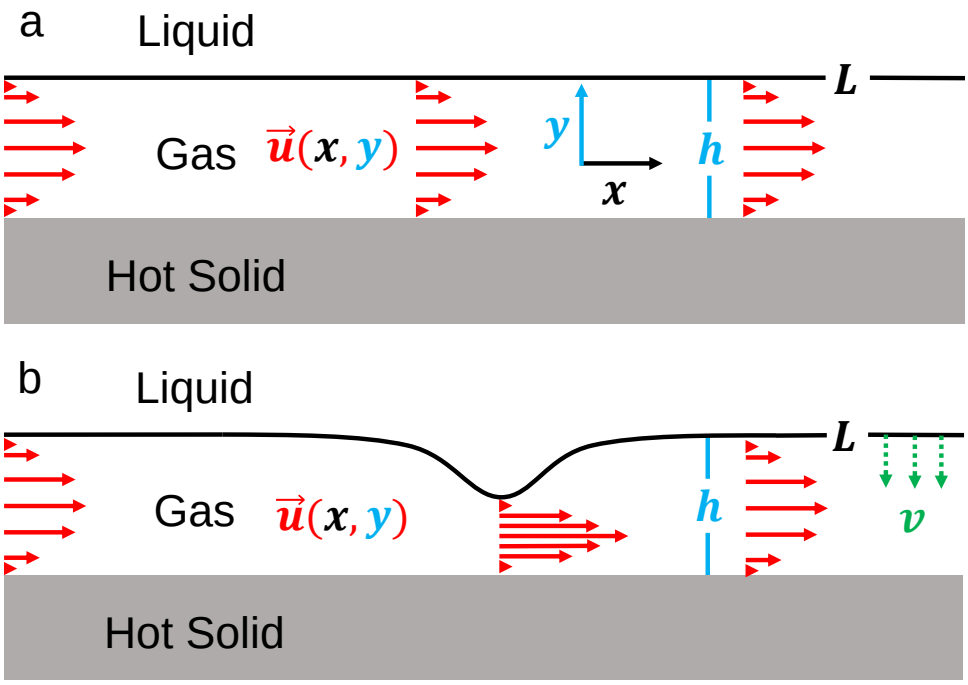

Figure 3.8: a) Depicts a time independent 2D lubrication approximation of gas flow between a hot solid and a fluid. In this system $h/L << 1$ and a parabolic profile assumptions allows the velocity to be integrated over y, simplifying $\vec{u}(x,y)$ to $\bar{u}(x)$. Here h is the thickness of the vapor layer along x and L is the characteristic length scale in the direction of fluid flow. b) Upon vapor layer failure a wave forms where now you must consider the flow between the wavepeak and the solid. The wavelength, which becomes the characteristic length scale L for fluid between the peal and the solid, is comparable to h so $h/L << 1$ is not true.

we assume that there is a constant flow of gas that feeds the vapor layer at velocity v_0. We only consider the flow around the lower part of a hemisphere immersed in a liquid, and use axisymmetric spherical coordinates so that the tip of the hemisphere (with radius R) corresponds to $\theta = \pi$ **(Fig. 3.2a)**. Both the film thickness, $h(\theta)$, and the depth-averaged velocity, $\bar{u}(\theta)$, vary with the angular coordinate. We will assume that $h \ll R$, and that $h' \ll R$, where prime denotes differentiation with respect to θ. This means that the film is thin and that its thickness varies slowly along the edge of the hemisphere, an assumption that must break down when waves form at the interface.

With these assumptions, there are two differential equations that describe the steady state profiles of h and $\bar{u}(\theta)$:

$$h\bar{u}\sin\theta = -Rv_0(1+\cos\theta), \tag{3.8}$$

$$12\eta\frac{\bar{u}}{h^2} = \frac{1}{R}\frac{d}{d\theta}\Big[\rho_l g(R+h)\cos\theta + \gamma\kappa\Big]. \tag{3.9}$$

Equation 3.8 comes from mass conservation of the gas in the vapor layer, assuming that $\bar{u}(\pi) = 0$ from symmetry considerations. The mass continuity in the vapor layer at θ results from the integrated amount of gas entering the vapor layer, starting from $\theta = \pi$. **Equation 3.9** balances the pressure gradient necessary to drive the flow $\bar{u}$ in the lubricating vapor layer with the pressure gradient determined by hydrostatic (gravitational) forces and variations in the Laplace pressure. The variable $\kappa = \kappa(\theta)$ is the total curvature of the interface, and can be calculated by taking the divergence of the normal vector to the liquid-vapor interface:

$$\kappa = \vec{\nabla}\cdot\hat{\mathbf{n}}, \tag{3.10}$$

$$\hat{\mathbf{n}} = \left(-\hat{\mathbf{r}} + \frac{h'}{R+h}\hat{\boldsymbol{\theta}}\right)\left(1+\frac{h'^2}{(R+h)^2}\right)^{-1/2}, \tag{3.11}$$

where the spherical coordinate r is evaluated at $R+h$ after differentiation. Here we

have kept the full curvature with no approximations in order to correctly model the shape of the interface all the way to the boundary.

Equation 3.8 can be solved directly for $\bar{u}$ and inserted into **Eq. 3.9**, resulting in a third-order differential equation for $h(\theta)$. For a given gas input velocity (v_0), we choose initial values of $h(\pi)$ and $h''(\pi)$ since $h'(\pi) = 0$ by axisymmetry. We then solve the resulting equation for $h(\theta)$ until we match the conditions at the boundary (i.e., $x = 5$ mm in **Fig. 3.9a**). We match the height of the liquid level at the boundary, and require that $h' = (R + h)\cot\theta$, which corresponds to the requirement that the normal of the interface points in the z direction. Using the properties for water and steam at the boiling point ($\rho_l = 959$ kg/m^3, $\gamma = 59$ mN/m, $\eta = 1.3 \times 10^{-5}$ Pa·s), and using $v_0 = 0.001$ m/s, we illustrate a steady solution where $h(\pi) = 40.32$ μm in **Fig. 3.9a & b**. In the COMSOL Model, a higher viscosity ($\eta = 1.3 \times 10^{-5}$ Pa·s) is used in the gas to reduce the computational costs of the two-phase interface. Decreasing the change in viscosity over the gas and liquid phases allows for a thinner interface while yielding the same results in COMSOL. However, using the higher gas viscosity in the lubrication approximation resulted in thicker vapor layers. The corresponding velocity of the lubrication approximation, $\bar{u}$, is shown in **Fig. 3.7b**. The peak at $|\bar{u}| \approx 0.25$ m/s corresponds to the minimum in h, and agrees very well with the velocity from the full COMSOL simulation **(Fig. 3.12a)**.

There are a few things to note about the solutions. First, the solution is technically not valid when $h \sim R$. For boundaries which are not too far from the solid edge at R, this is acceptable [70], but for far-field boundaries the solution would need to be matched to an outer solution for the liquid-vapor interface. Second, these are steady solutions, so there are no dynamics. This means that for a given v_0 and set of boundary conditions, a solution may not exist. In fact, the structure of the branches where solutions exist is quite complicated, as may be expected from similar problems considering the lubricating flow under droplets [70, 30]. In reality, a vapor

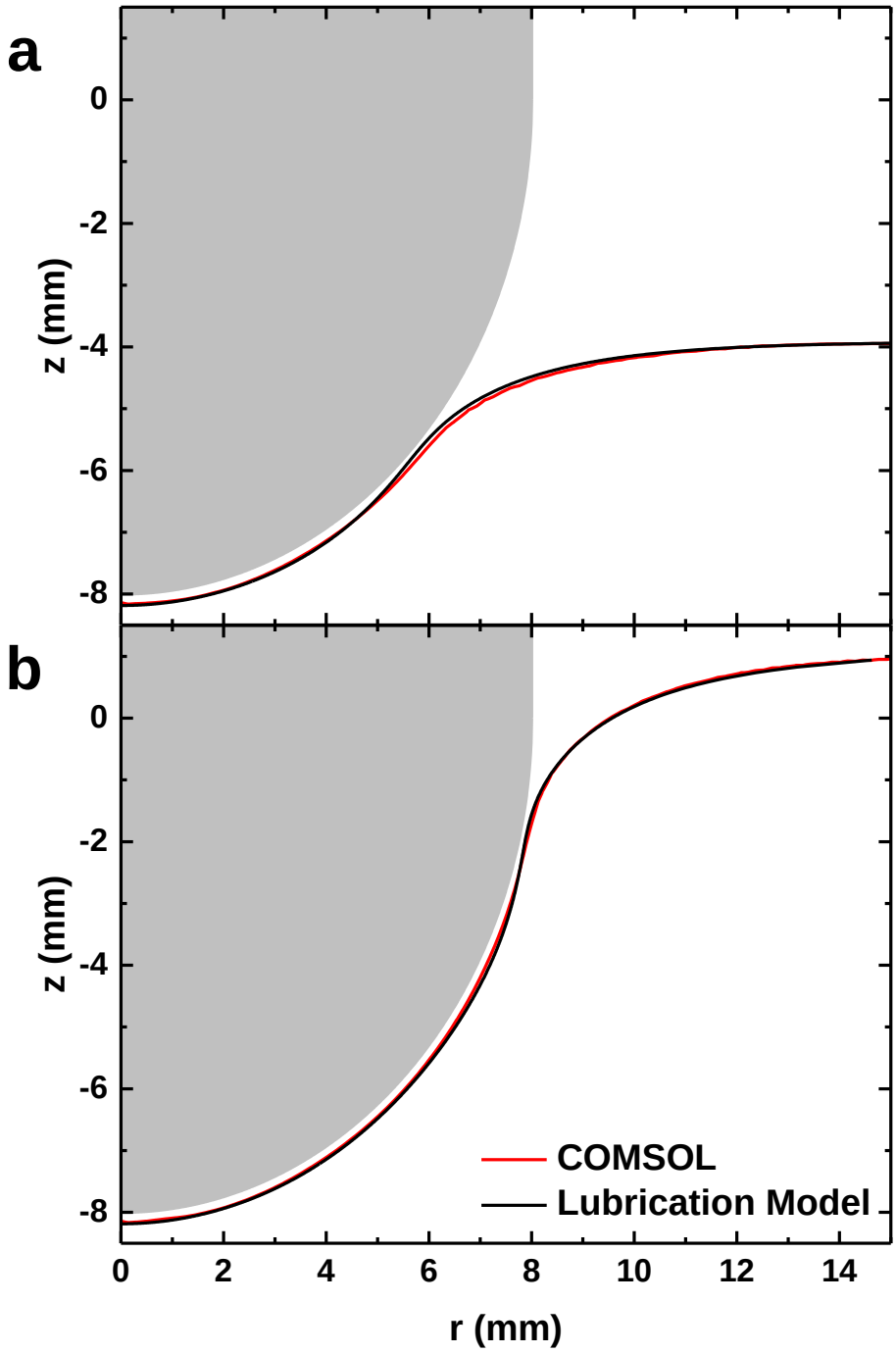

Figure 3.9: Comparison between the COMSOL rendered interface, red, and the Lubrication modeled interface, black, at a steady-state moment. Both use the values of water and water vapor: $\rho_l = 1000$ kg/m^3, $\gamma = 0.0588$ N/m, and $R = 8$ mm. One parameter difference is that the lubrication model uses the real dynamic viscosity, $\eta_l = 1.3e-5$ Pa·s, where the COMSOL simulation used $\eta_l = 1.3e-4$ Pa·s to reduce the computational costs of the phase field interface.

layer may exist for a given thickness and boundary conditions in the experiments, but it will fluctuate in time. Periods of quiescent behavior in the experiment and COMSOL simulation correspond to regimes where steady solutions of the lubricating vapor layer exist.

3.4 Chapter conclusions

We simulated Leidenfrost vapor layers around fixed hot solids using two-phase laminar flow with heat transfer and evaporation. We varied the geometry of the vapor layer and the thermal properties of the hot solid to expand upon our previous experimental results [42]. In experiments, we found the minimum Leidenfrost Temperature, $T_{-} = 140°\text{C}$, was independent of solid thermal properties, geometry, and salt concentration of the fluid. However, the explored geometric domain was limited due to experimental constraints. Here, simulations replicate experimental results, expand the geometric domain, and give insight into the instability that drives vapor layer failure.

The vapor layer geometry is varied with two parameters, the radius of the hot solid $2 \leq R \leq 16$ mm and the water height, $0.5 \leq H \leq 17$ mm. A geometric space with effective area, $0.02 < A_{eff} < 12$ is achieved. Where $A_{eff} = A_v/A_{lc}$, $A_v = 2\pi aR$ is the semi-spherical surface area of the vapor layer found by integrating [11]:

$$\int_0^{2\pi} \int_0^{\cos^{-1}\frac{R-a}{R}} R^2 \sin\theta d\theta d\Phi,$$

where a is the height measured at the inflection point of the $\phi = 0$ contour (see **Fig. 3.10**), and we use $A_{lc} = 2\pi lc^2$ to normalize the area, where $lc = 2.5$ mm (capillary length of boiling water). Additionally, we test the effect of solid thermal properties by using real material values described in **Table 3.3**.

A simulation proceeds as described in **Section 3.2** until vapor layer failure. As the water level rises, evaporation forms a vapor layer of order 100 μm around the hot

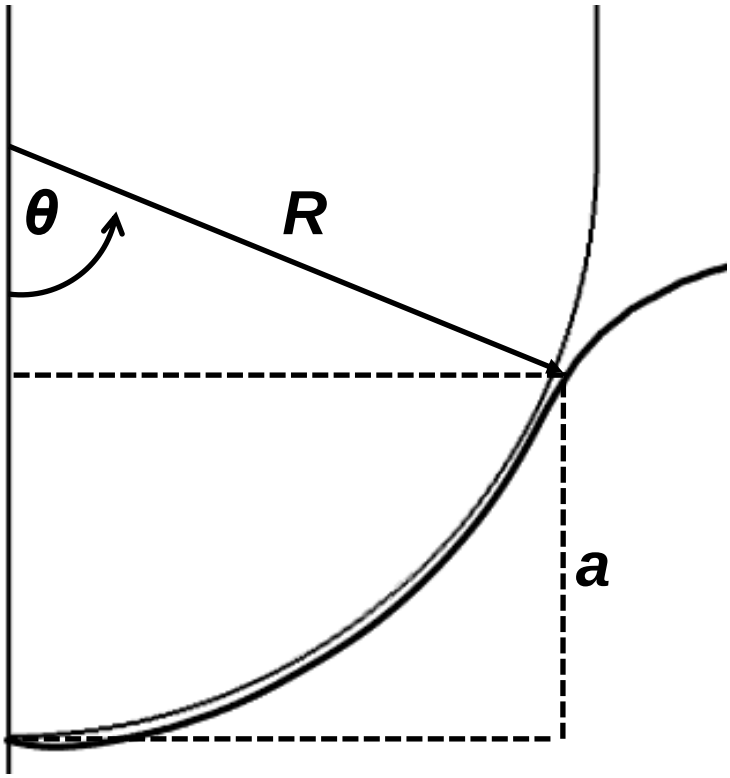

Figure 3.10: The effective surface area is defined as the surface integral of the hemisphere to the inflection point of the vapor layer interface defined as a.

object. Local cooling of both the solid and the fluid in proximity to the evaporated gas, determined by Q_s, is initially strong enough to create a downward convection flow **Figs. 3.4 - 3.6**. This is most easily observed in simulations where the metal has a low thermal conductivity like titanium, **Table 3.3 & Fig. 3.6**. However, as the solid cools down, super cooling convection is minimized and the water near the interface is heated. This produced the upward convection near the interface that we expect before failure.

Upon solid cooling, the heat transfer rate decreases, convection slows, and the vapor layer thins, **Figs. 3.4 - 3.6**. Eventually the balance of evaporation, pressure, and velocity gives way to an instability. In experiments, the instability is seen as surface waves, **Fig. 3.1a**, which cause the explosive collapse of the vapor layer. In simulations, the instability appears as the same interfacial wave, sometimes many waves, which grow and move along the surface until fluid-solid contact (last frames of **Figs. 3.4 - 3.6**). This is most clearly illustrated in **Fig. 3.12b** with waves of wavelength $\lambda \approx lc = 2.45$ mm, the capillary length of water at boiling. At liquid-solid contact, T_s is still well above the boiling point of water, so rapid evaporation ensues. At that point, the COMSOL simulation often crashed due to the explosive nature of the fluid dynamics. However, we can analyze the results of the simulation leading to failure.

In chapter 2, we could precisely determine the failure of the vapor layer in time as a discontinuity in the thickness measurement. That discontinuity correlates to the wetting of the surface as liquid comes into contact with the hot solid. To directly compare simulations to experiments we want to similarly define vapor layer failure at the initial contact point between the fluid and solid. Therefore, T_- is taken in the solid at the contact point of a wave peak one time-step before collapse. In **Fig. 3.11a** we plot T_- as a function of A_{eff} for for hot objects of $R = 2$, 4, 8, or 16 mm (circle, right facing triangle, square, and left facing triangle) and different thermal properties

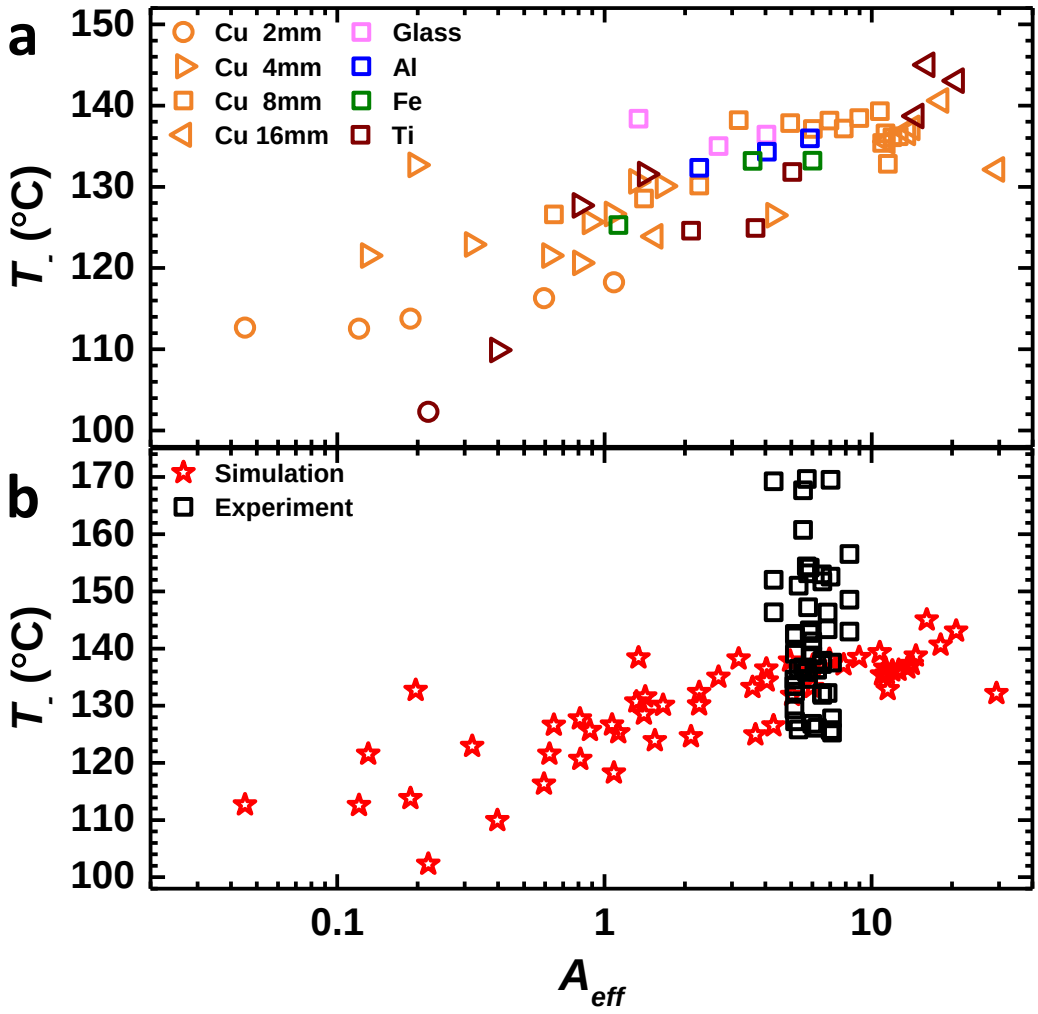

Figure 3.11: a) Local failure Temperature, T_{-}, of vapor layer collapse for simulations of various materials, denoted by color, and hot object radii from 2-16 mm, denoted by symbols plotted vs the normalized surface area, A_{eff} of the vapor layer. In general, T_{-} decreases with A_{eff}, but there are large fluctuations at small surface area. b) Comparison of T_{-} from simulation with experiments [42]. Simulations act as a lower bound for expected experimental results.

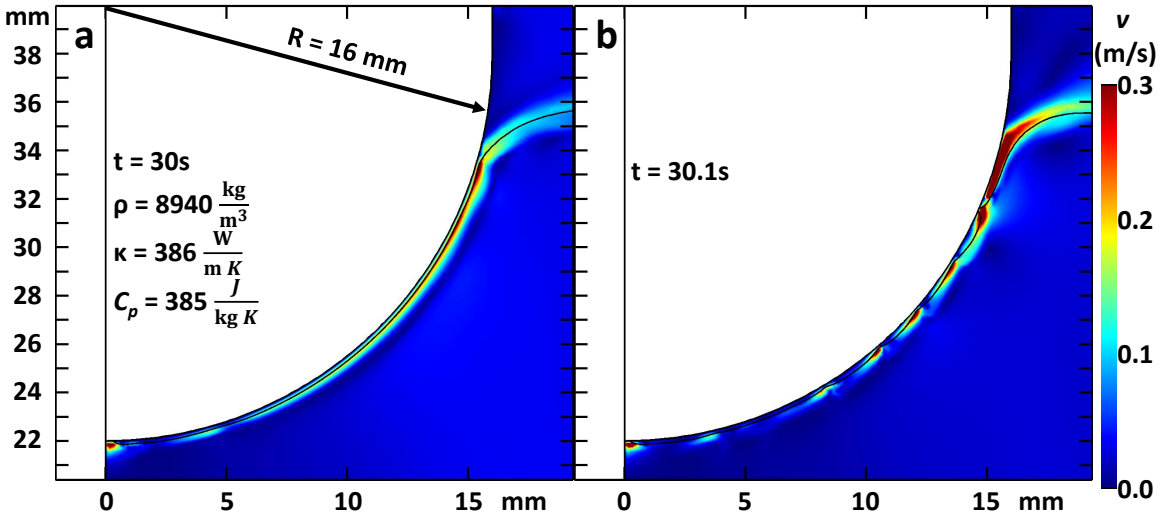

Figure 3.12: Velocity field of the fluid at 30 s (a) and 30.1 s (b). Surface waves of $\lambda = 2.45$ mm grow between the two frames and collapse occurs at the apex of the wave furthest to the right in panel b.

(colors).

Just like in experiments, we find that T_- is independent of the thermal properties used and overall T_- plateaus as A_{eff} increases. Above this surface area range we would approach significant computational costs and a size range that correlated to the break up of droplets [90]. Interestingly, when $A_{eff} < 1$ we approach a size regime that requires perturbations smaller than lc to initiate failure. Wavelengths smaller than lc are energetically very expensive and cannot be produced in the system. Therefore, in the small area limit, a perturbation driven collapse is no longer valid. Instead, the vapor layer fails when the hot solid can no longer evaporate fluid. In this regime, T_- decreases significantly and can even approach boiling [42, 121]. These results match those of our experiments where we saw no correlation between thermal conductivity and T_-, **Fig. 3.2b**. Furthermore, when directly comparing T_- of simulations and experiments it appears the simulations act as a lower bound for experimental T_-. In experiments, uncontrollable factors such as debris in the tank, wave disturbances, and finite surface roughness of the hot objects can lead to premature failure at higher temperatures, **Fig. 3.11b**.

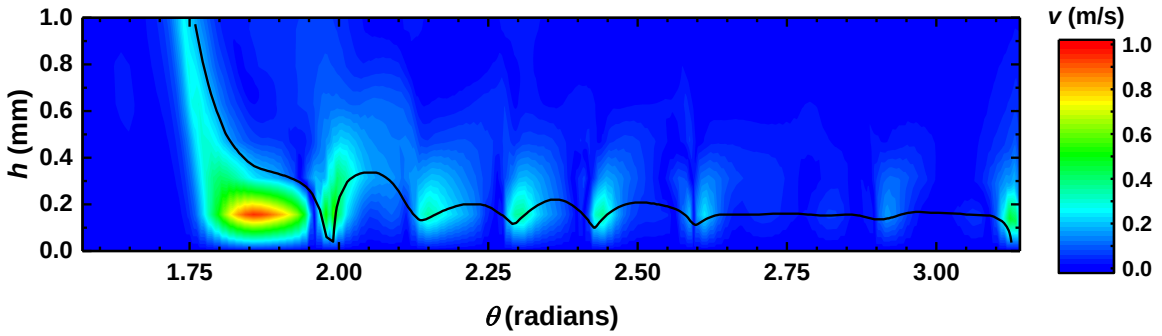

Figure 3.13: This velocity heat map clearly shows the waves at failure. Here velocity is plotted for the 16 mm hot object shown in **Fig. 3.12** along θ as defined in **Fig. 3.7** and a distance h from the surface. $\theta = \pi$ correlates to the tip of the hot object. The interface line is shown in black.

What mechanism is determining this consistent failure temperature? While the vapor layer is stable, evaporated water maintains a slowly varying velocity field at consistent thickness **Fig. 3.12a**. This matches the requirement of lubrication flows, **Fig. 3.9a & b**. However, there must come a point where a wave instability brings fluid close enough to contact the solid, breaking the lubrication approximation, **Fig. 3.12b**. Interestingly, the wavelength, λ appears to be $\sim$ 2.5 mm which is approximately the capillary length of boiling water, lc. This is more clearly visualized when plotting the velocity a distance h from the surface along θ in **Fig. 3.13**. **Figure 3.14** shows a time series of the wave instability causing failure. You can clearly see the waves appear and then grow as they move upwards around the hot solid. On the right, the velocity arrow graph clearly shows non-uniformity and a suction towards the hot object at the wave peaks.

An unstable wavelength between two fluids is reminiscent of a Kelvin-Helmholtz or Rayleigh-Taylor instability. However, in both these cases the critical wavelength is of order centimeters not millimeters. We must look elsewhere for the instability mechanism and consider all possible forces in our system that could be contributing to it. Consider the simple picture of a wave at the gas-fluid interface depicted in **Fig. 3.8b** and the forces acting on it. Surface tension and evaporation both act as

restoring forces to push the wave peak away from the solid. The surface tension wants to minimize the surface area, and thus restores any local perturbations that form. Similarly, evaporation will push a wave away from the surface since evaporation rates increase as the fluid approaches the solid. Gravity could instigate wave growth, but only for wavelengths above 1.6 cm, much larger than the millimeter sizes disturbances seen in simulation and experiment. Similarly, a lubrication pressure could create lift (suction in this case), but only in asymmetric wave peaks, which is not the case for our system. As a wave approaches the surface, the velocity of the escaping gas must increase between the wave peak and the solid, creating a low pressure zone that would further pull the fluid towards the solid via Bernoulli's principle. However, this is not expected for the initial growth of the small, symmetric disturbances we see in simulations (**Fig. 3.14**). The inertia of the fluid and gas could help explain the initial growth of the wavepeak. The pressure of the gas layer keeps fluid from approaching the solid, however as the pressure decreases the fluids momentum can overcome that pressure and allow liquid-solid contact. We currently believe that inertia is an important factor in instigating the instability, which means that the lubrication approximation, used in previous steady-state simulations, becomes invalid near instabilities in Leidenfrost vapor layers. It has been shown before that inertia can be paramount to inciting instabilities in other fluid systems namely, in Hele-Shaw systems [31] and in 2D inviscid pinch off [18].

We are currently varying parameters to quantify inertia's role in vapor layer collapse. **Figure 3.15a** shows the interfacial profiles one frame before collapse when changing the surface tension, γ. Colors denote the γ used with T_{-} for a given γ in the corresponding color. T_{-} increased with increasing γ, but the shape of the interface at failure is greatly affected. Therefore, the failure mechanism is not properly isolated when changing γ. When we vary Mw of the gas, **Fig. 3.15 b - d**, T_{-} increased with increasing Mw, but retained the same interface profile at failure. Mw is an

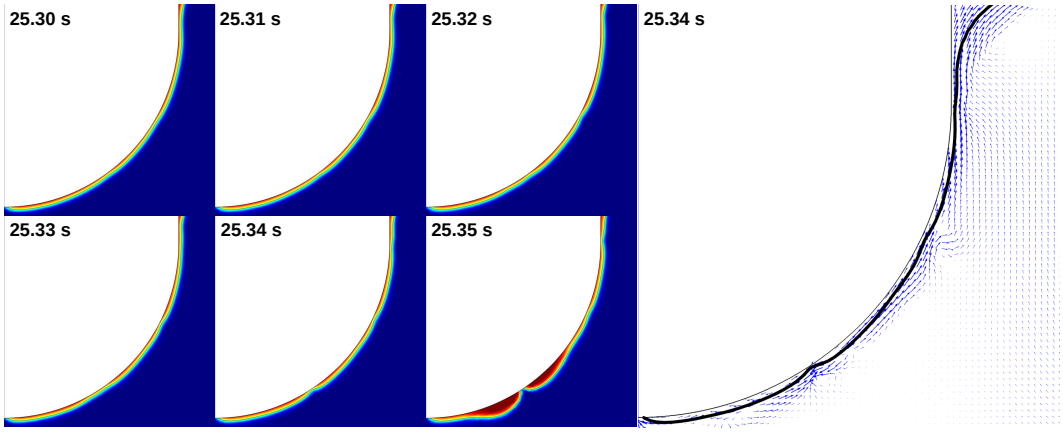

Figure 3.14: The left 6 frames show a phase field time series leading to the failure of the vapor layer. Surface waves are clearly visible and grow in time until one peak contacts the solid. On the right is an arrow velocity map showing the non-parabolic velocity gradient 1 frame before vapor layer failure.

important parameter as it defines ρ_v and L for the vapor in our simulation, **Table 3.1**. The culmination of results of altered parameters so far is shown in **Fig. 3.16**. I plot T_- vs γ (red) and T_- vs Mw (blue), where triangles denote varying Mw with L as defined in **Table 3.1**, and circles denote varying Mw while keeping $L = 2.33 \times 10^6$ J/kg constant. We see a 100°C increase in T_- when γ is increased by a factor of 10 and a similar increase when varying Mw from 0.009 to 0.072 kg/mol (blue), where the value for water is 0.018 kg/mol, **Fig. 3.16**.

Keeping L constant isolates ρ_v as the altered parameter and gives us same basic result as simulations where L is a function of Mw. This confirms that L, which determines the rate of evaporation, Q_s, does not significantly affect T_-. It is in fact ρ_v, which seems to determine T_- in our simulations. The density of the gas affects mass and thus the inertia. Our current hypothesis is that some perturbation at the interface causes a wave to form. That wave brings fluid close to the hot solid. Above the failure temperature, the restoring forces due to evaporation and surface tension are enough to push waves in the fluid away from the hot solid. However, at the critical temperature, T_-, if a wave forms at the surface, inertia of the fluid overcomes the restoring forces and initiates liquid-solid contact. If inertia was not playing a role

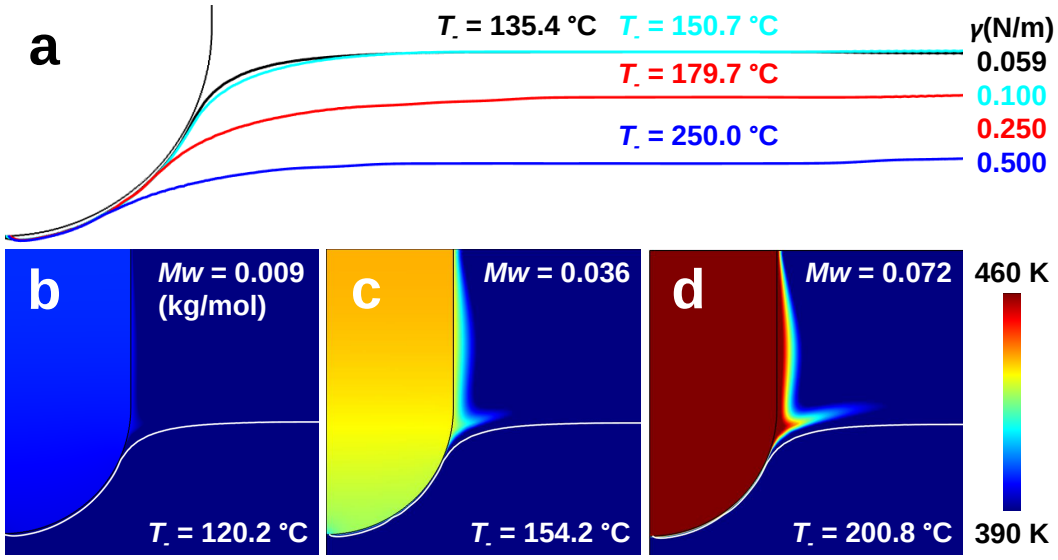

Figure 3.15: (a) Interface profiles for the frame before failure for various γ values listed. Increasing γ significantly changed the profiles and increased the temperatures at failure, T_{-}. (b - c) Temperature heat maps for the frame before failure when increasing the molecular weight of the gas, Mw. The failure temperature increases significantly while maintaining the same interface profile.

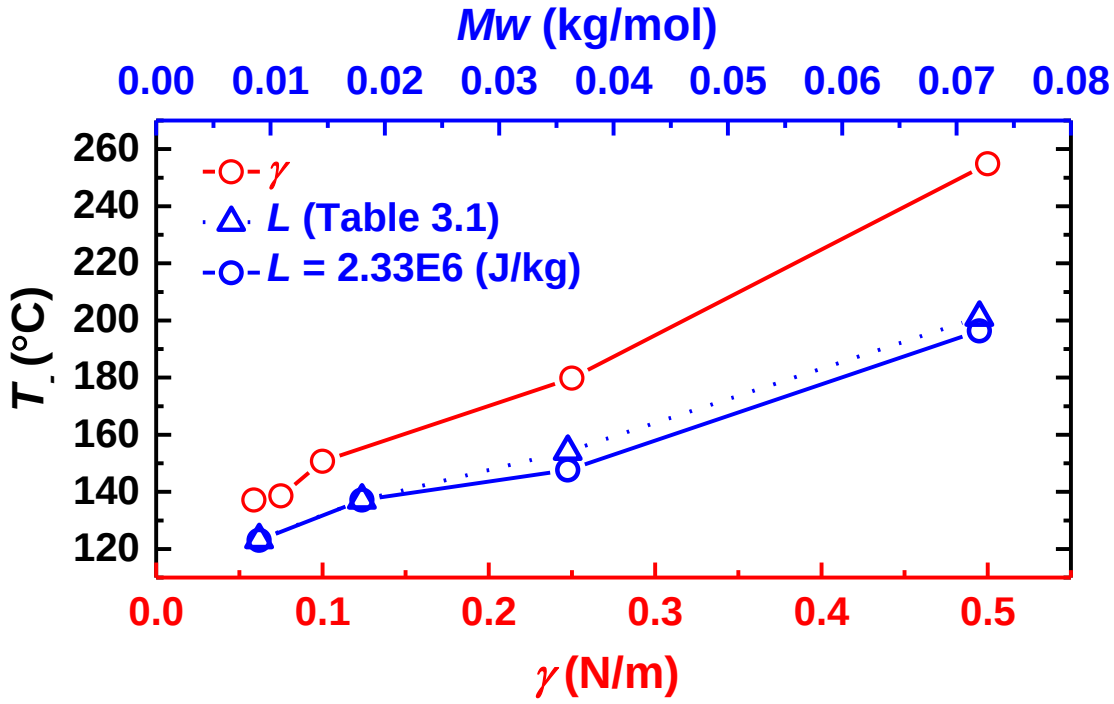

Figure 3.16: Simulations where either the surface tension coefficient, γ (red), or the molecular weight of the water, Mw (blue), were varied. Mw is used to define ρ_v of the simulations.

then we should not expect ρ_v or any other fluid property to significantly alter T_{-}. We continue to test parameters that may affect the failure temperature to isolate the failure instability.

Chapter 4

The lifetime of charged dust in the atmosphere

In this chapter I will explain the experiments performed to investigate charge decay on a variety of acoustically leviated particles under various atmospheric conditions. The text in this chapter has been adapted from recently accepted work of the same title, currently available on the arXiv [39]. In nature, dust and other air borne particles impact various systems, the lifetime of these particles in the atmosphere is not well understood. Observations repeatedly find large dust grains thousands of kilometers away their sources, in contrast to previous predictions. Since dust can charge during lofting, electrostatic forces may explain long residence times of coarse particles. However, the temporal stability of electrostatic charge on dust is unknown. We bridge this knowledge gap by monitoring the charge decay on acoustically-levitated electrified dust particles in various environments. We show that charge decay is primarily driven by ion recruitment to the particle surface through the electric potential. The model we develop is driven by diffusion which occurs on a lengthscale much larger than the particle diameter. Therefore, while we are limited to studying particles with diameters 0.1-2 mm, the ion capture model can be applied to all particles smaller than

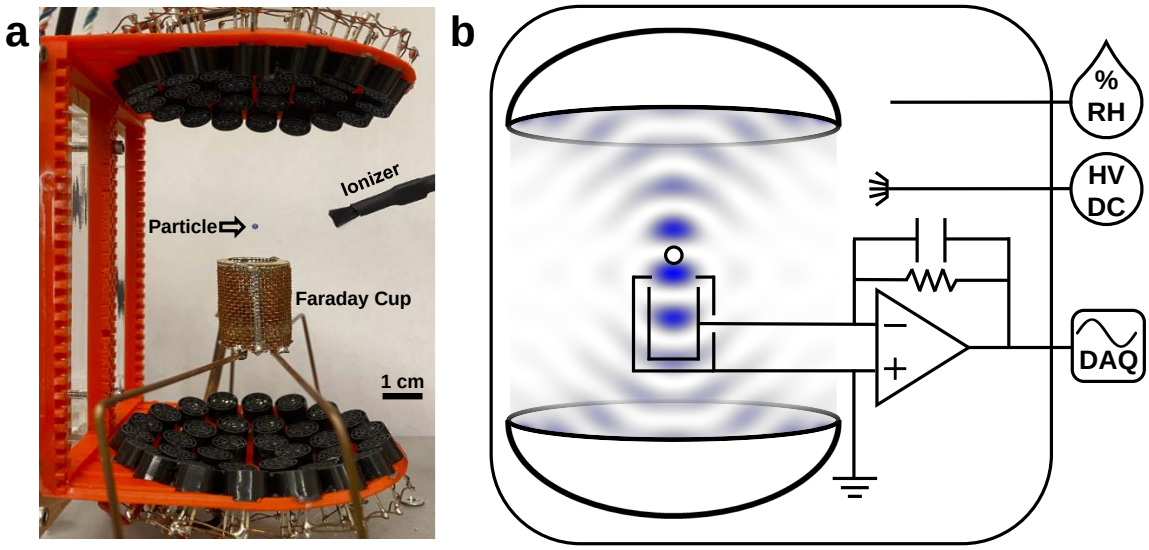

Figure 4.1: (a) A TinyLev acoustic levitator suspends a 2 mm polystyrene bead above the acoustically-transparent Faraday cup. (b) Diagram of the charge measurement system inside the environmental chamber with a theoretical acoustic field.

a few centimeters in diameter. Particles remain charged for days or weeks, suggesting that electrostatic forces may be important for the transport of dust with diameters of order 10 μm.

4.1 Non-contact charge measurement technique

We measured the decay of surface charge on single particles lofted in air using a TinyLev Acoustic Levitator (TAL) [77] housed in a environmental chamber. TAL is an open-source, 3D-printed design presented in Marzo *et al.* [77]. TAL consists of two semi-spherical arrays of 40 kHz transducers separated by a distance 11.5 cm. Generally, both hemispheres are driven in phase, creating a standing wave which can hold a particle static. However, by slightly changing the phase of one hemisphere, a particle in the acoustic trap may be moved up or down. We utilize this technique to lower and raise micron- to millimeter-sized particles in a non-contact manner, **Fig. 4.1 a** & **b**.

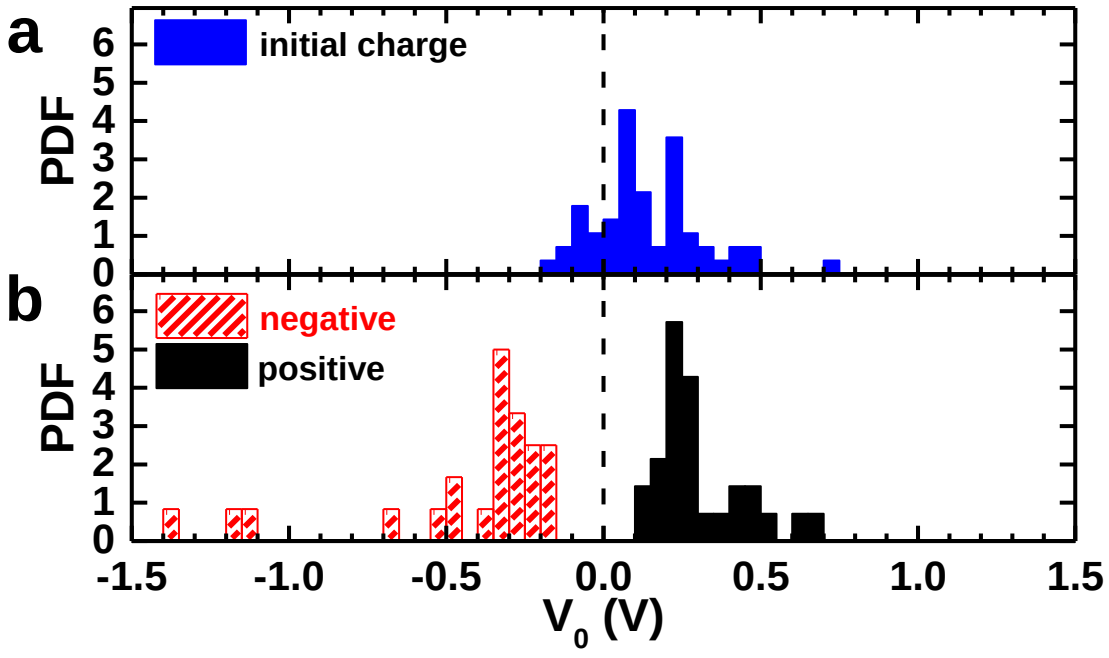

Figure 4.2: (a) Probability density function of charge on EPS particles before ionization. Particles have some initial positive charge after being extracted from container. (b) Distribution of charge on particles immediately after ionization with negative or positive bias.

We modified TAL with the ability to measure charge on suspended particles with a resolution of 1 fC ($\approx$ 6250 elementary charges). Particles placed in the acoustic trap are initially charged by ionizing the air in the chamber with a Bertan Series 225 high-voltage power supply at $\pm$ 8-10 kV connected to a bundle of sharp carbon needles for 10s. This eliminates any initial charge bias (**Fig. 4.2a** and **Fig. 4.3**). Free ions and electrons rapidly adhere to all surfaces including the isolated particle. Using a Gerdien tube condenser ion counter (AlphaLab, Inc), we estimate the ion density at the location of the levitating particle to be 10-15 $\times$ 10^6 cm^{-3} during the charging period. Since the ion concentration rapidly decays a few seconds after the ionizer is shut off, presumably due to collisions with grounded metallic surfaces in the apparatus, we allow a 5 min wait period before measurements. Once charged, a particle's surface only discharges across the gas-solid boundary.

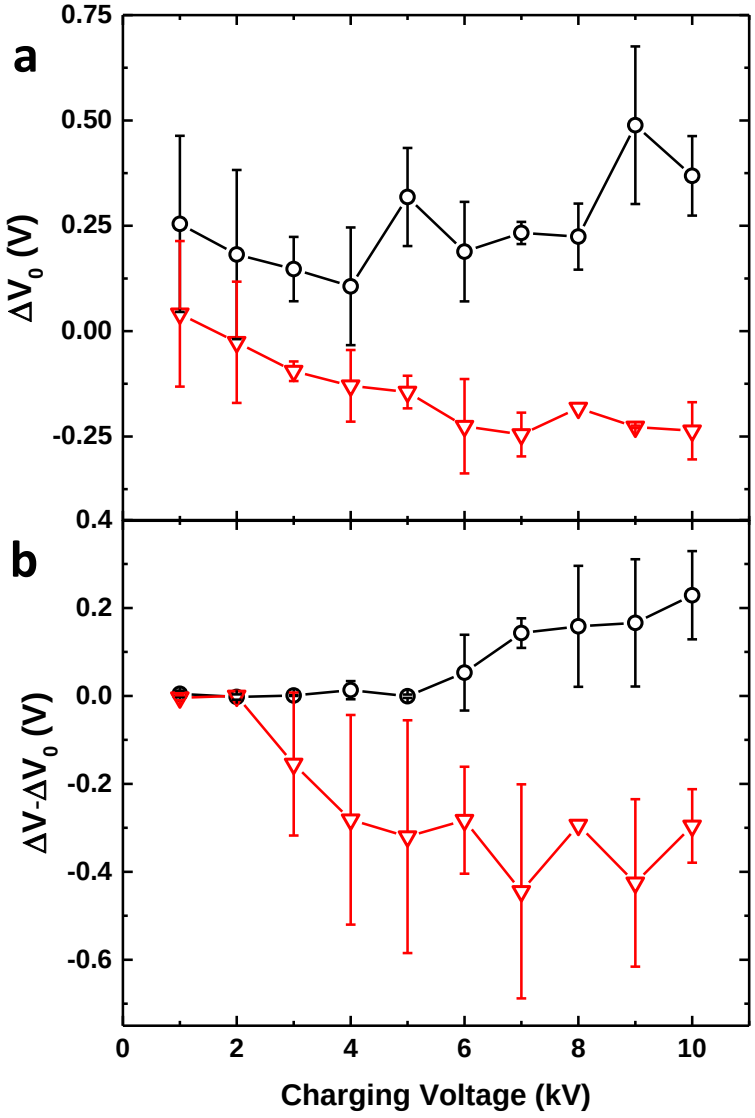

Figure 4.3: (a) Average voltage obtained by a particle after charging with the corona ionizer at a given voltage (x-axis). Most particles have a natural positive charge before the experiment **Fig. 4.2** . (b) Average voltage difference between the final and initial state of a particle after charging with the corona ionizer. Charging mostly saturates after 7 kV. Our experiments use 8-10 kV to eliminate any initial bias.

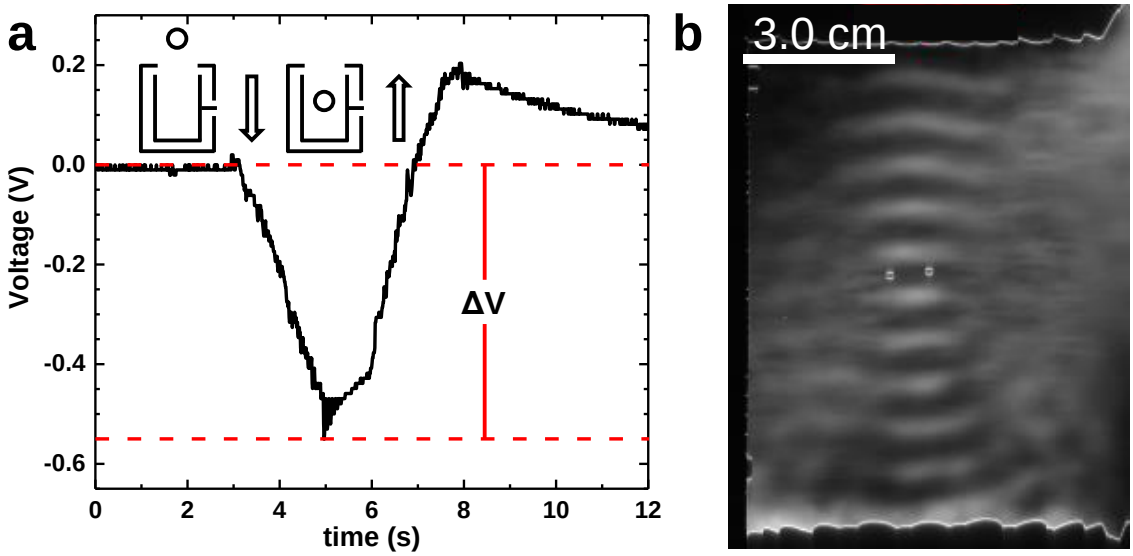

Figure 4.4: (a) Output of the amplification stage as the particle was lowered into and raised out of the Faraday cup. ΔV that corresponds to the charge on the particle.(b) Schlieren image of the acoustic field with a single levitated particle [95, 27]. A second, virtual image of the particle is visible in the mirror.

TAL can hold a trapped particle static and move it along its primary axis (**Fig. 4.4b**. We use this capability to perform non-contact charge measurements across extended time frames: a levitating particle is periodically (every 1-5 min) lowered by 2λ into and raised out of an "acoustically transparent" Faraday cup (ATFC) to ascertain its surface charge. The ATFC is connected to charge-sensitive electrometer which provides an overall sensitivity of 1 pC/V. A typical signal from the output stage of the electrometer during one measurement cycle is shown in **Fig. 4.4a**. The voltage difference ΔV between the initial baseline and the curve's minimum is proportional to the amount of charge on a particle's surface:

$$\Delta V = -100 \times \frac{Q}{C} e^{-t/RC}. \tag{4.1}$$

Here, the time constant of the charge amplifier's feedback loop was $RC = 5$ s, where $C = 1$ nF and $R = 5$ GΩ. Because the particle never touches a surface during the measurement process, charge loss occurs only through interactions with the gas.

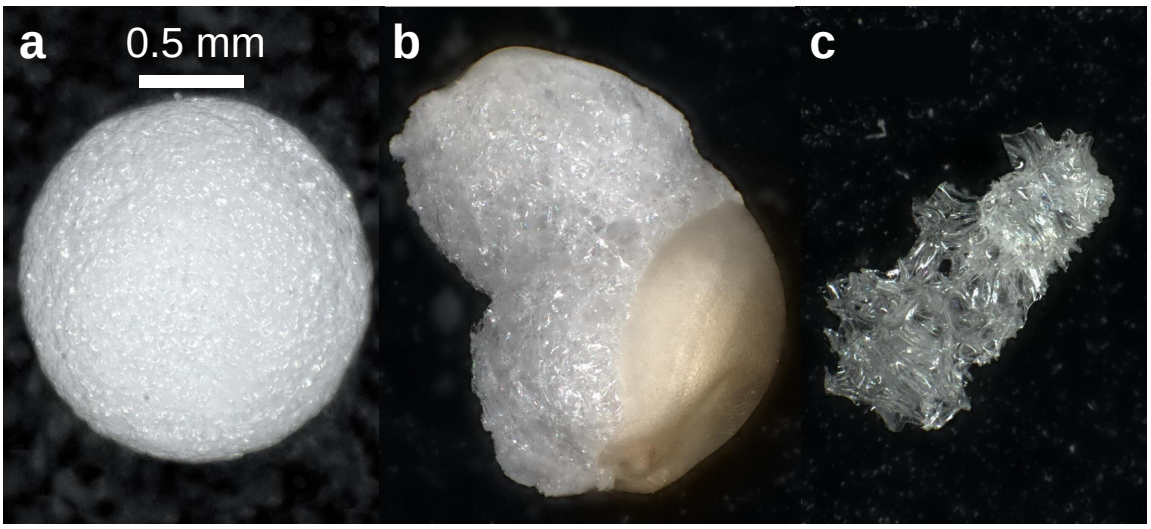

Figure 4.5: (a) Expanded polystyrene bead (EPS). (b) Toasted amaranth grain. (c) Pumice from the 1932 eruption of the Quizapú volcano (Maule, Chile).

To approximate the diversity of particles suspended in Earth's atmosphere (from silicate dust to pollen to microplastics), we explored the decay of charge on particles of 4 compositions: expanded polystyrene (EPS), silicon aerogel, toasted amaranth (Peru), and volcanic pumice (Quizapú, Popocatépetl, and Kos). Exemplary grains are rendered photographically in **Fig. 4.5 a - c**. All particles, despite a wide variation in shape, had spherical-equivalent diameters (SED) ranging between 1-2 mm, where SED is an approximate measure of largest distance between 2 points on the surface of the particle. Although TAL can suspend particles with densities as high as 3,000 kg/m^3, the device has difficultly moving such dense materials up and down as required for our charge measurement. Therefore, we did not conduct experiments with solid silica sand. Nonetheless, both the pumices and the aerogel have high silica contents (68%- 75% [97, 93] and 100%, respectively), making them first-order analogs for silicate particles. Furthermore, as will be discussed later on, charge decay is largely independent of particle composition and morphology.

EPS particles were transferred to the experimental setup directly from their packaging container (nylon bag). Conversely, aerogel and pumice samples crushed to the

appropriate size and were then stored in a desiccator at <10% RH until beginning an experiment. Amaranth samples were toasted immediately prior to inserting them into TAL. We note that particles inserted into TAL may be precharged as a result of contact electrification during handling. For instance, **Fig. 4.2a** shows that EPS particles taken from their plastic packaging bag generally carry positive charge (consistent with the relative positions of polystyrene and nylon on the triboelectric series [124]). However, the ionization process is capable of erasing this initial bias (**Fig. 4.2b**; **Fig. 4.3b**).

4.2 Schlieren imaging

The Tiny-lev acoustic levitator (TAL) has a well defined theoretical acoustic field that has been explored in detail through simulations [77]. To experimentally confirm our pressure field matched the theory, we imaged the time-averaged acoustic field using a single mirror off-axis schlieren system (**Fig. 4.6**) [27, 95]. In our setup, a point source of light was created by placing an adjustable iris infront of a 632 nm LED light. The iris was adjusted to have a diameter of approximately 1 mm. The light traveled from the iris and passed through the acoustic field, then reflected off the front surface of a spherical mirror. The reflecting, front surface of the mirror was aluminized. The quality of the mirror was crucial; spherical aberrations in our previous attempts produced a broad focus unsuitable for imaging. After reflecting, the light was focused to a point of approximately the same size as the iris, where a razor blade is placed. The blade cuts off approximately half of the light from entering the camera lens. The final image consists of grey areas where the air pressure is $\approx$ 1 atm and black or white areas in areas of high and low pressure. The grey scale is associated with a magnification of the index of refraction due to changes in pressure and therefore density and index of refraction.

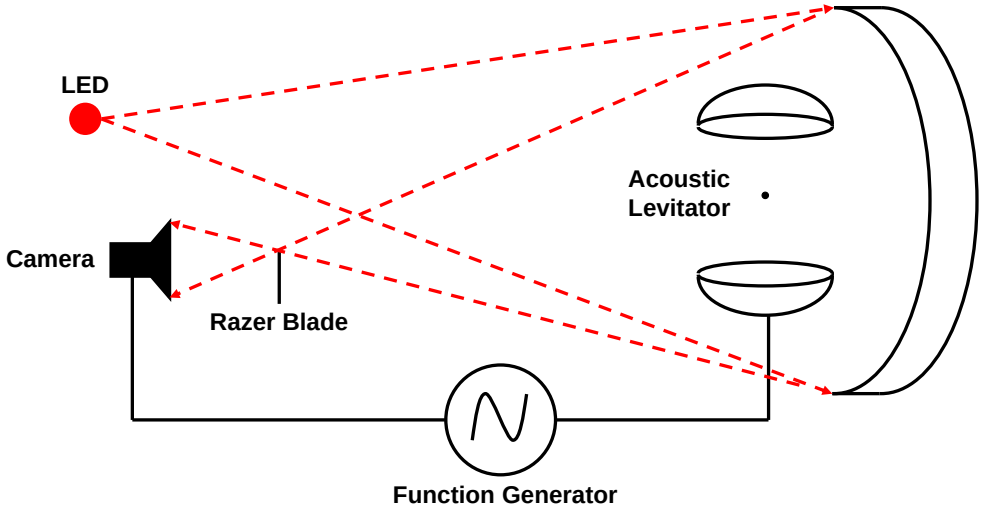

Figure 4.6: The design of the schlieren imaging system. A monochromatic LED emits coherent light from a pinhole source, which hits a concave mirror of diameter 203 mm and focal length 750 mm. The mirror is placed 1.2 m away from the source. The acoustic levitator is placed adjacent to the mirror. The synchronized high-speed camera captures the light that passes above the razor blade. See reference [27] for additional details.

In order to maximize the visual differences between high and low pressure, the 40 kHz square wave that drove the transducers was synced to a high-speed camera (Phantom V7.11, Vision Research). The signal was clock divided to reduce redundant frames, so that movies were taken at 256 fps, and the exposure time was set to half the original period, 12.5 μs. This allowed the camera to capture only positive or negative pressure swings of the standing acoustic wave. To only capture a positive or negative pressure swing, we adjusted the delay between the beginning of a frame, and the beginning of the camera exposure in that frame. A median pixel combination of a sequence of images was applied to minimize ambient ambient air currents that our schlieren set up was sensitive enough to register. The final result is shown in **fig. 4.4**, where approximately 500 frames taken over 3 s were used.

4.3 Behavior determines the discharge behavior

The environmental chamber which encloses TAL allowed us to explore the effect of atmospheric water (at 25°C) on particle charge decay. We varied RH of the chamber using a combination of boiling water and dry building air before charging. The decay dynamics for a subset of EPS particles are rendered in **Fig. 4.7**. In dry environments, the functional form of the charge decay was linear at early times, giving way to nearly exponential behavior at long times (see black and red curves **Fig. 4.7**). For RH $< 30\%$, all particles experienced charge decay over a characteristic half-life, $t_{1/2}$, of 2-8 days. At higher RH, a more expedient decay rate followed a logistic form (green, pink, and purple curves). This timescale decreased to 1 day or less for RH approaching 100%. Yet, even the shortest decay times in our experiments greatly exceed those of seconds to hours reported in several previous works for broad ranges of RH [101, 64]. We note that those efforts did not use isolated charged surfaces (i.e. tested materials were clamped, tethered, or otherwise secured extraneous surfaces). We suspect that shorter decay times there reflect conduction processes in addition to charge exchange between solid and gas. Indeed, Burgo et al. [5] found multi-day decay times for charged, polyethylene slabs in contact with aluminum, but short decay times at higher RH, possibly resulting from the growth of a conducting water layer on the surface.

Using the TAL system, particles only discharge by exchanging charge carriers with the atmosphere. Previous efforts have invoked ion recruitment processes to account for charge gain or loss on particle and aerosols surfaces [38, 43]. The conventional prediction from such models is that particles reach electrostatic equilibrium in minutes to hours, not days. The dramatic departure from theory implied by the long charge decay times observed in our experiments may indicate that the regions near the charged object are depleted of free ions. Such depletion was recently suggested by Heinert *et al.* [43] to explain the multi-day decay of charge on a magnetically levitated

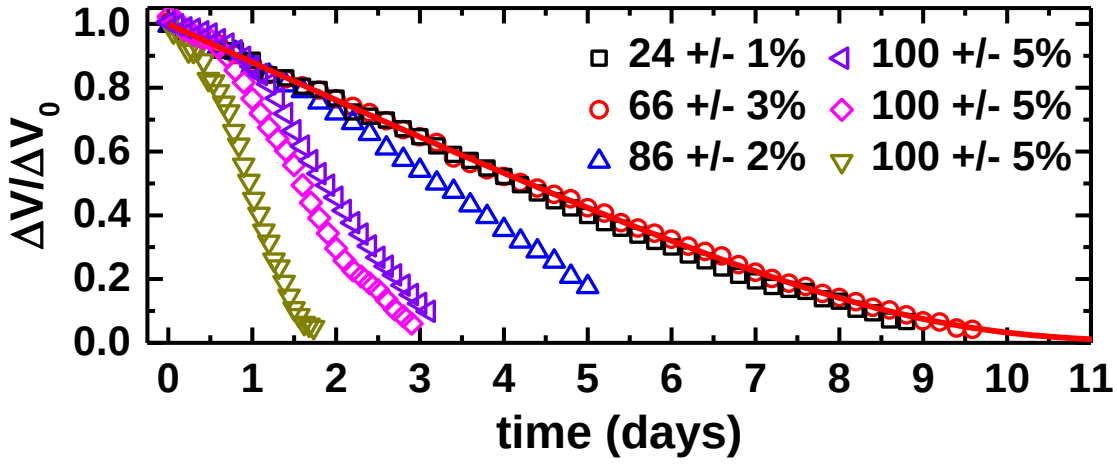

Figure 4.7: Normalized voltage $\Delta V/\Delta V_0$ vs time at various RH values. The low RH data is fit well by Eq. 4.3 as shown by the red line which fits the 66% RH decay. The fit parameters are $Q_0 = 1$, $Q_c = 0.11$, and $K = 1.24$.

conducting disk.

Particles in our experiments have radii of $a \approx 1$ mm and initial charges $|Q_0| \lesssim 1$ pC $= 6.25 \times 10^6$ elementary charges. These conditions correspond to approximately 0.5 charges for every square micron of particle surface area. While this charge density may seem dilute, the background ion density, as measured by the Gerdien tube condenser, is less than 1 ion/mm^3 for both positive and negative ions. The dynamics of charge neutralization in our experiments can be understood by considering the ratio of the potential energy to thermal kinetic energy for a single airborne ion: $e\phi/k_BT = eQ/4\pi\epsilon_0 r k_B T$. In this framework, k_B is Boltzmann's constant, T is the temperature, ϵ_0 is the permittivity of free space, e is the elementary charge, and r is the separation between the ion and the charged particle. We make the simplifying assumption that oppositely-charged ions near the particle are always captured, whereas ions far from the particle can escape capture. The boundary between these regimes is estimated as $|e\phi/k_BT| \approx 1$.

For the typical parameters described above when $|Q_0| = 1$ pC, this boundary corresponds to a radius $r \approx 35$ cm, which is larger than the size of our experimental chamber. Thus, in the early stages of charge decay, we can assume that *every* oppo-

sitely charged ion generated in the chamber is captured by the charged, millimetric particle. Indeed, the near linear decays seen in **Fig. 4.7** for low RH suggest that discharge rates are likely determined by and equal to the rate of ion production in air surrounding the particle. However, as the particle loses surfaces charge, the capture radius becomes significantly smaller than the size of the experimental chamber. For example, when $Q = 0.1Q_0$, $r \approx 3.5$ cm, and the decay rate of charge will depend on Q. Moreover, free ions may be funneled away by the flow system that maintains the chamber at low RH or may be neutralized by ions of opposite polarity before being captured by the particle.

A very simple model for the charge decay that includes both of these regimes can be written as:

$$\frac{dQ}{dt} = -\frac{K}{1 + Q/Q_c}Q, \tag{4.2}$$

where K is a characteristic rate, and Q_c is a characteristic charge representing a crossover between these regimes. A similar equation results from the capture of molecules by diffusion to a spherical particle covered in absorbing patches, as first discussed by Berg and Purcell in the context of chemoreception [9]. This equation can be readily solved for $Q(t)$:

$$Q(t) = Q_c W\left[\frac{Q_0 \exp\left(Q_0/Q_c - Kt\right)}{Q_c}\right], \tag{4.3}$$

where W represents the Lambert function, and Q_0 is the initial charge on the particle. This 3-parameter function shows excellent agreement with the data in dry conditions, as shown by the solid line in **Fig. 4.7**. It is important to note that Eq. 4.3 does not depend on the size of the particle, which may explain similar decay times observed in experiments with much larger, centimeter-scale objects [43, 5].

Even though data for RH as high as 60-70% follows the same trend as for very dry conditions, real lofted particles are often found in water-rich environments near

saturation. As **Fig. 4.7** shows, the decay rate of charge increases significantly with higher RH. Generally, equilibrium ion concentrations increase with RH [19], but the rate at which a system recovers to its equilibrium concentration is not well-known. In our experiments, we assume the charged particle and surfaces of the TAL apparatus quickly deplete nearly all ions in the chamber once the ionizer is shut off. Thus, we expect that higher RH acts to return the ion concentration to equilibrium more rapidly. Initially, the charge decay rate is small before increasing at later times as the ion concentration returns to equilibrium, resulting in a logistic-shaped decay curve, as seen in **Fig. 4.7**. This particular decay, characterized by an *increase* in decay rate during the lifetime of the experiment, has been observed in other studies [43, 5]. It is unclear if this behavior is solely related to RH, or other uncontrolled conditions.

Although data at higher RH cannot be fitted with Eq. 4.3, we can compare the half-life, $t_{1/2}$, of charge decay across all materials and RH. While there is a natural variability in decay time for individual experiments conducted at the same RH (see **Fig. 4.8c**), **Fig. 4.8a** shows no observable variation of $t_{1/2}$ for the different particles used in our experiments. These particles vary in their shape, size, porosity, and hydrophobicity. Additionally, $t_{1/2}$ decreases with RH by roughly a factor of 10 at saturation for all particle types. This is consistent with our model since the capture probability of a given ion is only dependent on the atmospheric conditions and the total charge on the levitating particle. For these relative humidity tests, RH was maintained within 10% variance over the entire experiment, with the majority of data points within 5% RH variance.

It is possible that in ion rich environments the charge decay of these particles would vary based on local surface properties or combinations of ion transport mechanisms such as diffusion, electrostatic drift, and convection. In our experiments, the acoustic levitator generates a small amount of heat, which nonetheless causes convection that is visible in the Schlieren imaging of the acoustic field. However, these environmental

variations occur on much shorter timescales where we observe no large fluctuations in the rate of charge decay.

Atmospheric dust may carry net positive or negative charge [83, 48, 52]. **Figure 4.8b** shows results for negatively and positively charged EPS particles, indicating little difference in $t_{1/2}$. To charge with a different polarity we simply switched the polarity of the high-voltage power supply. If discharge is mostly determined by ion recruitment from the atmosphere, then the decay rate should represent the relative concentrations of positive and negative ions. Measurements suggest a roughly equal number of positive and negative ions in our experimental chamber, explaining the similarity between decay rates for positively- and negatively-charged particles.

Lofted particles in Earth's atmosphere also experience varying amounts of UV radiation, ranging from UVC at the highest altitudes, to UVA near the Earth's surface. To simulate this exposure, in our experiments we used two different types of UV light bulbs. The bulbs were suspended at the inside wall of the chamber, horizontally aligned with the particle. The chamber was left partially open to laboratory air (dry conditions), and the initial ΔV_0 was measured before UV irradiation. Naively, one may expect that UV radiation always accelerates charge decay as high energy photons neutralize surface charge. Previous studies have shown that the efficiency of UV light on discharging can vary dramatically in a narrow range of wavelength [106]. Strikingly, we observe that UV radiation can even *extend* the life of charge on some particles. **Figure 4.9** shows data for EPS particles with negative **(4.9a)** and positive **(4.9b)** initial charge in dry conditions (low RH). With no UV radiation, particles exhibit a multi-day decay timescale ($t_{1/2}$), as expected. For UVA radiation (365 nm, 3.40 eV, irradiance of 7.07×10^{-3} W/m^2), $t_{1/2}$ decreased slightly to 2-3 days for negatively-charged particles, yet $t_{1/2}$ *increased* significantly for positively-charged particles.

This asymmetry can be explained by noting that UV radiation can potentially

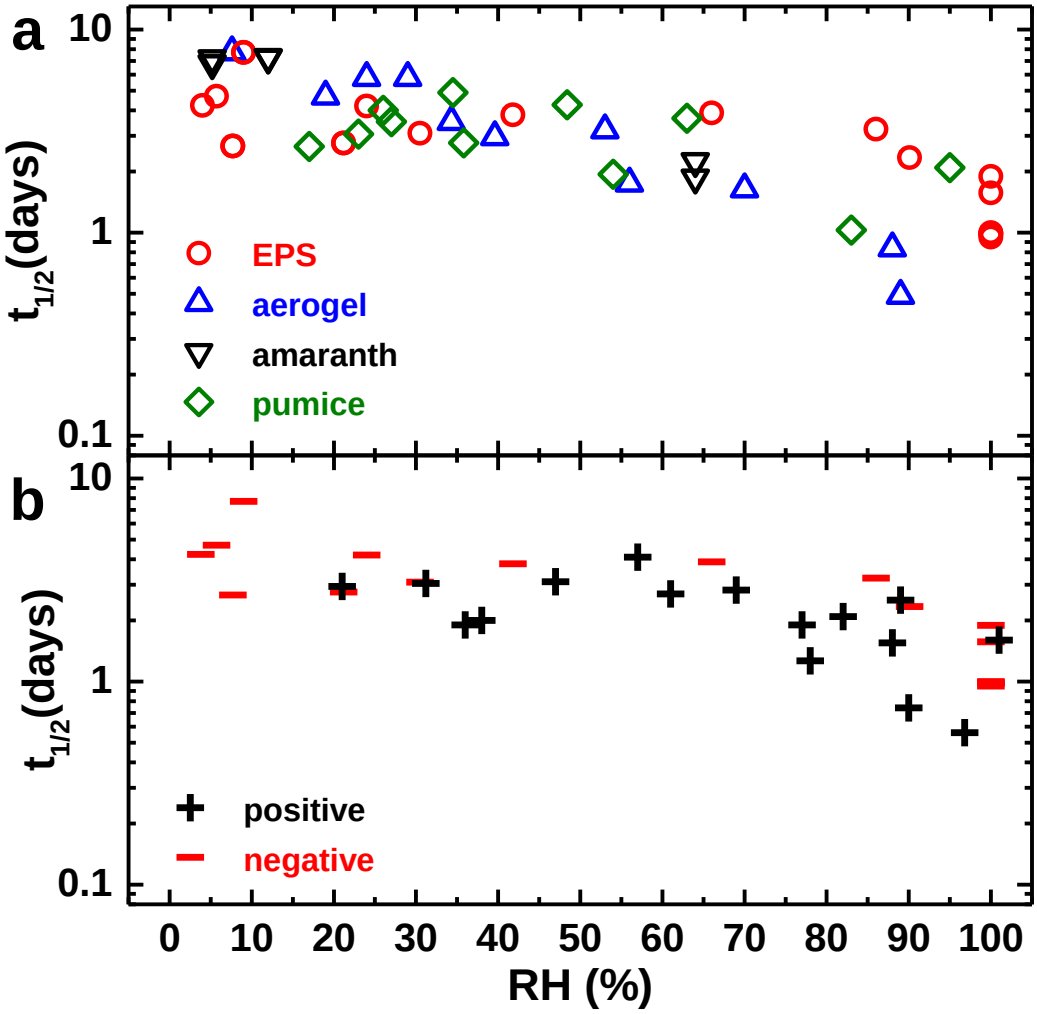

Figure 4.8: $t_{1/2}$ vs RH for (a) different materials that were negatively charged, and (b) EPS that was positively or negatively charged. We observed similar trends for $t_{1/2}$ with increasing RH for all materials used in (a). In (b) we observe a slightly smaller half life at lower RH for EPS particles, possibly due to differences in positive and negative ion concentrations.

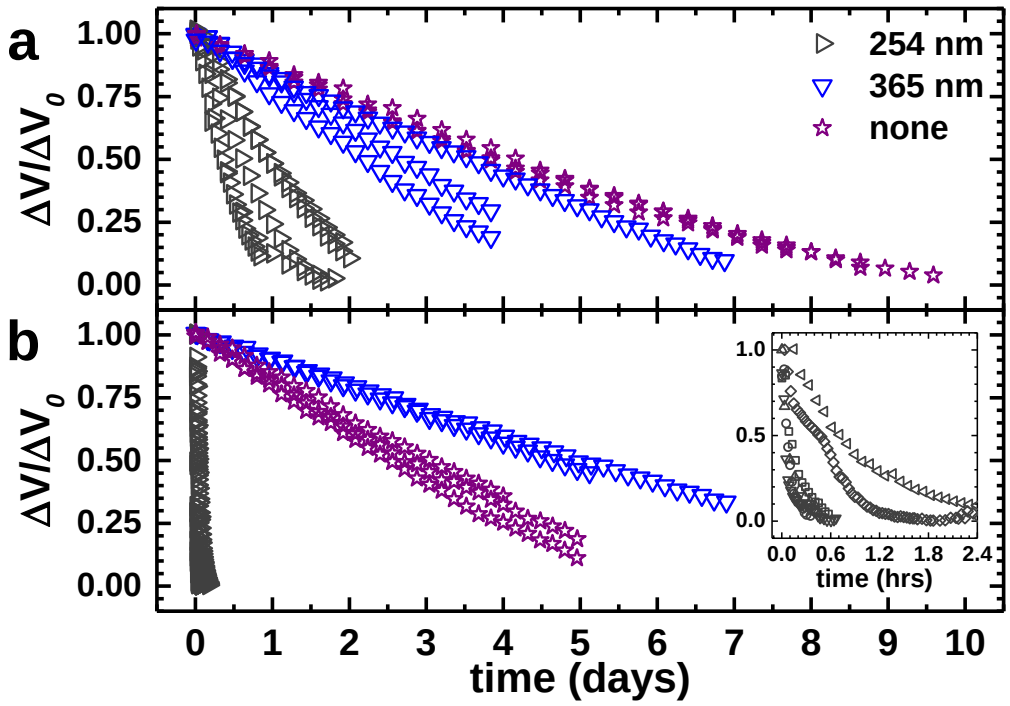

Figure 4.9: $\Delta V/\Delta V_0$ vs. time for particles irradiated by UV of different wavelengths, as indicated in the legend. Panel (a) represents negatively-charged EPS, and panel (b) represents positively-charged EPS. The inset of (b) shows a zoom-in of positively-charged particle data with the shortest decay times. The different symbols in the inset correspond to repeated experiments.

ionize organic atmospheric impurities that could deplete the local ion concentration, or even by direct photoelectric charging of the particle. The charged surface states can be highly variable given the complex particle materials, and the potential presence of water. Our experiments cannot disentangle these effects at the moment, however, the asymmetry is highly relevant for most airborne particles since UVA radiation can penetrate to Earth's surface. For UVC radiation (254 nm, 4.88 eV, irradiance of 1.06×10^{-1} W/m^2), which is absorbed in Earth's upper atmosphere, particles of either charge polarity experienced a decrease in $t_{1/2}$, yet positively charged particles decayed in less than 1 hour. This drastic decrease in the decay rate is almost certainly due to photoelectric electrons emitted from the surface of the copper mesh comprising the Faraday cup. The work function of copper is 4.7 eV.

Further experiments are required to test the limits of our ion capture model. I designed a new vacuum chamber with the purpose of studying the effects of different gaseous environments and pressures, **Fig. 4.10a**. If ion generation is the driving discharge mechanism, then submitting particles to gasses that spontaneously ionize at different rates or not at all will drastically alter $t_{1/2}$. Since ionization of air is due to a collection of mechanisms including: the radioactive decay of Radon, chemical pollution, and dissociation of water molecules, we should expect that particles in pure inert gases will retain charge for far longer. In fact, a preliminary result for charge decay of an EPS bead in the vacuum chamber shows a longer decay time than our previous results, **Fig. 4.10b.**. While this test is still with air, it does show that our previous non-vacuum sealed chamber could let in ambient air at a small, but measurable rate.

Other proposed experiments in the new chamber include testing other particle types. To expand the types of particles we can manipulate we must build a more powerful levitator. Some questions we hope to explore with a more robust levitator include: If only the environment is important, do we get the same charge

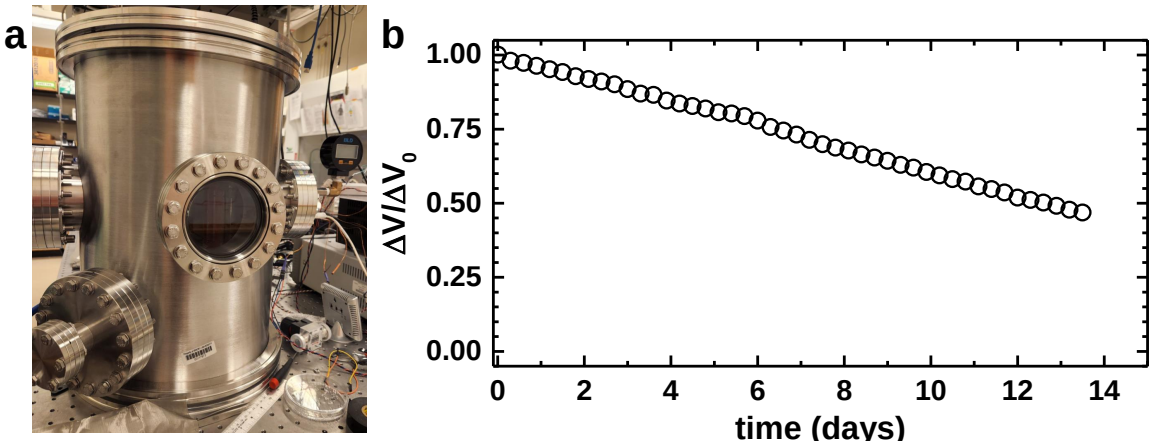

Figure 4.10: a) A new vacuum chamber will allow for more controlled environments to prove our ion capture model. b) preliminary charge decay results show a longer lifetime of charge than our previous chamber. We attribute this to leaks in the old chamber that let in a measurable amount of fresh air (ions).

decay for conductive materials or with glass particles covered in various hydrophobic/hydrophilic coatings? Can we investigate charge on suspended fluid drops? by varying the type of gas used, does the charge decay rate vary with ion concentration and type? and Can we similarly measure how particles charge in different gas environments?

4.4 1-D sedimentation model

How does the multi-day decay of charge affect transport in the atmosphere? The dynamics of a particle with a spherical equivalent diameter (SED) of D settling out of the atmosphere are governed by gravitational, F_g, drag, F_d, and electrostatic forces, F_e. We can thus quantify the impact of charge decay on atmospheric residence time by computing the difference of sedimentation time t_{set} between a charged particle and an otherwise identical neutral particle. Here, we assume the dynamics of a spherical particle with density ρ_p and diameter D falling through an air column in 1D:

$$\frac{1}{6}\pi\rho_p D^3\dot{v} = F_g + F_d + F_e, \tag{4.4}$$

where v is the particle's velocity in the y-direction, and the dot refers to differentiation with respect to time. F_g, F_e, and F_d are the gravitational, electrostatic, and drag forces, respectively:

$$F_g = -\frac{1}{6}\pi D^3\rho_p g, \tag{4.5}$$

$$F_e = \pi D^2\sigma(t)E, \tag{4.6}$$

$$F_d = -\frac{1}{8}C_d\rho_a\pi D^2 v|v|. \tag{4.7}$$

Above, g is the acceleration due to gravity, $\sigma(t)$ is the time-dependent surface charge density on the particle, and E is an ambient electric field. Note that the electrostatic force can either accelerate or retard sedimentation depending on the direction of the field and the polarity of the particle's charge.

Finally, ρ_a is the density of air, which depends on the altitude through the ideal gas law. For simplicity, we assume temperature varies with altitude according to a linear lapse rate $L = 0.0065$ K/m:

$$T = T_0 - Ly. \tag{4.8}$$

Where $T_0 = 300$ K is the temperature at sea level. Additionally, the variation of pressure with altitude p may be expressed as:

$$p = p_0(T/T_0)^{-(gM/(RL))}, \tag{4.9}$$

where $p_0 = 101$ kPa, $M = 0.02896444$ kg/mol is the molar mass of dry air, and $R = 8.31447$ J K^{-1} mol^{-1} is the universal gas constant. From these relationships, the

density of air may be computed as:

$$\rho_a = pM/(RT) \tag{4.10}$$

The drag coefficient C_d in Eq. 4.7 is computed using the formulation presented by Parmar et al. [87]:

$$C_d = \frac{24}{\mathrm{Re}}(1 + 0.15\mathrm{Re}^{0.687}) + 0.42\left(1 + \frac{42500}{\mathrm{Re}^{1.16}}\right)^{-1}. \tag{4.11}$$

Re is the Reynolds number given by $\rho_a|v|D/\mu$, where μ is the dynamic viscosity of air. **Equations 4.4 - 4.11** are solved numerically using the methodology described in Mastin et al. [78].

For this analysis, we consider particles with SEDs in the range of 1 - 100 μm and densities between 1000 - 2900 kg/m^3. Earth's fair weather electric field is on the order of 0.1 kV/m and points toward the surface. However, $\sim$ 10 kV/m is typical in dust storms [122], and $\sim$ 100 kV/m has been measured during foul weather [32]. As such, we employ a conservative electric field range spanning $\pm$5 kV/m. Furthermore, we assume that particles are initially charged to the theoretical maximum limit of $\sigma \sim 10^{-5}$ C/m^2 and then decay exponentially with a half life of 4 days. Lastly, we determined settling times for particles falling from an altitude of 5 km, an elevation at which dust has been detected in the Saharan Air Layer [85]. The model implements a simple atmospheric profile to account for changing pressure as a particle descends, see **Fig. 4.11.** We note that our model excludes the effects of turbulence and convective uplift.

Settling times from an altitude of 5 km can range between a few hours for the largest particles to $>10^2$ days for the smallest grains **(Fig. 4.12a)**. Because small, neutral particles take months or even years to settle, electrostatic effects with half-lives of a few days should not affect t_{set}. Likewise, electrostatic forces play a minimal role

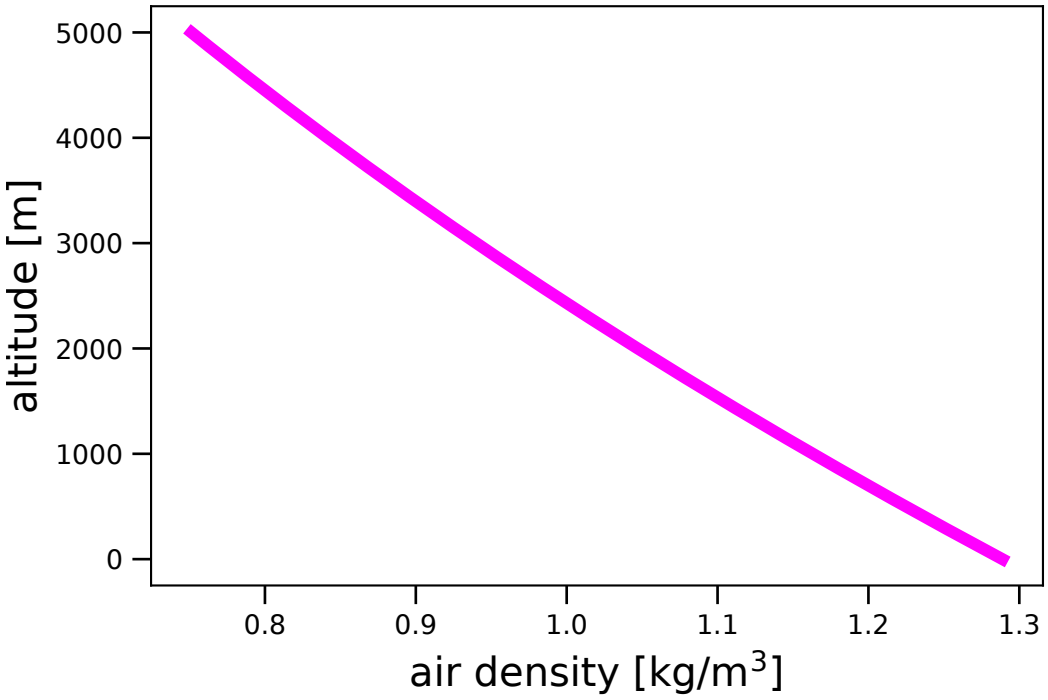

Figure 4.11: Variation of air density with altitude used in this work. The model assumes a lapse rate of L = 0.0065 K/m

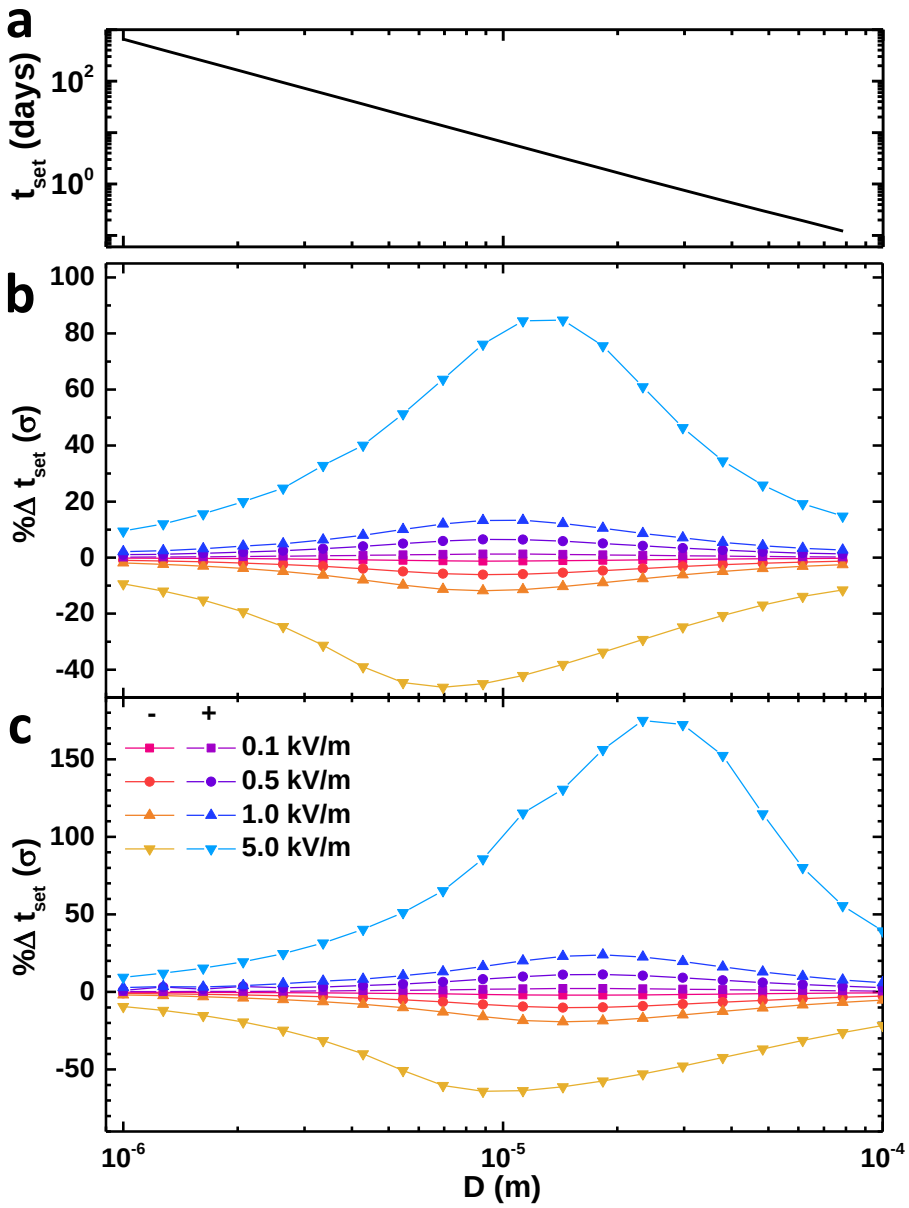

Figure 4.12: Model results for silicate (ρ = 2900 kg/m^3) (a & b) and plastic (ρ = 1000 kg/m^3) (c) particles sedimentation times assuming no turbulent mixing from an altitude of 5 km. (a) Without electrostatic forces, t_{set} is determined by gravitational and drag forces, ranging from years to hours for particle diameters 1-100 μm. (b & c) Percent change in settling time for a positively-charged particles of silicate, b, and plastic, c, in an external electric field with a surface charge density $\sigma = 10^{-5}$ C/m^2 that decays exponentially with $t_{1/2} = 4$ days. The symbols represent different ambient electric fields (+, upward pointing; − downward pointing).

for large particles since these are dwarfed by inertial forces. Conversely, our numerical experiments show that when $t_{set} \approx t_{1/2}$, electrostatic effects can substantially modify particle residence times. Indeed, we find that charge most strongly influences the dynamics of 2900 kg/m^3 particles (mineral dust) with SEDs of 5-20 μm by increasing t_{set} by 80% (**Fig. 4.12b**). For lighter 1000 kg/m^3 particles (e.g. microplastics), the effects of electrostatic forces are shifted toward particles with SEDs of 10-30 μm and can modify the settling times by up to 175% (**Fig. 4.12c**). These results are consistent with both experimental [104] and inferences from field observations [75].

Beyond more complex fluid dynamics, we note that the above model neglects additional electrostatic processes that may retard, reverse, or accelerate charge loss. As aforementioned, charged dust plumes have been detected at large distances from their sources, suggesting that in-situ charging mechanisms keep lofted particles electrified well beyond the timescales measured here [85, 40]. Additionally, we suspect that other environmental factors (such as pressure and temperature) may influence the retention of charge, and these should be explored in future work. However, our first-order analysis highlights the effects electrostatic forces may have on the transport of particles with $D \sim 10$ μm. Whether these forces help retain particles in the atmosphere (or more easily remove them) requires better understanding of the charge distribution in dust layers and electric fields at elevation.

Conclusions

Using acoustic levitation and non-contact charge measurement, we find that isolated particles of any material can retain charge for weeks. By levitating the particle and using a Faraday cup charge is monitored without introducing conduction to ground. This non-contact method means that the particle can only discharge through the gaseous environment it encounters. In general, RH decreased the half-life of charge

($t_{1/2}$), but the effect was less pronounced than reported in previous works [101, 5]. Additionally, $t_{1/2}$ was insensitive to the charge polarity of the particles for a broad range of RH. However, exposure to UV light either accelerated or arrested charge decay, depending on charge polarity and UV wavelength. Both RH and irradiation control the local concentration of ions in the air surrounding a charge particle, and ultimately determine the longevity of charge on a particle's surface. Using our experimental data as input to a simple 1D model, we find that electrostatic forces significantly modulate the residence times of airborne coarse mode dust with diameters 5-30 μm. Although dust particles are not entirely isolated and encounter charging environments, we provide the first measurements of charge decay on mm-scale lofted particles, and demonstrate that electrostatic forces and charge decay must be considered in dust transport models.

Chapter 5

Conclusions

During my time at Emory, I have successfully used electrostatic concepts to develop new measurement techniques in two separate systems. In the first system, I developed a thickness measurement for Leidenfrost vapor layers of known geometries that showed hydrodynamics determine the minimum Leidenfrost temperature. I then successfully simulated vapor layers where we hope to uncover inertia's role in nucleating the failure causing instability. In the second system, I worked with a postdoctoral researcher to develop a non-contact measurement for charge decay of acoustically levitated particles. We found that charge lasted for much longer on isolated particles than previous theories had predicted. We were also able to show how long-lasting charge on particles of a certain size should be implemented in models to predict travel distances of certain particles. These measurements can be scaled and applied to similar systems where non-contact or rapid sampling is required.

In the Leidenfrost experiments I used an inverse Leidenfrost geometry that let us precisely control the surface area of the vapor layer. We varied the thermal properties of the solid and the NaCl concentration of the water. We found a failure temperature, T_-, that was independent of the parameters tested and was more than 100°C lower than the temperature required to form the vapor layer, T_+. The measurement

technique we developed relies on a fixed geometry of the vapor layer "capacitor" and thus could be used to test the effects of other parameters on vapor layer failure. For instance we could add surfactant to the water or change the evaporating fluid altogether to investigate the role of surface tension. We could purposefully roughen a surface, physically or through corrosion, to investigate at what surface grit does roughness begin to matter. Finally, we could make new experimental hot objects of a wider range of thermal properties and sizes to compare to the wider range available in simulation. It was easier to tackle some of these problems using simulations as opposed to machining parts and running more experiments. So I created the COMSOL Multiphysics Leidenfrost simulations discussed in **chapter 3** to compare experiment to simulation, expand upon our previous results, and focus on the instability failure mechanism that determines T_{-}.

In **Chapter 3**, I combined the heat transfer, laminar flow, and phase field interfaces using the two-phase flow and nonisothermal flow multiphysics modules of COMSOL. I introduced evaporation as a heat source term found in the literature to implement all the possible forces related to the failure causing instability. I explored the influence of solid thermal properties and surface area on the failure temperature, T_{-}. T_{-} found in simulations acted as a lower bound for T_{-} found in the experiments discussed in **chapter 2**. We once again determined that the thermal properties of the solid did not affect T_{-}. However, we were able to explore a larger surface area range in simulations where we see a decrease in T_{-} with surface area, even approaching boiling like T_{-} of the smallest known droplets. We then investigated which parameters affect T_{-} in order to determine the cause of the hydrodynamic instability. When isolating and altering the density of the gas, ρ_v, we found an increase in T_{-} with the same interface shape as with real parameters. Since ρ_v most strongly effects the inertial terms of the Navier-Stokes equations, our current hypothesis is that inertia drives failure. At first, some perturbation at the interface causes a wave to form.

Then, as the wave brings fluid close to the hot solid the restoring forces due to evaporation and surface tension are enough to suppress them. However, at the critical temperature, T_{-}, the inertia of an incoming wave peak at the surface overcomes the restoring forces and initiates liquid-solid contact. I am continuing to test other variables, including neglecting the inertial term altogether, in the simulation to see if there are other coupled effects. There may also be other future directions for these simulations including: changing the surface roughness (add a bump), changing the shape of the hot object (pointed, flat, elliptical instead of spherical), and changing the fluid properties. All of these could help test our hypothesis that inertia drives collapse. Numerous systems use lubrication approximations for thin lubricating flows, from disk drives to car engines. Knowing when those assumptions break down has implications for investigating instabilities in those systems.

In my final project, discussed in **chapter 4**, we used an acoustic levitator to isolate insulating particles in order to investigate charge decay. We varied the particle type, polarity of the particles, and subjected them to UV radiation. We found that particles of any material can retain charge for weeks and determined that it is the environment which determines charge decay. Using an ion capture model that compares the thermal and electrical energy of the particles we were able to fit low humidity experimental data quite well. We were then able to show, using a simple 1-D sedimentation model, that charge is important for atmospheric particles with diameters 5-30 μm. To further prove our theory that ion creation near the particle determines the discharge rate I built a new experimental chamber. We hope to levitate denser conducting materials to further show that particle type does not matter. We also want to levitate fluids which may charge or discharge through other mechanisms. Most importantly the new chamber will allow us to finely tune the gas environment from alternate gas compositions to pressures approaching a vacuum. The observations presented in this chapter prove that the current understanding of charge and

discharge is faulty. Further work is required to investigate the leading causes and mechanisms for charge transfer especially in fluid environments. Furthermore, it is likely that long lasting charge can influence a multitude of sedimenting materials from seeds, to pollen, or even small animals like spiders sailing between branches.

Bibliography

[1] K. H. M. Abdalrahman, Sabariman, and E. Specht. Influence of salt mixture on the heat transfer during spray cooling of hot metals. *International Journal of Heat and Mass Transfer*, 78:76–83, 2014.

[2] A.A. Adebiyi and J.F. Kok. Climate models miss most of the coarse dust in the atmosphere. *Sci. Adv*, 6(15):9507, 2020.

[3] M.A.B Andrade, N. Pérez, and J.C. Adamowski. Review of progress in acoustic levitation. *Braz. J. Phys*, 48:190–213, 2018.

[4] Karen Aplin, Isobel Houghton, Keri Nicoll, Michael Humphries, and Alex Tong. Electrical charging of volcanic ash. In *Proc. ESA Annual Meeting on Electrostatics*, page 1, 2014.

[5] T. Augusto de Lima Burgo, A.C Rezende, S. Bertazzo, A. Galembeck, and F. Galembeck. Electric potential decay on polyethylene: Role of atmospheric water on electric charge build-up and dissipation. *J Electrostat*, 69(4):401–409, 2011.

[6] Sobac B., A. Rednikov, S. Dorbolo, and P. Colinet. Leidenfrost effect: Accurate drop shape modeling and refined scaling laws. *Phys. Rev. E*, 90:053011, 2014.

[7] C. Bain. Drip painting on a hot canvas. *Nature Nanotechnology*, 2:344–345, 2007.

[8] K. J. Baumeister, R. C. Hendricks, and T. D. Hamill. Metastable leidenfrost states. *NASA Technical Note D3226*, 1966.

[9] H. C. Berg and E. M. Purcell. Physics of chemoreception. *Biophys. J.*, 20(2): 193–219, 1977.

[10] A-L Biance, C. Clanet, and D. Quéré. Leidenfrost drops. *Phys. Fluids*, 15: 1632–1637, 2003.

[11] M. L. Boas. *Mathematical Methods in the Physical Sciences*. Wiley, 2005.

[12] A. Bouillant, T. Mouterde, P. Bourrianne, C. Clanet, and D. Quéré. Symmetry breaking in leidenfrost flows. *Physical Review Fluids*, 3:100502, 2018.

[13] A. Bouillant, T. Mouterde, P. Bourrianne, A. Lagarde, C. Clanet, and D. Queéré. Leidenfrost wheels. *Nature Physics*, 2018.

[14] W. S. Bradfield. Liquid-solid contact in stable film boiling. *Ind. Eng. Chem. Fundamen.*, 5:200–204, 1966.

[15] H. Bruus. Acoustofluidics 7: The acoustic radiation force on small particles. *Lab Chip*, 12:1014, 2012.

[16] J. C. Burtin, F. M. Huisman, P. Alison, D. Rogerson, and P. Taborek. Experimental and numerical investigation of the equilibrium geometry of liquid lenses. *Langmuir Article*, 26:15316–15324, 2010.

[17] J. C. Burton, A. L. Sharpe, R. C. A. van der Veen, A. Franco, and S. R. Nagel. Geometry of the vapor layer under a leidenfrost drop. *Phys. Rev. Lett.*, 109: 074301, 2012.

[18] J.C. Burton and P. Taborek. Two-dimensional inviscid pinch-off: An example of self-similarity of the second kind. *Physics of Fluids*, 19, 2007.

[19] H.R. Carlon. Equilibrium ion content of water vapor in air. *J. Applied Phys.*, 52(4):2638, 1981.

[20] G. Castanet, O. Caballina, and F. Lemoine. Drop spreading at the impact in the leidenfrost boiling. *Phys. Fluids*, 27:063302, 2015.

[21] T. A. Caswell. Dynamics of the vapor layer below a leidenfrost drop. *Physiscal Review E*, 90:013014, 2014.

[22] A. A. S. Chaibou, X. Ma, and T. Sha. Dust radiative forcing and its impact on surface energy budget over west africa. *Sci. Rep.*, 10(12236), 2020.

[23] I. Chakraborty, M. V. Chubynsky, and J. E. Sprittles. Computational modelling of leidendfrost drops. *Journal of Fluid Mechanics*, 936, 2022. doi: https://doi.org/10.1017/jfm.2022.66.

[24] P-H. Chiu and Y-T. Lin. A conservative phase field method for solving incompressible two-phase flows. *Journal of Computational Physics*, 230:185–204, 2011.

[25] COMSOL Multiphysics®, v. 5.3. COMSOL AB. Stockholm, Sweden, 2020. URL `www.comsol.com`.

[26] T. R. Cousins, R. E. Goldstein, J. W. Jaworski, and A. I. Pesci. A ratchet trap for Leidenfrost drops. *J. Fluid Mech.*, 696:215–227, 2012.

[27] A. Crockett and W. Rueckner. Visualizing sound waves with schlieren optics. *Am. J. Phys.*, 86:870, 2018.

[28] Lorena De León-Barragán, Gerardo Carrasco-Núñez, and Michael H Ort. Stratigraphy and evolution of the holocene aljojuca maar volcano (serdán-oriental basin, eastern trans-mexican volcanic belt), and implications for hazard assessment. *Journal of Volcanology and Geothermal Research*, 392:106789, 2020.

[29] C Denjean, F Cassola, A Mazzino, S Triquet, S Chevaillier, N Grand, T Bourrianne, G Momboisse, K Sellegri, A Schwarzenbock, et al. Size distribution and optical properties of mineral dust aerosols transported in the western mediterranean. *Atmospheric Chemistry and Physics*, 16(2):1081–1104, 2016.

[30] L. Duchemin, J. R. Lister, and U. Lange. Static shapes of levitated viscous drops. *J. Fluid Mech.*, 533:161–170, 2005.

[31] T.F. Dupont, R.E. Goldstein, L.P. Kadanoff, and S.M. Zhou. Finite-time singularity formation in hele-shaw systems. *Physical Review E*, 47(6), 1993.

[32] Joseph R Dwyer and Martin A Uman. The physics of lightning. *Physics Reports*, 534(4):147–241, 2014.

[33] M. Elbahri, D. Paretkar, K. Hirmas, S. Jebril, and R. Adelung. Anti-lotus effect for nanostructuring at the leidenfrost temperature. *Advanced Materials*, 19:1262–1266, 2007.

[34] B. M. Fabuss and A. Korosi. Vapor pressures of binary aqueous solutions of nacl, kcl, na_2so_4, and $mgso_4$ at concentrations of interest in desalination processes. *Desalination*, 1:139–148, 1966.

[35] R. Freud, R. Harari, and E. Sher. Collapsing criteria for vapor film around solid spheres as a fundamental stage leading to vapor explosion. *Nuclear Engineering and Design*, 239:722–727, 2009.

[36] A. Gauthier, C. Diddens, R. Proville, D. Lohse, and D. van der Meer. Self-propulsion of inverse leidenfrost drops on a cryogenic bath. *Proc. Natl. Acad. Sci. USA*, 116:1174–1179, 2019.

[37] L. P. Gor'kov. On the forces acting on a small particle in an acoustical field in an ideal fluid. *Soviet Physics Doklady*, 6:773, 1962.

[38] R. Gunn. Diffusion charging of atmospheric droplets by ions, and the resulting combination coefficients. *J. Atmos. Sci.*, 11(5):339–347, 1954.

[39] Josh Méndez Harper, Dana Harvey, Tianshu Huang, Jack McGrath III, David Meer, and Justin C. Burton. The lifetime of charged dust in the atmosphere, 2022.

[40] R. G. Harrison, K.A. Nicoll, Z. Ulanowski, and T.A. Mather. Self-charging of the eyjafjallajökull volcanic ash plume. *Environ. Res. Lett.*, 5(2):024004, 2010.

[41] R.G. Harrison, K.A. Nicoll, G.J. Marlton, C.L. Ryder, and A.J. Bennett. Saharan dust plume charging observed over the uk. *Environ. Res. Lett.*, 13(5): 054018, 2018.

[42] D. Harvey, J. Méndez Harper, and J. C. Burton. Minimum leidenfrost temperature on smooth surfaces. *Phys. Rev. Lett.*, 127:104501, 2021. doi: 10.1103/PhysRevLett.127.104501.

[43] C. Heinert, R.M. Sankaran, and D.J. Lacks. Decay of electrostatic charge on surfaces due solely to gas phase interactions. *J Electrostat*, 115:103663, 2022.

[44] SH. Hsu, YH. Ho, MX. Ho, JC. Wang, and C. Pan. On the formation of vapor film during quenching in de-ionized water and elimination of film boiling during quenching in natural sea water. *International Journal of Heat and Mass Transfer*, 86:65–71, 2015.

[45] C-K Huang and V. P. Carey. The effects of dissolved salt on the leidenfrost transition. *International Journal of Heat and Mass Transfer*, 50:269–282, 2007.

[46] S. B. Idso and A. J. Brazel. Planetary radiation balance as a function of atmospheric dust: Climatological consequences. *Science*, 198:731–733, 1977.

[47] R. Jafari and T. Okutucu-Özyurt. Phase-field modeling of vapor bubble growth in a microchannel. *The Journal of Computational Multiphase Flows*, 7, 2015. doi: https://doi.org/10.1260/1757-482X.7.3.143.

[48] M.R. James, S. Lane, and J.S. Gilbert. Volcanic plume electrification: Experimental investigation of a fracture-charging mechanism. *J. Geophys. Res. Solid Earth*, 105(B7):16641–16649, 2000.

[49] G. Jones and W. A. Ray. The surface tension of solutions of electrolytes as a function of the concentration. iii. sodium chloride. *J. Am. Chem. Soc*, 63: 3262–3263, 1941.

[50] P. R. Jones, C. Chuang, T. Sun, T. Y. Zhao, K. Fezzaa, J. C. Takase, D. Singh, and N. A. Patankar. High-speed x-ray imaging of the leidenfrost collapse. *Scientific Reports*, 9:1598, 2019.

[51] H. Jouhara and B. P. Axcell. Film boiling heat transfer and vapour film collapse on spheres, cylinders, and plane surfaces. *Nuclear Engineering and Design*, 239: 1885–1900, 2009.

[52] Felix Jungmann, Maximilian Kruss, Jens Teiser, and Gerhard Wurm. Aggregation of sub-mm particles in strong electric fields under microgravity conditions. *Icarus*, 373:114766, 2022.

[53] Z.A. Kanji, L.A. Ladino, H. Wex, Y. Boose, M. Burkert-Kohn, D.J. Cziczo, and M. Krämer. Overview of ice nucleating particles. *Meteorol. Monogr.*, 58 (1):1.1–1.33, 2017.

[54] S. Kaspari, M. Skiles, I. Delaney, D. Dixon, and T.H. Painter. Accelerated glacier melt on snow dome, mount olympus, washington, usa, due to deposition of black carbon and mineral dust from wildfire. *J. Geophys. Res. Atmos*, 120 (7):2793–2807, 2015.

[55] J. Kestin, H. E. Khalifa, and Correia R. J. Tables of the dynamic and kinematic viscosity of aqueous nacl solutions in the temperature range 20-150°c and the pressure range 0.1-35 mpa. *Journal of Physical and Chemical Reference Data*, 10:71, 1981.

[56] M. Khademi and D. P. J. Barz. Structure of the electrical double layer revisited: Electrode capacitance in aqueous solutions. *Langmuir*, 36:4250–4260, 2020.

[57] H. Kim, J. Buongiorno, LW. Hu, and T. Mckrell. Nanoparticle deposition effects on the minimum heat flux point and quench front speed during quenching in water-based alumina nanofluids. *International Journal of Heat and Mass Transfer*, 53:1542–1553, 2010.

[58] H. Kim, B. Truong, J. Buongiorno, and L-W. Hu. On the effect of surface roughness height, wettability, and nanoporosity on leidenfrost phenomena. *Appl. Phys. Lett.*, 98:083121, 2011.

[59] S. H. Kim, H. S. Ahn, J. Kim, M. Kaviany, and M. H. Kim. Dynamics of water droplet on a heated nanotubes surface. *Appl. Phys. Lett.*, 102:233901, 2013.

[60] S Kinne *et al.* An aerocom initial assessment - optical properties in aerosol component modules of global models. *Atmos. Chem. Phys*, 6(7):1815 – 1834, 2006.

[61] J. F. Kok and N. O. Renno. Electrostatics in wind-blown sand. *Phys. Rev. Lett.*, 100(014501), 2008.

[62] J.P Kok, D.A. Ridley, Q. Zhou, R.L. Miller, C. Zhao, C.L. Heald, D.S. Ward, S. Albani, and K. Haustein. Smaller desert dust cooling effect estimated from analysis of dust size and abundance. *Nat. Geosci.*, 10:274 – 278, 2017.

[63] C. Kruse, T. Anderson, C. Wilson, C. Zuhlke, D. Alexander, G. Gogos, and S. Ndao. Extraordinary shifts of the leidenfrost temperature from multiscale micro/nanostructured surfaces. *Langmuir*, 29:9798–9806, 2013.

[64] S. Kumara, Y.V. Serdyuk, and S.M. Gubanski. Surface charge decay on polymeric materials under different neutralization modes in air. *IEEE Trans. Dielectr. Electr. Insul.*, 18(5):1779–1788, 2011.

[65] G. Lagubeau, M. Le Merrer, C. Clanet, and D. Quéré. Leidenfrost on a ratchet. *Nature Phys.*, 7:395–398, 2011.

[66] B. Lautrup. *Physics of Continuous Matter: Exotic and Everyday Phenomena in the Macroscopic World*. Taylor & Francis, 2004. ISBN 9780750307529. URL `https://books.google.com/books?id=s1265-uY-BgC`.

[67] V. Lee, N. M. James, S. R. Waitukaitis, and H. M. Jaeger. Collisional charging of individual submillimeter particles: Using ultrasonic levitation to initiate and track charge transfer. *Physical Review Materials*, 2, 2018.

[68] J. G. Leidenfrost. *De aquae communis nonnullis qualitatibus tractatus*. Ovenius, 1756.

[69] H. Linke, B. J. Alemán, L. D. Melling, M. J. Taormina, M. J. Francis, C. C. Dow-Hygelund, V. Narayanan, R. P. Taylor, and A. Stout. Self-propelled Leidenfrost droplets. *Phys. Rev. Lett.*, 96:154502, 2006.

[70] J. R. Lister, A. B. Thompson, A. Perriot, and L. Duchemin. Shape and stability of axisymmetric levitated viscous drops. *J. Fluid Mech.*, 617:167–185, 2008.

[71] G. Liu and V. S. J. Craig. Macroscopically flat and smooth superhydrophobic surfaces: Heating induced wetting transitions up to the leidenfrost temperature. *Faraday Discussions*, 146:141–151, 2010.

[72] Volker Lorenz. Maar-diatreme volcanoes, their formation, and their setting in hard-rock or soft-rock environments. *Geolines*, 15:72–83, 2003.

[73] X. Ma and J. C. Burton. Self-organized oscillations of leidenfrost drops. *Journal of Fluid Mechanics*, 846:263–291, 2018.

[74] X. Ma, JJ. Liétor-Santos, and J. C. Burton. Star-shaped oscillations of leidenfrost drops. *Physical Review Fluids*, 2:031602(R), 2017.

[75] H Maring, DL Savoie, MA Izaguirre, L Custals, and JS Reid. Mineral dust aerosol size distribution change during atmospheric transport. *Journal of Geophysical Research: Atmospheres*, 108(D19), 2003.

[76] A. Marzo, S.A. Seah, B.W. Drinkwater, D.R. Sahoo, B. Long, and S. Subramanian. Holographic acoustic elements for manipulation of levitated objects. *nature communications*, 6, 2015.

[77] A. Marzo, A. Barnes, and B.W. Drinkwater. Tinylev: A multi-emitter single-axis acoustic levitator. *Rev. Sci. Instrum.*, 88(8), 2017. doi: 10.1063/1.4989995.

[78] L. G. Mastin. A simple calculator of ballistic trajectories for blocks ejected during volcanic eruptions. *U.S. Geological Survey Open-File Report 01-45*, 2001. URL `https://pubs.usgs.gov/of/2001/0045/`.

[79] LE Mc Keown, MC Bourke, and JN McElwaine. Experiments on sublimating carbon dioxide ice and implications for contemporary surface processes on mars. *Scientific reports*, 7(1):1–15, 2017.

[80] G.D. McDonald *et al.* Aeolian sediment transport on io from lava-frost interactions. *Nat. Commun.*, 13(2076), 2022.

[81] A. McElliot, A. Guerra, M.J. Wood, A.D. Rey, A.M. Kietzig, and P. Servio. Tinylev acoustically levitated water: Direct observation of collective, inter-

droplet effects through morphological and thermal analysis of multiple drops. *Journal of Colloid and Interface Science*, 619:84 – 95, 2022.

[82] J. Méndez Harper, C. Helling, and J. Dufek. Triboelectrification of kcl and zns particles in approximated exoplanet environments. *Astrophys. J*, 867(2):123, 2018.

[83] J. Méndez-Harper, C. Cimarelli, V. Cigala, U. Kueppers, and J. Dufek. Charge injection into the atmosphere by explosive volcanic eruptions through triboelectrification and fragmentation charging. *Earth Planet. Sci. Lett.*, 574(14): 117162, 2021.

[84] J.S. Méndez Harper *et al.* Electrification of sand on titan and its influence on sediment transport. *Nat. Geosci*, 10(4):260–265, 2017.

[85] K.A. Nicoll, R.G. Harrison, and Z. Ulanowski. Observations of saharan dust layer electrification. *Environ. Res. Lett.*, 6(1):014001, 2010.

[86] S. Okuzumi. Electric charging of dust aggregates and its effect on dust coagulation in protoplanetary disks. *Astrophys. J*, 698(2):1122, 2009.

[87] M. Parmar, A. Haselbacher, and S. Balachandar. Improved drag correlation for spheres and application to shock-tube experiments. *AIAA Journal*, 48(6): 1273–1276, 2010.

[88] V.K. Patel, A. Momen, K. Nawaz, A. Abu-Heiba, N. O'Connor, and J.S. Yagoobi. Bto 3.1.2.55 milestone report - preliminary framework for heat exchanger flow distribution model, 2019.

[89] J. D. Paulsen, J. C. Burton, and S. R. Nagel. Viscous to inertial crossover in liquid drop coalescence. *PRL*, 106:114501, 2011.

[90] D. Quéré. Leidenfrost dynamics. *Annu. Rev. Fluid Mech.*, 45:197–215, 2013.

[91] Dojo Research and Consulting. 2d pot boiling tutorial in comsol multiphysics, 2018. URL https://www.youtube.com/watch?v=Awwza_v27EA.

[92] Guillaume Riboux and José Manuel Gordillo. Maximum drop radius and critical weber number for splashing in the dynamical leidenfrost regime. *J. Fluid Mech.*, 803:516–527, 2016. doi: 10.1017/jfm.2016.496.

[93] S. Rodriguez *et al.* Observational evidence for active dust storms on titan at equinox. *Nat. Geosci*, 11(10):727–732, 2018.

[94] C.L. Ryder *et al.* Coarse and giant particles are ubiquitous in saharan dust export regions and are radiatively significant over the sahara. *Atmos. Chem. Phys*, 19:15353–15376, 2019.

[95] Author Settles, GS and Reviewer Covert, EE. Schlieren and Shadowgraph Techniques: Visualizing Phenomena in Transport Media. *Applied Mechanics Reviews*, 55(4):B76–B77, 07 2002. ISSN 0003-6900. doi: 10.1115/1.1483362. URL https://doi.org/10.1115/1.1483362.

[96] I. Sher, R. Harari, R. Reshef, and E. Sher. Film boiling collapse in solid spheres immersed in a sub-cooled liquid. *Applied Thermal Engineering*, 36:219–226, 2012.

[97] Claus Siebe, Sergio Salinas, Lilia Arana-Salinas, José Luis Macías, James Gardner, and Rosanna Bonasia. The˜ 23,500 y 14c bp white pumice plinian eruption and associated debris avalanche and tochimilco lava flow of popocatépetl volcano, méxico. *Journal of Volcanology and Geothermal Research*, 333:66–95, 2017.

[98] J. H. Snoeijer, P. Brunet, and J. Eggers. Maximum size of drops levitated by an air cushion. *Phys. Rev. E*, 79:053011, 036307.

[99] B. Sobac, A. Rednikov, S. Dorbolo, and P. Colinet. Self-propelled leidenfrost drops on a thermal gradient: A theoretical study. *Physics of Fluids*, 29:082101, 2017.

[100] Y. Sun and C. Beckermanm. Sharp interface tracking using the phase-field equation. *Journal of Computational Physics*, 220:626–653, 2007.

[101] Y. Tada and Y. Murata. Direct charge leakage through humid air. *Jpn. J. Appl. Phys*, 34:1926–1927, 1995.

[102] I. Tegen and A.A. Lacis. Modeling of particle size distribution and its influence on the radiative properties of mineral dust aerosol. *J. Geophys. Res. Atmos*, 101(D14):19237–19244, 1996.

[103] P. Thomas and P.J. Gierasch. Dust devils on mars. *Science*, 230(4722):175–177, 1985.

[104] J.R. Toth III *et al.* Electrostatic forces alter particle size distributions in atmospheric dust. *Atmos. Chem. Phys*, 20(5):3181–3190, 2020.

[105] T. Tran, H. J. J. Staat, A. Prosperetti, C. Sun, and D. Lohse. Drop impact on superheated surfaces. *Phys. Rev. Lett.*, 108:036101, 2012.

[106] D. Ugolini, M. Girard, G. M. Harry, and V. P. Mitrofanov. Discharging fused silica test masses with ultraviolet light. *Phys. Lett. A*, 372(36):5741–5744, 2008.

[107] C.R. Usher, A.E. Michel, and V.H. Grassian. Reactions on mineral dust. *Chem. Rev.*, 103(12):4883–4940, 2003.

[108] I. U. Vakarelski, J. O. Marston, D. Y. C. Chan, and S. T. Thoroddsen. Drag reduction by leidenfrost vapor layers. *PRL*, 106:214501, 2011.

[109] I.U. Vakarelski, N. A. Patankar, J. O. Marston, D. Y. C. Chan, and S. T. Thoroddsen. Stabilization of liedenfrost vapour layer by textured superhydrophobic surfaces. *Nature*, 489:274–277, 2012.

[110] M. A. J. van Limbeek, M. H. Klein Schaarsberg, B. Sobac, A. Rednikov, C. Sun, P. Colinet, and D. Lohse. Leidenfrost drops cooling surfaces: theory and interferometric measurement. *J. Fluid Mech.*, 827:614–639, 2017.

[111] S. R. Waitukaitis, V. Lee, J.M. Pierson, S.L. Forman, and H.M. Jaeger. Size-dependent same-material tribocharging in insulating grains. *Phys. Rev. Lett.*, 112, 2014.

[112] B. Weinzierl *et al.* The saharan aerosol long-range transport and aerosol–cloud-interaction experiment: Overview and selected highlights. *Bull. Amer. Meteor. Soc.*, 98(7):1427–1451, 2017.

[113] Gary G Wells, Rodrigo Ledesma-Aguilar, Glen McHale, and Khellil Sefiane. A sublimation heat engine. *Nature communications*, 6(1):1–7, 2015.

[114] W.J. Xie and B. Wei. Parametric study of single-axis acoustic levitation. *Appl.Phys.Lett*, 79:881–883, 2001.

[115] W.J. Xie, C.D. Cao, Y.J. Lü, and B. Wei. Levitation of iridium and liquid mercury by ultrasound. *Phys. Rev. Lett.*, 89:104304, 2002.

[116] V. V. Yagov, A. R. Zabirov, and M. A. Lexin. Unsteady heat transfer during subcooled film boiling. *Heat and Mass Transfer and Properties of Working Fluids and Materials*, 62:833–842, 2015.

[117] V. V. Yagov, M. A. Lexin, A. R. Zabirov, and O. N. Kaban'kov. Film boiling of subcooled liquids. part i: Leidenfrost phenomenon and experimental results

for subcooled water. *International Journal of Heat and Mass Transfer*, 100: 908–917, 2016.

[118] Shi-Chune Yao and Kang Yuan Cai. The dynamics and leidenfrost temperature of drops impacting on a hot surface at small angles. *Exp. Therm. and Fluid Sci.*, 1(4):363–371, 1988.

[119] C.L. Young, I.N. Sokolik, M.G. Flanner, and J. Dufek. Surface radiative impacts of ash deposits from the 2009 eruption of redoubt volcano. *J. Geophys. Res. Atmos*, 119(11):11387–11397, 2014.

[120] H. Yu *et al.* The fertilizing role of african dust in the amazon rainforest: A first multiyear assessment based on data from cloud-aerosol lidar and infrared pathfinder satellite observations. *Geophys. Res. Lett*, 42(6):1984–1991, 2015.

[121] D. V. Zaitsev, D. P. Kirichenko, V. S. Ajaev, and O. A. Kabov. Levitation and self-organization of liquid microdroplets over dry heated substrates. *Phys. Rev. Lett.*, 119:094503, 2017.

[122] H. Zhang and Y. Zhou. Reconstructing the electrical structure of dust storms from locally observed electric field data. *Nat. Commun.*, 11(5072):1–12, 2020.

[123] T. Y. Zhao and N. A. Patankar. The thermo-wetting instability driving leidenfrost film collapse. *PNAS*, 117:13321–13328, 2020.

[124] H. Zou and et al. Quantifying the triboelectric series. *Nat. Commun.*, 10(1427): 1–9, 2019.